DESIGN STRATEGIES FOR POLYMER SOLAR CELLS OF HIGH EFFICIENCY AND LOW COST: MATERIALS, INTERFACE, AND DEVICE STRUCTURES

Liqiang Yang

A dissertation submitted to the faculty of the University of North Carolina at Chapel Hill in partial fulfillment of the requirements for the degree of Doctor of Philosophy in the Curriculum in Applied Sciences and Engineering.

Chapel Hill
2012

Approved by:

James Cahoon

John Papanikolas

Edward Samulski

Sergei Sheiko

Wei You

ABSTRACT

LIQIANG YANG: Design Strategies for Polymer Solar Cells of High Efficiency and
Low Cost: Materials, Interface, and Device Structures
(Under the direction of Wei You)

Polymer-based solar cells are very promising candidates towards cheap solar energy, since they can be solution processed and light weight. The best polymer solar cells currently achieve an efficiency of about 8%, which is not competitive with their thin film inorganic counterparts yet. On the other hand, reducing the manufacturing cost and improving the stability of polymer solar cells are also curial for future commercialization of polymer solar cells. These further developments can be facilitated on more detailed design strategies that can only be established through the elucidation of the fundamentals on conjugate polymers, interface, and device structures.

In this thesis, quantitatively investigations of side chains and substituents to construct ideal conjugated polymers for organic solar cells have been presented. The side chain of a conjugated polymer significantly impacts the photovoltaic properties of the corresponding bulk heterojunction (BHJ) solar cell. In addition to side chains, substituents can further tune energy levels, band gaps, and even morphology. A proper combination of side chains and fluorine substituents on the conjugated backbone is a viable approach to high efficient BHJ devices. Moreover, the poly(3-methylthiophene) (P3MT) interfacial layer successfully serves as the hole transport layer for solution-

processed BHJ polymer solar cells with efficiency as high as 5%, which largely extends the lifetime of polymer solar cells. In addition, solution-processed flexible polymer BHJ solar cells based on silver nanowires (Ag NWs) have been successfully fabricated with recoverable efficiency of 2.5%, which indicates that Ag NW electrodes can serve as a low cost, flexible alternative to indium tin oxide (ITO), and thereby improve the economic viability of polymer solar cells. Finally, a conceptually new approach, parallel bulk heterojunction (PBHJ) has been demonstrated in this thesis. The PBHJ solar cell maintains the low cost manufacturing of single junction BHJ cells, while inherits the major benefit of incorporating multiple polymers in tandem cells. Very respectable power conversion efficiency (PCE) over 7% has been obtained in the PBHJ device, which is among the best performances for polymer solar cells.

To my parents,
To my wife Qian Wang, for love and support

ACKNOWLEDGEMENTS

TABLE OF CONTENTS

LIST OF TABLES

LIST OF FIGURES

xv

LIST OF SYMBOLS AND ABBREVIATIONS

AFM	atomic force microscope (microscopy)
Ag NWs	silver nanowires
BHJ	bulk heterojunction
BnDT	benzo[1,2-*b*:4,5-*b'*]dithiophene
C10,6	2-hexyldecyl
C12	dodecyl
C6,2	2-ethylhexyl
C8	octyl
C8,4	2-butylcotyl
CB	chlorobenzene
CV	cyclic voltammetry
DCB	dichlorobenzene
DTBT	4,7-di(thiophen-2-yl)benzothiadiazole
DTffBT	fluorinated 4,7-di(thiophen-2-yl)benzothiadiazole
E_g	difference between HOMO and LUMO of organic semiconductor
EQE	external quantum efficiency
F	fluorine
FF	fill factor
FTAZ	fluorinated 2-alkyl-benzo[*d*][1,2,3]triazoles
FWHM	full width at half maximum
G	exciton generation rate
GI-WAXS	grazing-incidence wide-angle X-ray scattering

η	power conversion efficiency
HOMO	highest occupied molecular orbital
HTL	hole transport layer
IP	in-plane
IQE	internal quantum efficiency
ITO	indium tin oxide
J_{ph}	photocurrent density
J_s	reverse saturation current density
J_{sat}	saturated photocurrent density
J_{sc}	Short circuit current density
k	Boltzmann constant
LUMO	lowest unoccupied molecular orbital
Mn	number average molecular weight
Mw	molecular weight
MWNT	multiwall-carbon nanotubes
n	diode ideality factor
NDT	naphtho[2,1-b:3,4-b']dithiophene
OOP	out-of-plane
OPV	organic photovoltaic
P	charge separation probability
P3HT	poly(3-hexylthiophene)
P3MT	poly(3-methylthiophene)
PBHJ	parallel bulk heterojunction

$PC_{71}BM$	phenyl-C71-butyric acid methyl ester
$PC_{61}BM$	phenyl-C61-butyric acid methyl ester
PCE	power conversion efficiency
PDI	polydispersity index
PEDOT:PSS	poly(3,4-ethylenedioxythiophene):poly(styrenesulfonate)
PET	polyethylene terephthalate
PV	photovoltaic
q	elementary charge
R_{sh}	shunt resistance
R_s	series resistance
SAM	self-assembled monolayer
SCLC	space charge limited current
SEM	scanning electron microscope (microscopy)
SWNT	single-wall carbon nanotube
TAZ	2-alkyl-benzo[d][1,2,3]triazoles
TCB	trichlorobenzene
TEM	transmission electron microscope (microscopy)
UPS	ultraviolet photoelectron spectroscopy
UV-Vis	ultraviolet–visible spectroscopy
V	Volt
V_0	compensation voltage
V_{app}	applied voltage
V_{oc}	open circuit voltage

XRD	X-ray diffraction
$\mathit{\Delta}E_{DA}$	difference between HOMO of donor and LUMO of acceptor
φ_{m}	work function

CHAPTER 1

INTRODUCTION

1.1. Why Polymer Solar Cells

With the world energy demand increasing, the search for alternative energy sources is a growing academic and industrial pursuit. The limited reserve of carbon-based fuels and increased emissions of greenhouse gases (e.g. CO_2) has placed a greater demand on the renewable and clean energy, such as hydropower, geothermal, wind, and solar. Compared with other renewable energy sources, harvesting energy directly from the Sun via photovoltaic (PV) technologies is increasingly being recognized as one of the most promising long-term solutions – or maybe the ultimate solution – to a sustainable future. Since the 1950s, the power conversion efficiency (PCE) of these devices has steadily improved. Currently, crystalline silicon crystalline silicon based cells and multi-junction solar cells can achieve up to 25%[1] and 35% PCE[2], respectively. Furthermore, in a multi-junction device, where two or more sub-cells are stacked to absorb different regions of the solar spectrum, PCE over 40% have been achieved.[3] However, the high cost of single crystal growth and the complicated manufacturing process compared to fossil fuels limit their wide applications. In order to lower the cost, other types of solar cells such as such as amorphous silicon, cadmium telluride, dye sensitized solar cells, and organic solar cells have been developed. Among them, polymer solar cells are considered promising low-cost alternatives to existing silicon photovoltaics, because of the low weight, the

tenable electronic and optical properties of conjugated polymers and the potential for low-cost roll-to-roll manufacturing.[4]

1.2. Bulk Heterojunction Polymer Solar Cells

In 1959,the first organic solar cell was made by Kallman et al. based on a single crystal of anthracene[5] with a power efficiency of 0.02%. The low efficiency is partly due to organic materials with high dielectric constant, which lead to strongly bound electron-hole pairs, and therefore poor charge separation. In 1986 Tang reported an efficiency of 0.95% and FF of 65% by using thin-film double-layer photovoltaic cells of copper phtalocyanine (CPc) and a perylene tetracarboxylic (PT) derivative[6]. It was found that excitons can easily be dissociated into electrons and holes at the interface of CPc and the PT layer due to their differences in energy levels. The success of this electron donor/acceptor concept largely stimulated research in the field of organic photovoltaics. The seminal discovery of rapid photoinduced electron transfer from a conjugated polymer to the buckminsterfullerene molecule in 1992,[7] led to the first demonstration of an efficient polymer solar cell based on poly[2-methoxy-5-(2'-ethylhexyloxy)-1,4-phenylenevinylene] (MEH-PPV) and a soluble version of the fullerene, [6,6]-phenyl-C61-butyric acid methyl ester (PC$_{61}$BM) in 1995.[8] Since then, the new concept, coined as "Donor-Acceptor Bulk Heterojunction (BHJ)" solar cell, has remained as one of the most active research fields in the past two decades. [9]

1.2.1 Device Configuration and Mechanism

A typical polymer solar cell has a "sandwich" structure (Fig. 1.1) and it is fabricated layer-by-layer, whose four layers, from bottom to top, are the anode, the poly(3,4-

ethylenedioxythiophene) poly(styrenesulfonate) (PEDOT:PSS) layer, the active layer, and the cathode. The anode is usually a plastic or glass substrate coated with a transparent Indium Tin Oxide (ITO) layer. The conductive PEDOT:PSS is used to adjust the energy level and provide a smooth surface to improve the electrical contact between the ITO and the active layer.[10] The organic active layer is used for light absorption and charge separation. The cathode is usually made of a low work function metal such as Aluminum or Calcium.
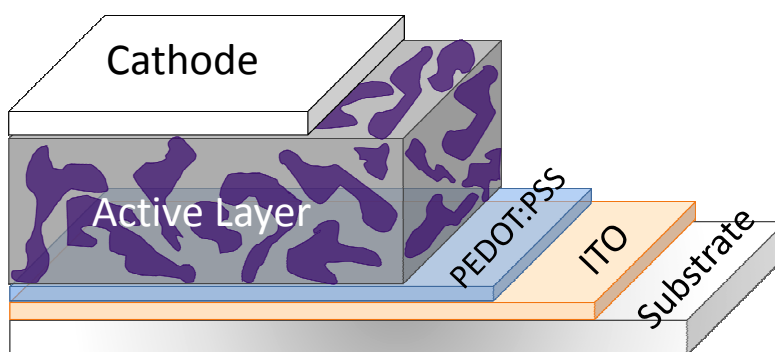
Figure 1.1. A typical structure of "layer-by-layer" polymer solar cell

The fundamental operating principle of a polymer solar cell is based on the cooperative interaction of molecular or polymeric electron donors and acceptors. Typically, photoexcitation of the donor generates excitons (bound electron-hole pairs), as opposed to free charges in the inorganic solar cells, due to the low dielectric constant of organics. These excitons will only find sufficient energetic driving force for dissociation into free charges at the interface with an electron acceptor of suitably high electron affinity. Excitons must therefore diffuse through the donor in order to reach an acceptor site where charges can be generated and then finally be transported through the donor phase (holes) and the acceptor phase (electrons). It is this necessity of having two distinct and interacting species that is the defining characteristic of the organic solar cell. Despite this common attribute, many different types of organic solar cells exist, which can be

grouped in two general categories distinguished by the architecture of the active layer, with either a donor-acceptor bilayer or a bicontinuous donor-acceptor composite, known as a bulk-heterojunction (BHJ). In contrast to the double layer structure, the success of the bulk hetreojunction solar cell can be attributed to the interpenetrated network between the donor and acceptor (Fig. 1.2). The interpenetrated network of BHJ offers two advantages: (a) it minimizes the travelling distance of excitons (electron-hole pair generated upon light absorption) to the donor/acceptor (D/A) interface, and concurrently maximizes the D/A interfacial area, thereby ensuring the exciton dissociation at the D/A interface to generate maximum free charge carriers; and (b) it offers charge transport pathways to facilitate the charge collection at electrodes, completing the conversion of the photon energy to electrical energy (i.e., photovoltaic effect).
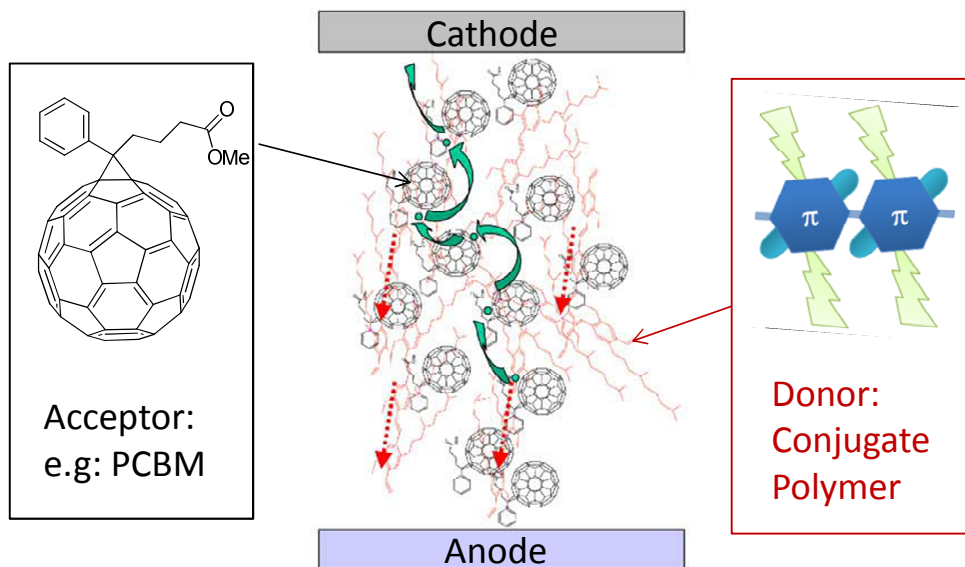
Figure 1.2. Schematic illustration of the active layer in BHJ polymer solar cell

1.2.2 Important Parameters of Organic Solar Cells

The single most important performance parameter of a solar cell is the power conversion efficiency (PCE or η), which can be defined as the ratio of maximum power

out (the blue area shown in Fig. 1.3) to power in. When illuminated with light and placed under short circuit (i.e. applied voltage $= 0$ V), photocurrent is produced in the external circuit. This point is labeled as the short-circuit current (J_{sc}) on the standard current density vs. voltage (J-V) measurement (Fig. 1.3). On the other hand, under open circuit (i.e. $J = 0$ A/m^2), the value of applied voltage is named as the open circuit voltage (V_{oc}). The fill factor (FF) is defined as the ratio of maximum power divided by Jsc $\times$ Voc. Therefore, the PCE is proportional to the product of Jsc, V_{oc}, and FF as shown in the equation: $PCE = \dfrac{V_{oc} \times J_{sc} \times FF}{P_{in}}$.
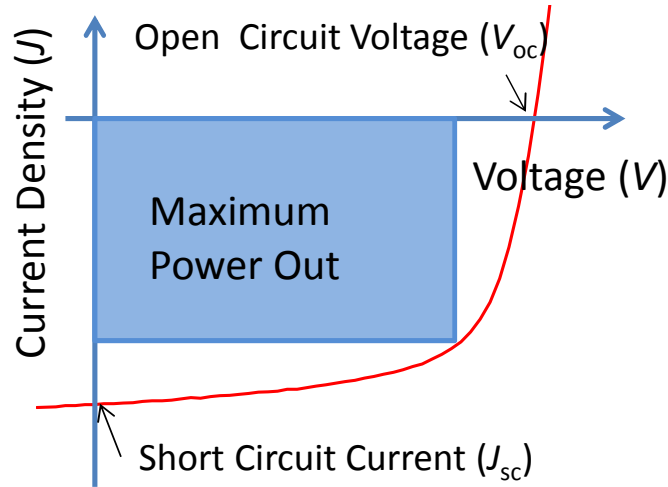
Figure 1.3. A preventative current density-voltage (J-V) curve and key parameters of device measurement.

1.3. Conjugated Polymers for Polymer Solar Cells

The development of new materials has always been the driving force to reach higher efficiency values, with significant contribution from the careful control of the morphology of the Donor-Acceptor blend. A typical conjugated polymer used as the electron donor in polymer solar cells is illustrated in Fig. 1.4. Generally, a conjugated

polymer can be arbitrarily divided into three constituting components: the conjugated backbone, the side chains and the substituents.
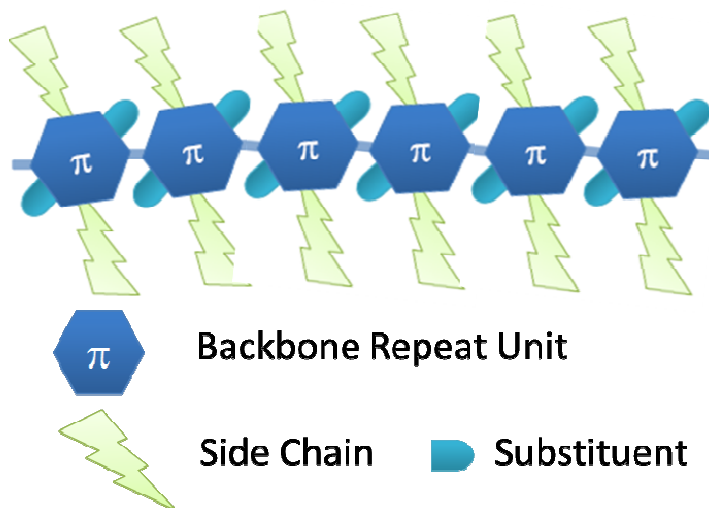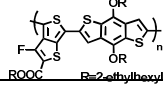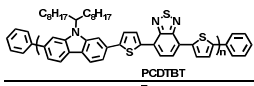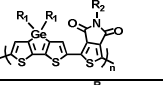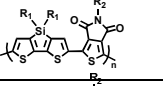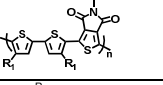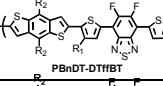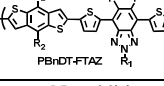
Figure 1.4. Illustration of a typical conjugated polymer for the application in organic solar cells

3.1.1. Development of Conjugated Backbone

The conjugated backbone is the most important component because it dictates most of the polymer solar cell-related physical properties of the conjugated polymer, such as energy levels, band gap and molecular interactions. Hundreds of different backbones have been reported so far.[11-13] For example, early studies had been focused on poly(phenylenevinylene) (PPV) based polymers, such as MEH-PPV and poly[2-methoxy-5-(3'-7'-dimethyloctyloxy)-1,4-phenylenevinylene] (MDMO-PPV). The PCE of MDMO-PPV based BHJ solar cells reached over 3% – with a high V_{oc} of 0.82 V – by employing chlorinated solvents to control the morphology.[14,15] Unfortunately, the large band gap (over 2 eV) of PPV based polymers significantly limited the current achievable by BHJ solar cells. A new polymer, regioregular poly(3-hexylthiophene) (P3HT), with a narrower band gap (1.9 eV) and thereby higher achievable J_{sc} became the new focus of intensive studies. By the careful control of the morphology of the Donor-Acceptor

blended thin films via thermal[16] or solvent annealing,[17] the efficiency of P3HT based BHJ devices was able to reach over 5%.[18,19] Recognizing that a smaller band gap polymer can absorb more light with potentially much higher efficiency, the focus of new materials development has been shifted to conjugated polymers of smaller band gaps. The heavy investment in the research of small band gap polymers has paid off quite well: a number of new polymers have shown over 7% PCE in BHJ solar cells (Table 1.1),[12,20-28] with over 9% being reported in the press.[29]

Table 1.1. Best performing polymers for BHJ solar cells

Polymer	HOMO (eV)	E_{gap} (eV)	V_{oc} (V)	J_{sc} (mA/cm^2)	FF [b]	η (%)	Ref.
ROOC R=2-ethylhexyl	− 5.15	1.6	0.74	14.50	0.69	7.4 (C70) 8.4 (C70)	21 20
PCDTBT	− 5.5	1.88	0.88	10.6	0.66	6.1 (C70) 7.2 (C70)	23 24
	− 5.60	1.69	0.85	12.6	0.68	7.3 (C70)	25
	− 5.57	1.73	0.88	12.2	0.68	7.3 (C70)	26
	− 5.56	1.82	0.92	13.1	0.61	7.3 (C70)	27
PBnDT-DTffBT	− 5.54	1.7	0.89	12.8	0.62	7.2 [a]	30
PBnDT-FTAZ	− 5.36	2.0	0.79	12.45	0.72	7.1 [a]	28

a. No additives were added. PC$_{61}$BM was used. b. *FF*: fill factor

1.3.2 Side Chains Are NOT Trivial

It is well-known that decorating the polymer backbone with side chains can effectively improve the solubility of the polymer, which is a crucial prerequisite toward achieving high molecular weight of the resulting conjugated polymer. However, substituting the small hydrogen atoms on these aromatic units with rather big alkyl or

alkoxy chains often result in significant steric hindrance between these aromatic units on the conjugated backbone. For example, a computational simulation revealed that severe steric hindrance introduced by these alkyl/alkoxy chains on the 4,7-di(thiophen-2-yl)benzothiadiazole (DTBT) lead to a twisted conjugated backbone in polymers incorporating the substituted DTBT.[31] Therefore the hole mobilities of the polymers incorporating such substituted DTBT were noticeably lower than that of the polymer with un-substituted DTBT, which accounted for a smaller J_{sc} in the former case.[31] In an earlier study, the homopolymers of alkylated DTBT were prepared by Jayakannan *et al.* by varying alkyl chains on either 3 or 4 positions of the thienyl groups.[32] Though relatively high molecular weight polymers were obtained, the steric hindrance introduced by these alkyl chains in these polymers led to much larger band gaps than that of the homopolymer of un-substituted DTBT.[33] Later, Wang *et al.* synthesized a series of internal donor-acceptor type of copolymers containing benzothiadiazole (BT) and four thiophenes incorporating side chains on different position.[34] Despite indentical alkyl side chains, the positions where these alkyl side chains are attached to different thiophene rings have significant influence on the physical properties and photovoltaic performance of resulting polymers. Positioning these alkyl chains close to the fluorene renders large steric hindrance during polymerization, which results in a significantly lower molecular weight in PFO-M2 and consequently a poor performance of 0.74% compared with 1.82% in PFO-M1 and 2.63% in PFO-M3.

Most recently, You and co-workers systematically investigated what effect the side chain positions had on the optical, electrochemical, and photovoltaic properties of conjugated polymers using PBDT-DTBT as the model polymer (Fig. 1.5).[35] Not

surprisingly, attaching alkyl chains greatly improved the solubility of resulting polymers; however, the anchoring positions significantly impacted the photovoltaic properties in BHJ solar cells. As discussed earlier, anchoring solubilizing chains at the inner core of DTBT introduces significant steric hindrance along the conjugated backbone, leading to anincrease in the band gap. Moreover, the electron density of HOMO energy levels of PBDT-3DTBT and PBDT-DTsolBT are essentially localized on the BDT unit, indicating a lack of delocalization. Therefore low efficiencies were observed for both PBDT-3DTBT (0.21 %) and PBDT-DTsolBT (0.01 %). On the other hand, shifting alkyl chains to the 4 positions of the flanking thienyl groups (PBDT-4DTBT) has a minimal impact on the band gap and energy levels when compared with PBDT-DTBT. Due to its increased solubility, PBDT-4DTBT possesses a higher molecular weight (Mn: 27 kg/mol) and shows enhanced intermixing with PC61BM, without the severe aggregation of polymers observed with PBDT-DTBT. Therefore, PBDT-4DTBT based solar cells result in an overall efficiency of 1.83%, which is significantly higher than that of the PBDT-DTBT based devices (0.72 %). These results present a good example of how the positioning side chains does in fact matter.
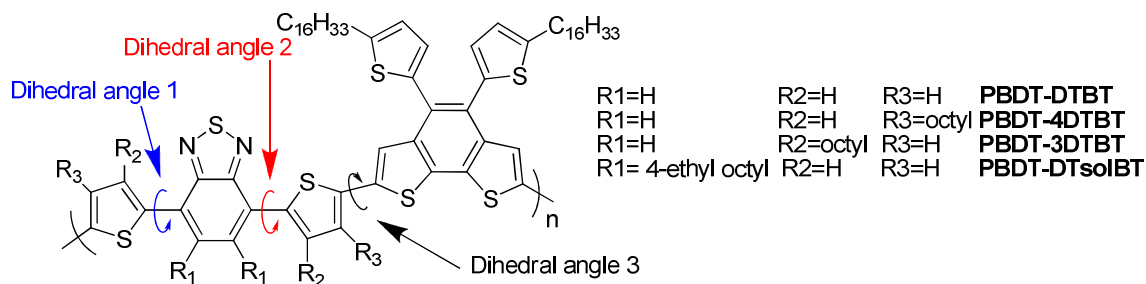
Figure 1.5. Chemical structures of PBDT-DTBT, PBDT-4DTBT, PBDT-3DTBT and PBDT-DTsolBT.

Even when the side chains are "properly" anchored on the conjugated backbone, the length and shape of these side chains also have a noticeable (sometimes substantial) impact on the properties of resulting conjugated polymers. Gadisa et al. completed a comparative investigation on the photovoltaic properties of BHJ devices based on a series of poly(3-alkylthiophene)s of butyl (P3BT), pentyl (P3PT) and hexyl (P3HT).[36] The longer side-chains facilitate the clustering of $PC_{61}BM$ molecules and establish fast electron-percolation pathways, leading to improved electron mobility. Since holes and electrons exhibit well-balanced mobilities in the case of P3HT: $PC_{61}BM$, a better fill factor was observed. In another study, Egbe et al. grafted different side chains to the backbone of a series of anthracene-containing poly(p-phenylene-ethynylene)-alt-poly(p-phenylene-vinylene)s (PPE-PPV) copolymers to tune the π–π stacking ability of the materials.[37] An increase of the open circuit voltage from ~0.65 V to ~0.90 V was observed with decreasing side chain density. It is because high density side chains dilute the concentration of the absorbing conjugated species per volume unit and reduce the interfacial area between donor polymer and $PC_{61}BM$ leading to strong phase separation and concomitant poor photovoltaic performance.

1.3.3. Importance of Substituent

Though the energy levels and band gap of a conjugated polymer is mainly determined by the selection of conjugated aromatic units, substituents can be used to further tune energy levels, band gaps, molecular interaction and even morphology.

Using archetypical poly(p-phenylene-vinylene) (PPV) as the model polymer, the substituent effect on conjugated polymers was systematically studied by Bredas and Heeger with the valence effective Hamiltonian (VEH) method.[38] Attaching electron

donating methoxy groups to the benzene unit of the PPV would raise the highest occupied molecular orbital (HOMO) energy level when compared with the original PPV (with similar lowest unoccupied molecular orbital (LUMO) level). This effect was also observed experimentally.[39] When switching to the electron withdrawing group (such as cyano), stabilization on both HOMO and LUMO levels would be expected. However, calculations found that the band gaps of the cyano PPVs would be larger than that of PPV, because of the asymmetry in the stabilization of the HOMO and LUMO levels by the cyano substituent. Furthermore, the position of the cyano (either on the phenylene or on the vinylene) affects the energy levels and band gap. When cyano was added on the vinylene, the calculated LUMO level was noticeably lower than that of the analog with cyano on the phenylene, with less difference on the HOMO energy levels. The authors attributed this effect to the different number of π electrons on the vinylene and phenylene. Since vinylene unit only has two π electrons whereas phenylene unit has six, substitution on the vinylene would introduce a relatively larger perturbation to the conjugated backbone, further lowering the LUMO level. All these results presented above indicate that electron donating substituents (such as methoxy) would have a more significant impact on the HOMO level, while electron withdrawing ones (such as cyano) would affect more strongly on the LUMO level.

Another interesting substituent is the fluorine. Fluorine is the smallest electron withdrawing group with a van der Waals radius of 1.35 Å and a Paul electronegativity of 4.0. Fluorinated organic molecules exhibit a series of unique features such as great thermal and oxidative stability,[40] elevated resistance to degradation,[41] enhanced hydrophobicity and high lipophobicity in perfluorinated substances.[42] In addition, these

fluorine atoms often have a great influence on inter- and intramolecular interactions via C-F···H, F···S and C−F···π_F interactions.[41,43] Applying fluorine substitution in the D-A polymers was investigated by You and co-workers in two recent studies.[28,30] In one report, they added two fluorine atoms to the commonly employed benzothiadiazole (BT), converting BT into fluorinated benzothiadiazole (ffBT).[30] The ffBT based polymer showed decreased HOMO and LUMO levels but a similar band gap when compared with those of its non-fluorinated analog. Preliminary PV tests on BHJ devices demonstrated both increased V_{oc} (0.91 V) and J_{sc} (12.9 mA/cm^2). Together with an also enhanced fill factor of 0.61, an impressive PCE of 7.2% was thus obtained without special treatments. In another related study, BnDT based copolymers (PBnDT-FTAZ) with 5,6-difluoro-2H-benzo[d][1,2,3]triazole (FTAZ) as the acceptor unit was synthesized.[28] This polymer exhibited a medium band gap of 2.0 eV compared with that of the DTBT based polymer due to the weaker electron affinity of FTAZ. Surprisingly, in spite of a band gap of ~ 2.0 eV, the current of PBnDT-FTAZ could be larger than 12 mA/cm^2 (depending upon the thickness of the active layer), which can be explained by its high molecular weight and large hole mobility. The BHJ devices based on PBnDT-FTAZ consistently showed a higher FF and J_{sc} than those of devices based on the polymers without fluorine substituents at comparable thicknesses. A peak PCE of 7.1% was obtained in BHJ devices of PBnDT-FTAZ:PC$_{61}$BM without annealing and any additives. Remarkably, PBnDT-FTAZ:PC$_{61}$BM solar cells can still achieve over 6% efficiency even at an unprecedented thickness of 1 μm (of the active layer), which makes PBnDT-FTAZ an excellent polymer for tandem solar cells.

1.4. Hole Transport Layers (HTL) in BHJ Polymer Solar Cells

The electrical properties at the interfaces are critical for governing solar cell performances, because the contact resistance between the organic photoactive layer and the electrode can strongly impact the charge collection, which is one of the fundamental steps of energy conversion in BHJ solar cells. In addition, anode/cathode interfacial layers are used as charge selective contacts between the BHJ active layer and the electrodes. Typically, a thin layer of PEDOT:PSS is applied in between the ITO and the active layer to improve the electrical contact between the ITO and the active layer and to adjust energy levels.[10] However, a number of drawbacks exist with this approach that limits the application of polymer solar cells: the acidic nature of PEDOT:PSS can corrode the ITO electrode,[44,45] leading to a chemical instability at the interface,[46] and PEDOT:PSS does not have sufficient electron blocking capability,[45] which could render electron leakage at anode to reduce the J_{sc}.

The research community has proposed several new interfacial layers as viable replacements for PEDOT:PSS for polymer solar cells applications.[24,27,47-54] For example, a self-doped, grafted conductive copolymer (PSSA-g-PANI), has been reported for photovoltaic applications. The conductivity and acidity of this copolymer can be easily tuned by varying the PSSA and PANI molar ratio.[55] Most importantly, OPV devices based on optimized PSSA-g-PANI film exhibited better thermal stability and efficiency than those of the PEDOT:PSS-based control device. PSSA-g-PANI can also be doped by introducing perfluorinated ionomer (PFI). Devices based on the PFI-doped PSSA-g-PANI showed a more than 30-fold increase in lifetime compared to the PEDOT:PSS based device. In addition to conductive polymers, p-Type transition metal oxides such as

vanadium oxides (V_2O_5)[56], nickel oxides (NiO_x)[57], and molybdenum oxide (MoO_3)[24,47] have also been used as another class of hole transport layer for OPVs. Compared with PEDOT:PSS, these large bandgap metal oxides possess better optical transparency in the visible and near infrared regions. In addition, the conduction band of these p-type semiconducting oxides is sufficiently higher than the LUMO of acceptor materials, which can effectively work as electron blocking layer, leading to small electron leakage through the anode. However, most of the p-type metal oxide films required vacuum deposition processes, which are incompatible with the high throughput printing processes. Recently, low temperature and solution-based NiO_x films were prepared by a sol–gel method with thermal annealing at moderate temperatures, followed by O_2 plasma treatment. The NiOx films successfully worked as HSL in the polymer BHJ devices,[58,59] with a very promising high PCE (6.7%). The NiO_x-based devices have better stability than those PEDOT:PSS-based devices due to improved hole selectivity and contact. As discussed above, interface layer plays a very important role for improving the efficiency and stability of OPVs. Therefore, design of interfacial materials is an important research topic.

1.5. Transparent Conductive Electrode for BHJ Polymer Solar Cells

The conventional anode of choice for organic solar cells has been indium tin oxide (ITO) due to its excellent transparency and conductivity. However, ITO has several longstanding disadvantages. First, the cost of ITO thin films is very high, primarily because ITO thin films must be vapor-deposited at rates orders of magnitude slower than solution-based coating processes. Second, indium is a relatively scarce element. Third, the brittleness of ITO renders it susceptible to mechanical damage, making it unsuitable

for use with mobile, flexible electronic systems.[60] Therefore, a critical roadblock to the commercialization of OPVs is the transparent conductive electrode.

Since 2004, steady improvements have been made in the research and development of transparent electrodes based on nanoscale carbon-based materials including single-wall carbon nanotubes (SWNT), multiwall-carbon nanotubes (MWNT), and grapheme.[61-68] A sheet resistance of several hundred $\Omega/\square$ at 80% optical transmittance in the visible range, achievable in these multiwall-carbon nanotubes (MWNT) and grapheme electrodes, is used in solar cells, ending up with a relative low efficiency.[64,68] Great progress of the SWNT films have been developed have transmittance of 85% in the visible and sheet resistance of 200 $\Omega/\square$ with achieved power efficiency of 2.5 %, a printing method was required to transfer carbon-based materials to transparent substrates, which complicates the processing procedures and potentially increases the cost of OPVs. More recently, metal nanogrids based on copper and silver have been developed as high transparent electrode with pretty low sheet resistance.[69,70] More recently, a high-performance transparent electrode (90 % at 50 $\Omega/\square$) based on electrospun copper nanofiber networks was developed.[71] Organic solar cells using these copper nanowire networks as transparent electrodes have reached power efficiencies of 3.0 %, comparable to control devices made with ITO electrodes. The solution processed silver nanowire (Ag NW) networks have been developed with low sheet resistance of 10-20 $\Omega/\square$ at 80 % transmittance recently.[72-74] With a very low processing and materials cost, and a relative high work function around 4.6 eV, Ag NW transparent electrode is a promising alternative to replace ITO anode for large area applications and roll-to-roll processing. The solution-processed Ag NW transparent electrodes have been used recently as cathode

electrode on top of BHJ devices[75] and anode electrode on top of invert cells.[76] And, it was successfully developed as anode electrode underneath a vacuum deposited bilayer solar cells.[72]

1.6. Tandem and Multi-blend Solar Cells

The first prerequisite to achieving high efficiency in any types of solar cells is that the solar radiation is absorbed efficiently by the active layer. In a typical BHJ polymer solar cell which employs a conjugated polymer as a p-type semiconductor and a fullerene derivative as the n-type semiconductor, the polymer is the major light absorber. However, the intrinsic narrow absorption width of these conjugated polymers, usually with a full width at half maximum (FWHM) on the order of 200 nm,[77] can only overlap with a small fraction of the solar spectrum. This in-efficient light absorption leads to noticeably low current (usually around 10 mA/cm^2) when compared with other types of high efficiency solar cells (e.g., over 40 mA/cm^2 in crystalline Si solar cell), which limits the further improvement on the efficiency of polymer solar cells. One simple approach to increase the absorption breadth of a polymer solar cell is to blend multiple donor components of different absorption features (ideally complementary), into a BHJ with phenyl-C$_{61}$-butyric acid methyl ester (PC$_{61}$BM) as the electron acceptor. Recently, this simple method has been successfully demonstrated by the addition of a small fraction (1 – 20%) of dye molecules or a small band gap polymer into the archetypical poly(3-hexylthiophene) (P3HT)/PC$_{61}$BM BHJ cells.[78,79] In these ternary or even quaternary blend systems, both the dye molecules and the small band gap polymer act as the "guest" sensitizer to improve the light absorption of the "host" P3HT based BHJ. It was believed

16

that additional excitons generated by these sensitizers would dissociate with $PC_{61}BM$, and these extra charge carriers (holes) were able to transport to the anode via the dominant P3HT phase. This requires these "guest" sensitizers to have their HOMO and LUMO levels in between the corresponding energy levels of the P3HT and those of the $PC_{61}BM$ (Fig. 1.6). Such a cascade energy level alignment is necessary to prevent the possible energy transfer among components in the BHJ blend, and to ensure efficient exciton splitting and charge transport to the electrodes.
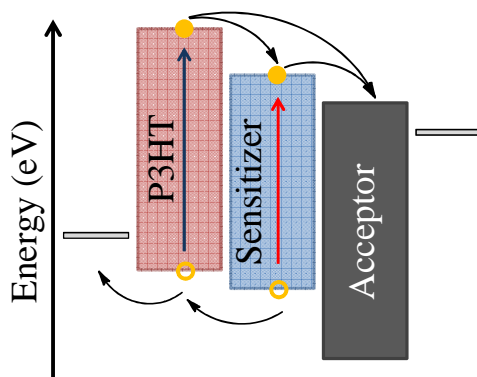
Figure 1.6. Energy diagram electrodes and semiconductors used in ternary blends. Curved arrows indicate allowed charge transfer reactions in the multi-blend system.

Compared with the multi-blend system, tandem cells offer a more effective approach to broaden the light absorption and enhance its utilization.[80] This is because tandem cells stack multiple sub-cells in either series or parallel connection such that each sub-cell incorporating a polymer absorbing specific range of the solar spectrum (Fig. 1.7).[81-83] Each sub-cell works individually without any energy or charge transfer between each other, significantly reducing the thermalization losses in the multi-blend system.[79] Further, this important feature of tandem cells – independent working sub-cells – essentially lifts the restrictions on the design and selection of materials in the multi-blend system, allowing versatile materials selections and device designs. Specifically, a serially

connected tandem cell benefits from a significantly higher V_{oc}, which is the sum of those from each sub-cell; however, the J_{sc} of such a device is pinned to the smallest J_{sc} among those individual J_{sc} from sub-cells.[84] On the other hand, the J_{sc} in a parallel connected tandem cell combines those from each sub-cell, whereas the V_{oc} is in between those of single sub-cells.[85-88]
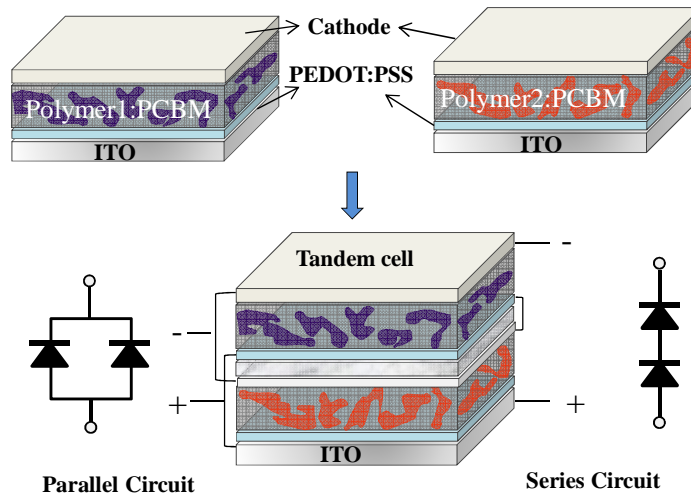
Figure 1.7. Schematic structure of polymer tandem cells.

1.7. Challenges and Objectives

It is generally agreed that further increases in efficiency will be required before these polymer solar cells can become competitive with their thin film inorganic counterparts. Several research groups have tried to predict the maximum attainable efficiency that can be achieved with polymer/fullerene BHJ solar cells,[12,20-28,30] although different methods have been used, most estimates are between 10 and 11%. A specific route toward such efficiencies is not well-defined, although it does appear that development of new polymer and fullerene derivatives will be required. Such development must be based on a new set of more detailed design principles that can only be established through the rigorous

elucidation of the fundamental physical principles that govern the photovoltaic process. In addition to higher efficiency of polymer solar cells, long lifetime and large scale roll-to-roll manufacturing for polymer solar cell are also critical for commercialization of polymer solar cells in near future. Therefore, design of device structure and interfacial layer for polymer solar cells is required to meet the solution-processed roll-to-roll manufacturing and to improve the stability of polymer solar cells.

The creative design and synthesis of conjugated backbones has received the greatest amount of attention and has driven the efficiency of BHJ solar cells to record highs, however, the investigate on side chains and the substituents are quite empirical. Since both side chains and the substituents are key constituting components of conjugated polymer, optimization of side chains and the substituents can maximize the energy harvesting potential of a given conjugated backbone in its BHJ devices. In Chapter 2 and 3, we will quantitatively analyse the influence of side chains and fluorine substituents on the photovoltaic performance of polymer solar cells. Moreover, interfacial layer of PEDOT:PSS is commonly applied in between the ITO and the active layer to improve the electrical contact between the ITO and the active layer and to adjust energy levels, however, the acidic nature of PEDOT:PSS tends to corrode the ITO electrode, leading to a chemical instability at the interface. In order to extend the lifetime of polymer solar cells, we will try to replace PEDOT:PSS with a much more stable hole transport layer in Chapter 4. Another critical roadblock that stands in the way of commercialization in OPVs is the ITO anode electrode which is expensive and does not have required flexibility[8] for low-cost roll-to-roll manufacturing. Therefore, we will focus on promising alternative to ITO as the anode electrode in Chapter 5. In addition to the typical single

junction solar cells, tandem cells that stack multiple conjugated polymers can effectively harvesting the solar energy than the single junction cells.[81-83] However, the concomitant issues with tandem cells such as device complexity and increased cost of fabrication[89-91] significantly impair the commercial viability of this technology. In Chapter 6, we will demonstrate a conceptually new approach which maintains the simple device configuration and low cost processing of single junction BHJ cells while inherits the major benefit of incorporating multiple polymers in tandem cells.

.

CHAPTER 2

QUANTITATIVELY ANALYZING THE INFLUENCE OF SIDE CHAINS OF CONJUGATED DONOR POLYMERS ON THE PERFORMANCE OF PHOTOVOLTAIC [*]

2.1. Introduction

The efficiency of all solar cells is determined by the simple equation:

$$\eta = \frac{J_{sc} \times V_{oc} \times FF}{P_{input}}$$. To the first degree of approximation, J_{sc} is dictated by the band

gap of the light-absorbing materials in the solar cell, while V_{oc} is closely related to the

energetics (i.e., energy levels) of the materials used. The third parameter, *FF*, is

determined by the shunt and series resistance of the solar cell[92]. In the prevailing bulk

heterojunction (BHJ) configuration for organic solar cells, typically consisting of a

polymer and a fullerene derivative, the J_{sc} and V_{oc} are decided by the band gap and the

HOMO energy level of the conjugated polymer[93]. Therefore, engineering the band gap

and energy levels of conjugated polymers has been an extremely active research direction

under intense scrutiny. Within this area, impressive progress has been achieved; for

example, the record high efficiency for organic solar cells has been constantly

updated[12,14,16,17,21,23,94], and the ever-increasing database of polymers for BHJ solar cells

has led to a reasonably organized design rationale[95-97]. However, most of these

structure/property correlations are rather qualitative and empirical[93]; whereas the more

---

[*] Adapted with permission from *Journal of Physical Chemistry C,* 2010, 114 (39), 16793–16800, by Liqiang Yang, Huaxing Zhou, and Wei You

respected, rigorous and quantitative analyses of these structure/property relationships rarely appear in the literature[98,99].

Conventional wisdom dictates that the band gap and energy levels of a conjugated polymer are determined by the molecular structure of the conjugated backbone, while the solubilizing alkyl chains – if engineered properly – should have a negligible impact on these properties[35]. Therefore, the side chains should have minimal impact on the observed J_{sc} and V_{oc} in polymer based BHJ solar cells[36,100]. Contrary to the "conventional wisdom", we report here that the side chain plays a significant role in modulating the V_{oc} and J_{sc} of BHJ solar cells fabricated from polymers containing an identical conjugated backbone. The conjugated backbone of these polymers (PNDT-DTBT) is constructed following the weak donor-strong acceptor strategy[35,96,97], by alternating naphtho[2,1-*b*:3,4-*b'*]dithiophene (NDT) and 4,7-di(thiophen-2-yl)benzothiadiazole (DTBT) (Fig. 2.1). The alkyl chains are attached to the 4th position of these thienyl groups on DTBT to minimize the steric hindrance to the polymer backbone and hence to maintain near identical band gap and energy levels (as decided by the conjugated backbone)[35]. Surprisingly, the observed V_{oc} and J_{sc} of these PNDT-DTBT based BHJ devices vary as much as 100%, depending upon the length and shape of the alkyl side chains. Consequently, the overall efficiency of PNDT-DTBT polymers/PC$_{61}$BM based solar cells has shown a significant variation as much as 2.5 fold (from 1.20% to 3.36%). More importantly, the observed difference in V_{oc} and J_{sc} has been quantitatively correlated with a pre-exponential dark current term, J_{so}, which accounts for the intermolecular interactions in the polymer/PC$_{61}$BM blends[98]. The calculated V_{oc} and J_{sc} match the

experimental values within 10% error, which clearly demonstrate the predictive power of this quantitative analysis.

R1=2-hexyldecyl R2=octyl   C10,6-C8
R1=2-hexyldecyl R2=2-ethylhexyl C10,6-C6,2
R1=octyl   R2=octyl   C8-C8
R1=octyl   R2=dodecyl   C8-C12
R1=octyl   R2=2-ethylhexyl C8-C6,2
R1=2-ethylhexyl R2=2-ethylhexyl C6,2-C6,2
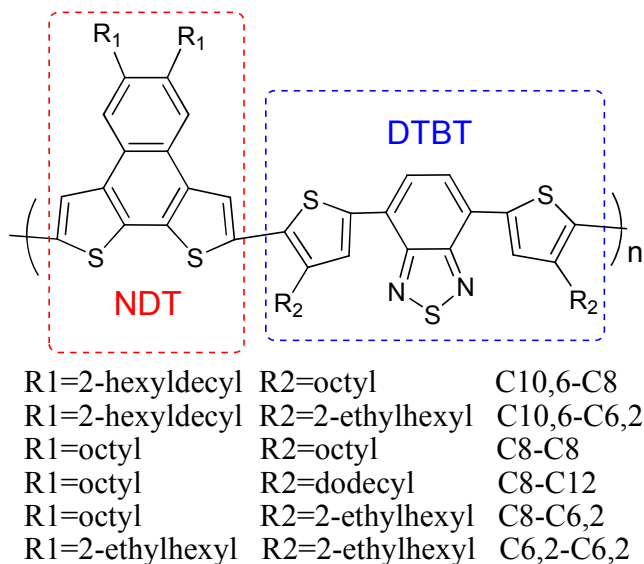
Figure 2.1. The chemical structures of the six polymers based on the PNDT-DTBT backbone.

2.2. Experimental Section

Glass substrates coated with patterned indium-doped tin oxide (ITO) were purchased from Thin Film Devices, Inc. The 150 nm sputtered ITO pattern had a resistivity of 15Ω/□. Prior to use, the substrates were ultrasonicated for 20 minutes in acetone followed by deionized water and then 2-propanol. The substrates were dried under a stream of nitrogen and subjected to the treatment of UV-Ozone over 30 minutes. A filtered dispersion of PEDOT:PSS in water (Baytron PH500) was then spun cast onto clean ITO substrates at 4000 rpm for 60 seconds and then baked at 140 °C for 10 minutes to give a thin film with a thickness of 40 nm. A blend of polymer and $PC_{61}BM$ (1:1 w/w, 10 mg/mL for polymers) was dissolved in chlorobenzene with heating at 100 °C for 6 hours. All the solutions were spun cast at 1100 rpm for 60 seconds onto PEDOT:PSS

layer. The substrates were then dried at room temperature in the glovebox under nitrogen atmosphere for 12 hours. The devices were finished for measurement after thermal deposition of a 30 nm film of calcium and a 70 nm aluminum film as the cathode at a pressure of $\sim 1\times10^{-6}$ mbar. There are 8 devices per substrate, with an active area of 12 mm^2 per device. Device characterization was carried out under AM 1.5G irradiation with the intensity of 100 mW/cm^2 (Oriel 91160, 300 W) calibrated by a NREL certified standard silicon cell. Current versus potential (I-V) curves were recorded with a Keithley 2400 digital source meter. EQE were detected under monochromatic illumination (Oriel Cornerstone 260 ¼ m monochromator equipped with Oriel 70613NS QTH lamp) and the calibration of the incident light was performed with a monocrystalline silicon diode. All fabrication steps after adding the PEDOT:PSS layer onto ITO substrate, and characterizations were performed in gloveboxes under nitrogen atmosphere. For more experimental details about reagents, instrumentation, electrochemistry, and spectroscopy please check **Appendix A**.

2.3. Optical and Electrochemical Properties of Polymers
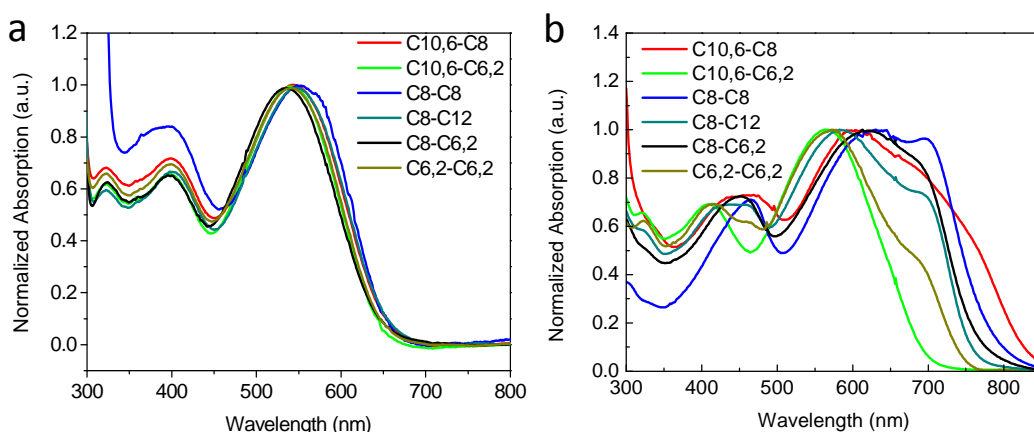
Figure 2.2. Normalized absorption spectra of polymer solutions in trichlorobenzene at a) 140 ºC and b) room temperature.

At high temperature and in good solvent, the effect of solubilizing chains on conjugated polymers has little impact on the optical properties since the polymers are adequately solvated. Thus all absorption spectra of these polymers collapse together, indicative of the identical PNDT-DTBT backbone (Fig. 2.2a). However, dramatic effects were observed on the optical properties of polymer, when these polymer solutions of identical concentration are cooled to room temperature. For example, polymer C8-C8 with short straight side chains exhibits much stronger aggregation when compared with C10,6-C6,2, as indicated by a pronounced absorption increase at longer wavelengths from about 700 nm to almost 800 nm. The observed differences on the optical properties of polymer with different size of side chains will be further discussed in the following sections.
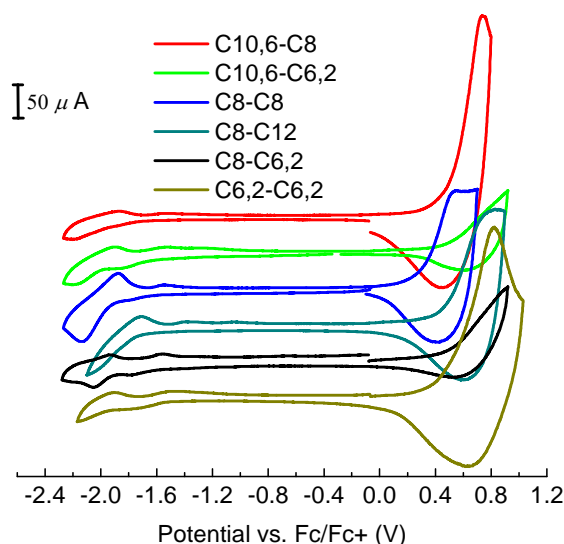
Figure 2.3. Cyclic voltammograms of the oxidation and reduction behavior of thin films

The polymerization results of all polymers are listed in Table 2.1. The synthesis of all six polymers was controlled to get a similar molecular weight in order to minimize the effect of molecular weight on the photovoltaic performances. Probing this library of polymers with identical conjugated backbone via cyclic voltammetry provides direct evidence on how the difference in shape and length of these alkyl chains affects the

energy levels of these related polymers (Fig. 2.3). Table 2.1 summarizes the energy levels of LUMO and HOMO observed from cyclic voltammetry and computational study (see **Appendix B Fig. B.1**). The calculated values of the HOMO and LUMO exhibit similar trend to the corresponding experimental data, a clear indication of the viability and effectiveness of these electrochemical data. Interestingly, the shape and length of attached solubilizing alkyl chains on the DTBT unit seemingly has little impact on the electrochemical properties of related polymers, due to the limited steric hindrance introduced by the side chain on 4th position of the polymer backbone.[35]

Table 2.1. Calculated and measured electrochemical data of all polymers.

Polymer	Mn (Kg/mol)	PDI	HOMO(eV) Cal	HOMO (eV) Exp	LOMO (eV) Cal	LOMO (eV) Exp
C10,6-C8	11.9	1.83	-5.15	-5.32	-2.85	-3.12
C10,6-C6,2	10.6	1.77	-5.16	-5.33	-2.89	-3.20
C8-C8	12.4	2.23	-5.04	-5.13	-2.86	-3.19
C8-C12	15.4	3.03	-5.02	-5.27	-2.84	-3.12
C8-C6,2	5.24	1.91	-5.16	-5.30	-2.88	-3.21
C6,2-C6,2	6.76	2.07	-5.17	-5.34	-2.90	-3.26

2.4. Measured and Calculated Photovoltaic Properties of All Devices

The generalized Shockley equation (equation (2.1))[101,102] can be used to describe the current density (J) vs. voltage (V) characteristics of organic solar cells:

$$J = \frac{R_p}{R_s + R_p}\left\{ J_s \left[\exp\left(\frac{q(V - JR_s)}{nkT} \right) - 1 \right] + \frac{V}{R_p} \right\} - J_{ph}(V) \qquad (2.1)$$

Here, R_p is the parallel resistance, R_s is the series resistance, J_s is the saturation current density, q is the fundamental charge, n is the diode ideality factor, and $J_{ph}(V)$ is the

voltage-dependent photocurrent density. The saturation current density J_s, which is the current resulting from carriers generated thermally at the Donor/Acceptor interface, has been shown to vary exponentially with energy barrier (ΔE_{DA}) – the energy difference between the LOMO level of the Acceptor and the HOMO level of the Donor. Therefore, J_s can be represented by equation (2.2)[98,102-105] for systems, where J_s is dominated by the recombination, as observed for most organic solar cells[101,102,104]

$$J_s = J_{so} \exp\left(\frac{-\Delta E_{DA}}{2nkT}\right) \tag{2.2}$$

The magnitude of the pre-exponential term, J_{so}, depends on a number of materials properties that determine the carrier generation/recombination rate, independent of ΔE_{DA}. Since the studied polymers have the identical PNDT-DTBT backbone with only difference in the alkyl side chains, J_{so} is believed to represent the strength of intermolecular interactions determined by the intermolecular packing and ordering.

At open circuit conditions ($J=0$, $V=V_{oc}$), substitution of equation (2.2) into equation (2.1) and assuming both a minimal leakage current ($R_p \gg R_s$), and a short circuit current $J_{sc} = J_{ph}(V) \gg J_s$, equation (1) can be simplified and further solved to offer equations (2.3)[98,103,105,106] and (4), in which V_{oc} and J_{sc} are given by:

$$V_{oc} \approx \frac{nkT}{q} \ln\left(\frac{J_{sc}}{J_{so}}\right) + \frac{\Delta E_{DA}}{2q} \tag{2.3}$$

$$J_{sc} \approx J_{so}\left[\exp\left(\frac{2qV_{oc} - \Delta E_{DA}}{2nkT}\right)\right] + \frac{V_{oc}}{R_p} \tag{2.4}$$

Equation (2.3) suggests a logarithmic dependence of the V_{oc} on J_{sc} and J_{so} in the first

term and a linear dependence of the V_{oc} on the interface energy difference (ΔE_{DA}) in the

second term. Clearly, to achieve the maximum possible V_{oc} for a given Donor/Acceptor

pair, J_{so} must be *minimized*. On the contrary, a *large J_{so}* is required for the maximum

possible J_{sc} according to equation (2.4). However, because other parameters (i.e.,

molecular weight and solubility) also contribute to the attainable J_{sc}, the relationship

between J_{so} and the observed J_{sc} is more complex in practical BHJ devices than what is

described in equation (2.4)[98].

Table 2.2. Measured and calculated performance parameters for all devices. [a]

Polymer	Jso (mA/cm^2)	n	$\frac{nkT}{q}\ln\left(\frac{J_{SC}}{J_{SO}}\right)$	$\frac{\Delta E_{DA}}{2q}$	Voc (V) Cal	Voc (V) Exp	Jsc (mA/cm^2) Cal	Jsc (mA/cm^2) Exp
C10,6-C8	148	2.16	-0.16	0.76	0.60	0.59	7.05	7.98
C10,6-C6,2	3.38	4.90	0.06	0.77	0.83	0.81	5.02	5.62
C8-C8	399	2.64	-0.28	0.67	0.39	0.41	9.75	6.97
C8-C12	254	2.12	-0.21	0.74	0.53	0.52	5.22	5.88
C8-C6,2	68.8	3.17	-0.15	0.75	0.60	0.59	10.04	10.93
C6,2-C6,2	22.6	3.51	-0.07	0.77	0.70	0.69	9.58	10.67

[a] Devices were obtained using polymer and $PC_{61}BM$ blend with 1:1 weight ratio. The interface gap, ΔE_{DA}, was calculated using $PC_{61}BM$ lowest unoccupied molecular orbital (LUMO) value which is 3.8 eV as we measured.

Having laid out the foundation, we applied these equations our library of polymers

(PNDT-DTBT), to compare the experimental results with the predicted values from these

equations, with ultimate goal of quantitatively explaining the observed difference in

photovoltaic properties. In practice, the measured dark current-voltage characteristics

were first fit into the generalized Shockley equation (2.1) to extract n and J_s (Table 2.2).

Then the calculated values of J_{so}, V_{oc}, and J_{sc} were derived from equation (2.2), equation

(2.3), and equation (2.4), respectively. The results are listed in Table 2.2, together with corresponding experimental values. The calculated values of the V_{oc} match the corresponding experimental data exceptionally well (less than 5% difference), a clear indication of the viability and effectiveness of this simulation for V_{oc}. A noticeable discrepancy between the calculated and the experimental values has been observed in the case of J_{sc}, however, the calculated J_{sc} values exhibit a similar trend as the corresponding experimental data. This indicates there are other factors involved in the attainable J_{sc} in practical BHJ devices. Furthermore, J_{so} – a parameter that is determined by the intrinsic properties of donor polymers – is proposed to quantitatively explain the intermolecular interaction introduced by the side chain. We believe this is the first time such quantitative analysis has been used to explain the dramatic impact on photovoltaic properties solely caused by the side chains.

Table 2.3. Photovoltaic performances of all polymer-based devices.

Polymer	Polymer: $PC_{61}BM$	Thickness (nm)	Voc (V)	Jsc (mA/cm²)	FF (%)	η (%)
C10,6-C8	1:1	75	0.59	7.98	46.05	2.17
C10,6-C6,2	1:1	85	0.81	5.62	44.07	2.01
C8-C8	1:1	110	0.41	6.97	42.05	1.20
C8-C12	1:1	65	0.52	5.88	42.09	1.28
C8-C6,2	1:1	75	0.59	10.93	46.43	3.00
C6,2-C6,2	1:1	65	0.69	10.67	45.90	3.36

Since the repeating unit of PNDT-DTBT consists of two structural units, NDT and DTBT, we arbitrarily sub-categorized these six polymers into three groups. Each group

contains two or three polymers with only variation of side chains on either NDT or DTBT (but not on both), in order to accurately analyze the effect of these side chains in a systematic fashion.

2.5. NDT with 2-hexyldecyl (C10,6) and DTBT with Various Alkyl Chains

In this group, a long branched chain (C10,6) is attached to the structural unit NDT, while another eight carbon chain is anchored on the DTBT. The two polymers studied in this group are structural isomers, with only a small difference in the shape of the alkyl chain attached to DTBT (straight C8 vs. branched C6,2). However, their corresponding photovoltaic properties are noticeably different (Table 2.3). Since all polymers exhibit similar mobility (see **Appendix B Table B.1**), the observed difference in photovoltaic properties can only be explained by the different intermolecular interaction in the solid state. For this reason, small angle X-ray diffraction (XRD) was used to probe the nanomorphology of the active layer. The peaks around 20º with strong intensity in the XRD spectra of the polymer- $PC_{61}BM$ blend is believed to arise from the $PC_{61}BM$ (Fig. 2.2b). The representative spacing of the (100) and (010) plane calculated from the spectra is listed in Table 2.4.
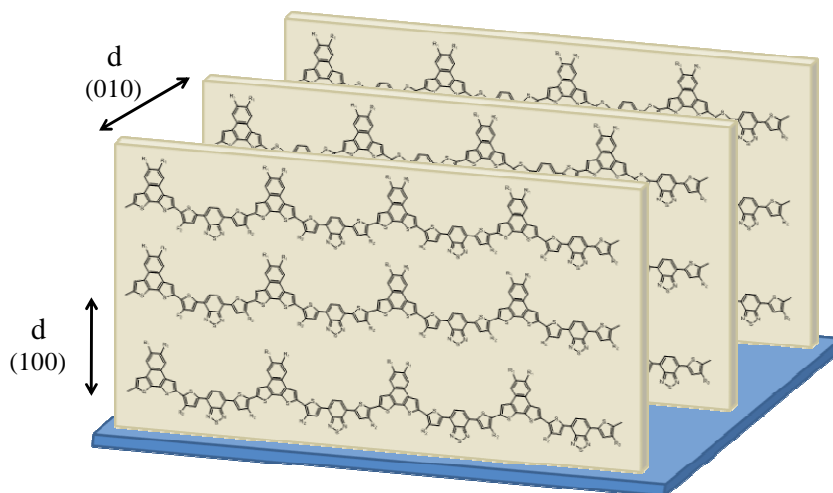
Figure 2.4. Schematic nanomorphology of active layer in BHJ devices.

As shown in the Fig. 2.4, the value of (100) spacing corresponds to the distance between PNDT-DTBT conjugated backbones, which is determined by the longest alkyl side chain. The fact that these two polymers with identical longest side chains of 2-hexyldecyl (C10,6) explains the observed similar (100) spacing. On the other hand, the distance between the coplanar π-conjugated polymers is represented by the value of (010) spacing. Unlike C10,6-C8 PNDT-DTBT showing an identifiable (010) peak, C10,6-C6,2 has a barely discernible (010) peak. This is because the branched alkyl side chain 2-ethylhexyl (C6,2) renders the (010) plane less planar and consequently decreases the intermolecular packing of the C10,6-C6,2 polymer. Moreover, C10,6-C6,2 has a larger (010) spacing than that of C10,6-C8 as shown in Table 2.4, implying a longer π overlapping distance which is also due to the bulky branch alkyl side chains (C6,2). Both the weak (010) peak intensity and the large value of (010) spacing in the C10,6-C6,2 polymer indicates a weak π-overlapping amongst individual conjugated polymer chains which results in weak intermolecular interaction. This weak intermolecular interaction explains the calculated small J_{so} in the case of C10,6-C6,2. In contrast, a much sharper

(100) peak and observable (200) and (300) peaks have been obtained for the C10,6-C8 polymer in both the polymer/PC$_{61}$BM blend and the pure polymer spectra than corresponding peaks in the C10,6-C6,2 polymer. Moreover, an additional small peak at 21° can be observed in the continual spectrum zone in the XRD spectrum of the C10,6-C8 polymer. These facts indicate the C10,6-C8 polymer has a higher percentage of polycrystalline nature in the solid state than the C10,6-C6,2, as corroborated by AFM (Fig. 2.5). Since J_{so} values can be magnitudes larger in polycrystalline materials than in amorphous materials[98], it is not surprising to observe that the J_{so} of the C10,6-C8 polymer with straight C8 chain on the DTBT is almost fifty times bigger than that of the C10,6-C6,2.
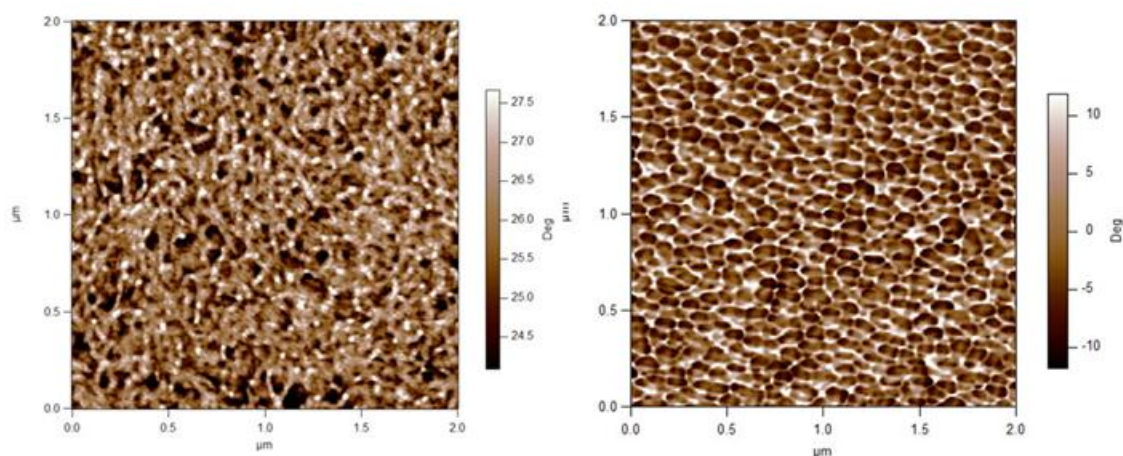
Figure 2.5. AFM phase images of C10,6-C8:PC$_{61}$BM film (left) and C10,6-C6,2:PC$_{61}$BM film (right).

Further evidence supporting stronger intermolecular interaction in the C10,6-C8 polymer is provided by the UV-vis spectra acquired in the solid state as thin films (Fig. 2.6c). At a glance, both polymers have similar absorption coefficients, indicative of a similar density of conjugated backbones in the solid state. This can be ascribed to the identical longest alkyl chain of C10,6 in both polymers (and further supported by a

similar value of (100) spacing), since the density of conjugated backbone in the thin film is largely decided by the longest side chains. However, unlike the UV-Vis absorption spectra of polymers in solutions at high temperature where all spectra overlapped, the size and branching of the side chains have a dramatic effect on the absorption spectra as thin films. The much stronger intermolecular interaction in the C10,6-C8 polymer than that of the C10,6-C6,2 leads to a pronounced increase in the absorption breadth, extending up to almost 850 nm (Fig. 2.6c), which is supportive of the calculated large J_{so} of the C10,6-C8 polymer (Table 2.2).

Table 2.4. Diffraction angles and related d-spacing obtained from XRD spectra.

Polymer	Polymer Only		Polymer: $PC_{61}BM$ (1:1)	
	(100)	(010)	(100)	(010)
	2θ (°)/d-spacing (Å)	2θ (°)/d-spacing (Å)	2θ(°)/d-spacing (Å)	2θ (°)/d-spacing (Å)
C10,6-C8	3.74/23.62	25.00/3.56	3.69/23.94	24.93/3.57
C10,6-C6,2	3.76/23.50	23.41/3.80	3.73/23.69	N/A
C8-C8	4.23/20.89	25.45/3.50	4.31/20.50	25.44/3.50
C8-C12	3.72/23.75	25.32/3.52	3.65/24.21	25.21/3.53
C8-C6,2	4.37/20.22	25.17/3.54	4.47/19.77	25.19/3.54
C6,2-C6,2	4.67/18.92	25.02/3.56	4.60/19.21	24.68/3.61

The seemingly negligible difference in the side chains (straight C8 vs. branched C6,2) has a significant impact on the current-voltage characteristics of solar cells fabricated from these polymers (Fig. 2.6d). For example, while the cyclic voltammetry (CV) measurements only discerned a very small difference on the HOMO energy level between the C10,6-C6,2 polymer and the C10,6-C8, a much bigger difference on the V_{oc} was observed between the C10,6-C6,2 polymer (0.81 V) and the C10,6-C8 (0.59 V). The

smaller J_{so} of the C10,6-C6,2 polymer, which rooted from the weaker intermolecular stacking of the conjugated polymer due to the branched C6,2 chain, contributes positively to the V_{oc} via the first term in equation (2.3). Similarly, the bigger J_{so} of the C10,6,-C8 polymer significantly reduces the V_{oc}. However, the impact of J_{so} is reversed when the short circuit current (J_{sc}) is concerned. A large J_{so} will help increase the J_{sc} via the first term in equation (2.4). Therefore, the J_{sc} of BHJ devices from the C10,6-C8 polymer is noticeably bigger than that of the C10,6-C6,2 polymer (Table 2.3). Qualitatively, the larger J_{sc} of the C10,6-C8 polymer can be explained via the UV-Vis absorption spectra: the strong intermolecular interaction in the C10,6-C8 polymer decreases the optical band gap and broadens the absorption spectrum, and hence increases the J_{sc}. The investigation of these two isomeric polymers reveals that a branched side chains can lead to a low J_{so}, resulting a high V_{oc}, while a straight side chain will facilitate a higher J_{sc} by increasing the J_{so} (also resulting in a decreased optical band gap).
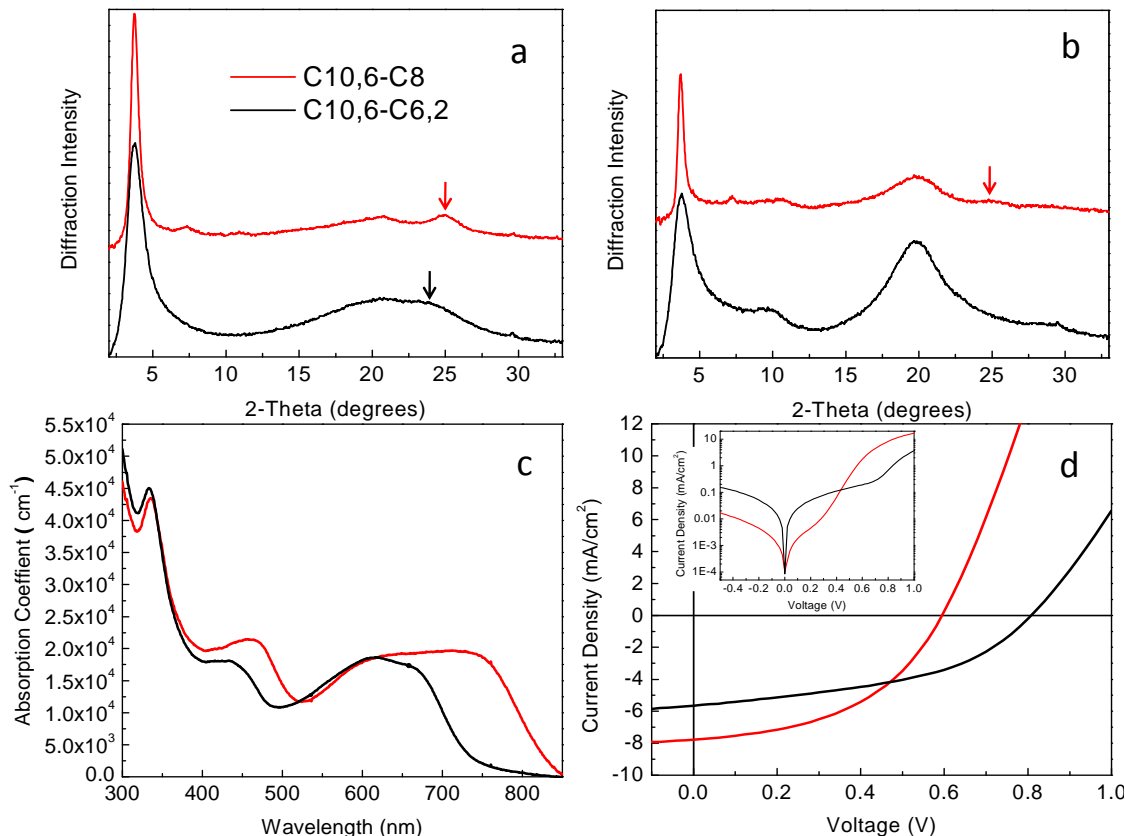
Figure 2.6. a) XRD spectra of the C10,6-C8 and C10,6-C6,2 polymers in thin films (arrows indicating (010) peaks). b) XRD spectra of C10,6-C8:$PC_{61}BM$ (1:1) and C10,6-C6,2:$PC_{61}BM$ (1:1) blends in thin films (arrows indicating (010) peaks). c) Absorption spectra of C10,6-C8:$PC_{61}BM$ (1:1) and C10,6-C6,2:$PC_{61}BM$ (1:1) blends in thin films. d) Current density vs. voltage characteristics in the dark (inset) and illumination under 1 sun, AM1.5 conditions for C10,6-C8 and C10,6-C6,2 polymer based BHJ solar cells.

2.6. NDT with Octyl (C8) and DTBT with Different Alkyl Chains

The study of the C10,6-C8 and C10,6-C6,2 polymers implied that shorter chains are beneficial to improving the J_{sc} via the increased density of conjugated backbone and the enhanced intermolecular interaction. Therefore, in section 2.6, short, straight alkyl chains (C8) were attached to the NDT in order to further improve the J_{sc}. As shown in Fig. 2.7a and b, (010) peaks with strong intensities are observed in all of these three polymers (C8-C8, C8-C12, and C8-C6,2), indicating that the short straight chains of C8 do enhance the

intermolecular packing compared with the branched chains of C10,6. In addition, the (010) spacing is further decreased in the C8-C8 polymer compared with that in the C8-C6,2 polymer, reiterating the stronger intermolecular interaction introduced by the straight alkyl chains on the DTBT as previously discussed. Therefore, the C8-C8 polymer with short straight alkyl chains on both NDT and DTBT units has the smallest (010) spacing among all studied six polymers, leading to the largest J_{so} value (Table 2.2). A small difference between the (100) spacing of the C8-C8 polymer and that of the C8-C6,2 is noticed, likely due to a shorter length of the branched chain of C6,2 on the DTBT than that of the straight chain of C8. However, the (100) spacing of the C8-C12 polymer is significantly longer than that of either the C8-C8 polymer or the C8-C6,2. This can be explained by the fact that the distance between conjugated polymer backbones is mainly dominated by the length of the longest side chain rather than other shorter chains. For example, the longest side chain in this study is dodecyl (a linear alkyl chain of 12 carbons), which is 4.98 Å longer than the longest side chain of octyl in polymers of C8-C8 and C8-C6,2. This gives rise to the observed difference of 3 – 3.5 Å in the (100) spacing.
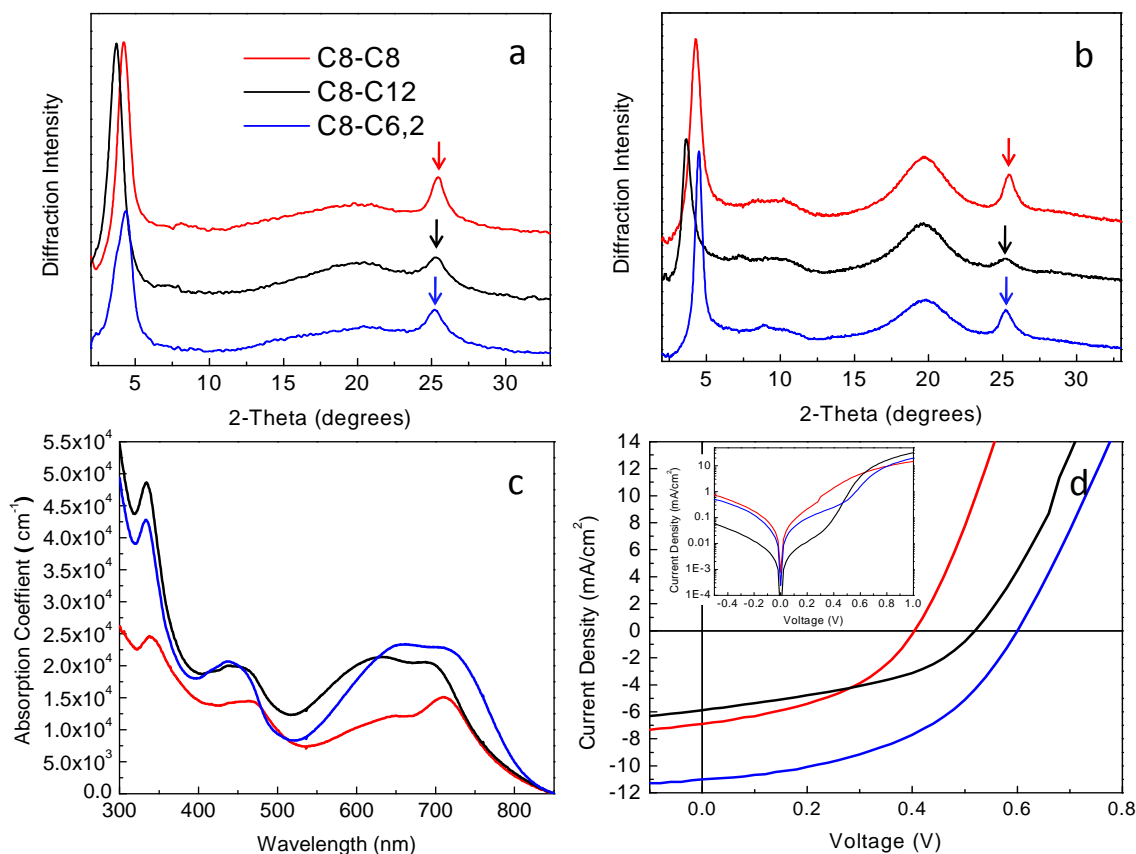
Figure 2.7. a) XRD spectra of the C8-C8, C8-C12, and C8-C6,2 polymers in thin films (arrows indicating (010) peaks). b) XRD spectra of C8-C8:$PC_{61}BM$ (1:1), C8-C12:$PC_{61}BM$ (1:1), and C8-C6,2:$PC_{61}BM$ (1:1) blends in thin films (arrows indicating (010) peaks). c) Absorption spectra of C8-C8: $PC_{61}BM$ (1:1), C8-C12:$PC_{61}BM$ (1:1), and C8-C6,2:$PC_{61}BM$ (1:1) blends in thin films. d) Current density vs. voltage characteristics in the dark (inset) and illumination under 1 sun, AM1.5 conditions for C8-C8, C8-C12, and C8-C6,2 polymers based BHJ solar cells.

The UV-Vis absorption spectra and current-voltage characteristics of these three polymers are plotted in Fig. 2.7c and d, respectively. According to equation (2.4), the short straight chains of C8 on both NDT and DTBT units should improve the J_{sc} due to a large J_{so}. However, the BHJ device of the C8-C8 polymer with the largest J_{so} does not exhibit a high J_{sc}, largely due to the poor film morphology as large polymer domains and rougher surfaces have been observed (Fig. 2.8). The very strong intermolecular interaction in the C8-C8 polymer limits its solubility in the processing solvent, resulting

in large agglomerations in the film. These undesired large aggregates of polymers influence the J_{sc} by limiting the exciton diffusion to the interface with $PC_{61}BM$, as well as by impacting the energetics and kinetics of charge transfer at the interface. The strong tendency to aggregate of the C8-C8 polymer is also indicated by the relatively low absorption coefficient and a red-shift absorption shoulder arising at 730 nm due to the strong stacking of polymers (Fig. 2.7c).
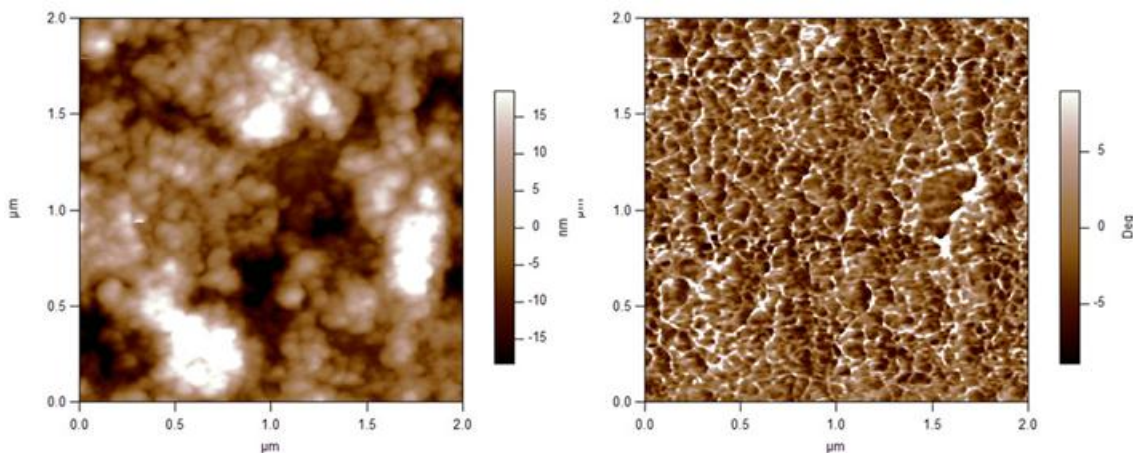
Figure 2.8. AFM images of C8-C8:$PC_{61}BM$ film in a 1:1 ratio blend. (left: height image; right: phase image).

Changing the short straight C8 chain on the DTBT unit to a long straight chain of C12 or a branched chain of C6,2 significantly improves the solubility of the resulting polymers (C8-C12 and C8-C6,2) and the morphology of their blend with $PC_{61}BM$. The improved solubility of the C8-C12 polymer compared with that of the C8-C8 is due to the increased degrees of freedom resulted from the four extra carbon atoms on the C12 chain compared with the C8 chain. The longer side chain of C12 slightly weakens the intermolecular interaction in the C8-C12 polymer, thereby leading to a slightly smaller J_{so}. This smaller J_{so} helps enhance V_{oc} from 0.41 V in BHJ solar cells of the C8-C8 polymer to 0.52 V in the case of the C8-C12 polymer. Similarly, the improved solubility of the

C8-C6,2 polymer can be explained by the weakened intermolecular packing due to the branched chain of C6,2, which also accounts for a much smaller J_{so} of the C8-C6,2 polymer than that of the C8-C8. This smaller J_{so} explains the observed higher V_{oc} of 0.59 V in solar cells made from the C8-C6,2 polymer. It is interesting to notice that the observed J_{sc} of C8-C6,2 polymer BHJ devices is much higher than that of C8-C12, even though the latter polymer has a four times larger J_{so} as that of the former polymer. This observation implies that J_{sc} is not only influenced by the J_{so}. Another important parameter that determines the J_{sc} is the density of the conjugated backbones in thin films, which is controlled by the length of alkyl side chain. As indicated in the previous discussion, the longer side chains of C12 in the C8-C12 polymer increase the distance between PNDT-DTBT polymer backbones (~ 3.5 Å larger value of the (100) spacing in the C8-C12 polymer than that in the C8-C6,2) and result in a lower polymer backbone density at given thin films. Therefore, the C8-C12 polymer with a smaller polymer backbone density has a lower absorption coefficient than that of the C8-C6,2 (Fig. 2.7c) and consequently a decreased J_{sc}. Similarly, the C10,6-C8 polymer exhibits a higher J_{so} but a smaller J_{sc}, partly due to the lower absorption coefficient of the C10,6-C8 polymer (due to the longer side chain of C10,6).

2.7. DTBT with 2-ethylhexyl (C6,2) and NDT with Different Alkyl Chains

To complement the previous investigations where we arbitrarily defined the alkyl chain on the NDT unit while changing the chain on the DTBT unit, in section 2.7, the short branched alkyl chain of C6,2 is fixed on the DTBT unit, while the alkyl chain on the

NDT unit is varied by the size and branching. Here, polymers C10,6-C6,2, C8-C6,2, and C6,2-C6,2 were investigated.

As shown in Table 2.4, the C10,6-C6,2 polymer has noticeably larger (010) spacing and weaker peak intensity than that of either C8-C6,2 or C6,2-C6,2, due to the co-existence of both the big and bulky branched chains of C10,6 and the branched chains of C6,2. The weak intermolecular interaction in the C10,6-C6,2 polymer explains its small J_{so} (smallest among all six polymers studied), which consequently leads to the highest observed V_{oc} (0.81 V) as a BHJ device. Compared with the C8-C6,2 polymer, the C6,2-C6,2 polymer with branched chains, C6,2 on the NDT unit, exhibits a weaker (010) peak and a slightly larger (010) spacing. Hence, a relatively smaller J_{so} is obtained for the C6,2-C6,2 polymer, which contributes to the observed larger V_{oc} (0.69 V) as a BHJ device than that of the C8-C6,2 polymer (0.59 V).

On the other hand, the largest J_{so} of the C8-C6,2 polymer (among all three polymers in section 2.7) implies the strongest intermolecular interaction, which is supported by the smallest (010) spacing and strongest peak intensity. This strong intermolecular stacking explains the observed smallest optical band gap. Moreover, having two shorter chains (C8 and C6,2) helps maintain a relatively high absorption coefficient of the C8-C6,2 polymer (Fig. 2.9c). Both of the large J_{so} and high absorption coefficient result in the highest J_{sc} (10.93 mA/cm^2) of the C8-C6,2 polymer based BHJ devices among all studied six polymers.

Finally, the C6,2-6,2 polymer exhibits only a slightly smaller J_{sc} (10.67 mA/cm^2) in its BHJ device than that of the C8-C6,2 polymer (Table 2.3), but a significant larger V_{oc}

(0.69 V vs. 0.59 V). Therefore the C6,2-C6,2 polymer demonstrates the highest efficiency (3.36%) among all studied six polymers. It does appear that shorter, branched chains strike a balance between the V_{oc} and the J_{sc}, resulting in the highest possible efficiency.
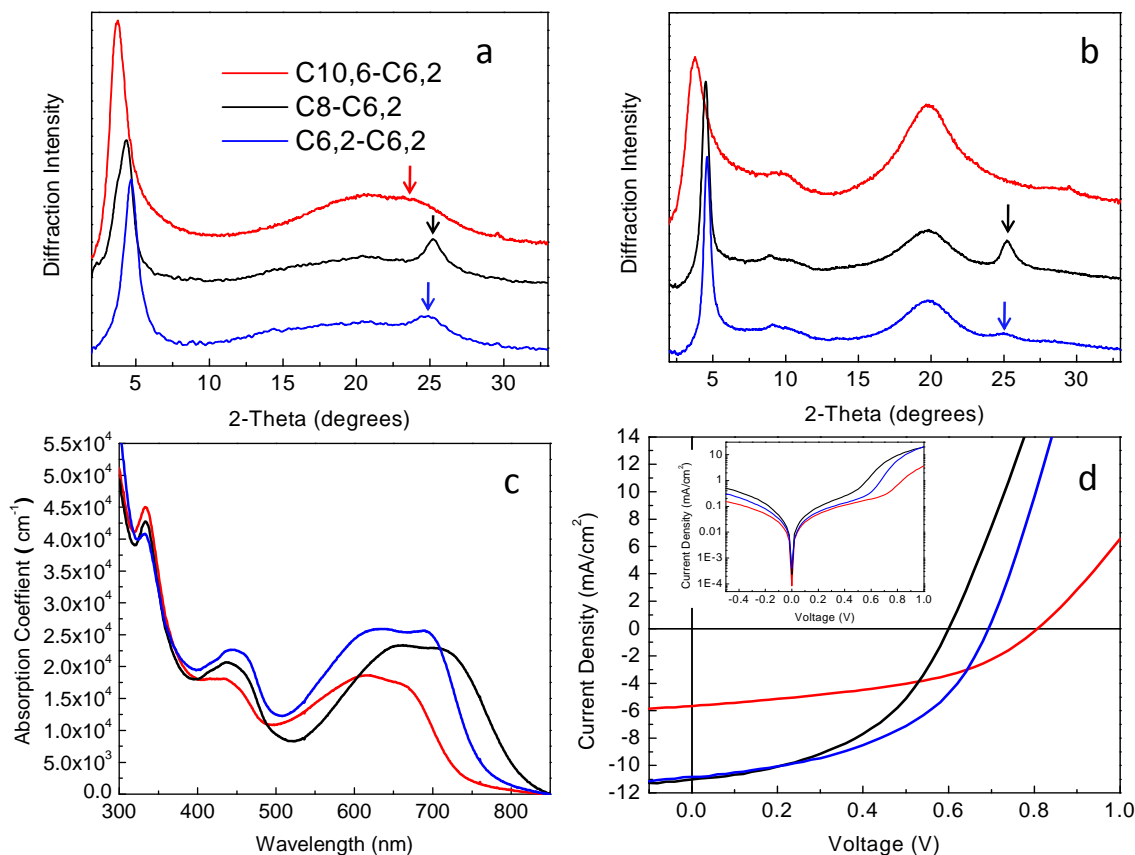
Figure 2.9. a) XRD spectra of the C10,6-C6,2, C8-C6,2, and C6,2-C6,2 polymers in thin films (arrows indicating (010) peaks). b) XRD spectra of C10,6-C6,2:PC$_{61}$BM (1:1), C8-C6,2:PC$_{61}$BM (1:1), and C6,2-C6,2:PC$_{61}$BM (1:1) blends in thin films (arrows indicating (010) peaks). c) Absorption spectra of C10,6-C6,2:PC$_{61}$BM (1:1), C8-C6,2:PC$_{61}$BM (1:1), and C6,2-C6,2:PC$_{61}$BM (1:1) blends in thin films. d) Current density vs. voltage characteristics in the dark (inset) and illumination under 1 sun, AM1.5 conditions for C10,6-C6,2, C8-C6,2, and C6,2-C6,2 polymers based BHJ solar cells.

2.8. Conclusion

The most striking conclusion of this study is that the side chains attached to the conjugated backbone of a low band gap polymer (PNDT-DTBT) significantly impacts the photovoltaic characteristics (V_{oc} and J_{sc}) of the corresponding BHJ solar cell. Further, we successfully established a quantitative relationship between the attached alkyl side chains and observed photovoltaic properties via the generalized Shockley equation. J_{so} – a parameter that is determined by the intrinsic properties of donor polymers – is distilled to quantify the observed side chains-dependent photovoltaic properties. Since our library of six polymers shares an identical conjugated backbone (PNDT-DTBT), the variation of the J_{so} on the different side chains is believed to be representing the strength of the intermolecular interaction among polymers in thin films.

As demonstrated in our study, long and branched side chains would weaken the intermolecular interaction, leading to a small J_{so} which is beneficial to the V_{oc}. On the other hand, short and straight side chains would promote the intermolecular interaction, rendering a large J_{so}, which should increase the J_{sc} (though at the expense of V_{oc}). However, J_{sc} is not only influenced by J_{so} but also affected by the film morphology of the blend, and the density of the conjugated backbone which is controlled by the length of alkyl side chain. It appears that short and branched side chains would strike a desirable balance between V_{oc} and J_{sc}, to reach the optimum efficiency via an appropriate J_{so}. This hypothesis is supported by the fact that the highest efficiency of 3.36% is obtained from the C6,2-C6,2 polymer in the studied six polymers, with a V_{oc} of 0.69 V and a J_{sc} of 10.67 mA/cm^2 [107]. Similar results have been obtained in other studies[21,106], though the authors ascribed the observed difference in photovoltaic properties to the morphological

42

difference in the BHJ blend. Based on our study, it might not be coincidental or serendipitous that the branched side chain of C6,2 has been used in a number of low band gap polymer with impressive photovoltaic efficiencies in their BHJ solar cells[12,94,108,109].

Finally, we want to mention that though the short, branched chain of C6,2 seems to be the optimum side chain for the studied PNDT-DTBT as well as other polymer systems; however, it may not be the ideal chain for any given conjugated backbone. The structural optimization of polymers to reach the full potential of any given conjugated polymer for photovoltaic applications is a convoluted process. Other factors, such as molecular weight, solubility in the processing solvent, and the morphology of the polymer/$PC_{61}BM$ blend, remain to be included in the selection of side chains.

CHAPTER 3

DISENTANGLING THE IMPACT OF SIDE CHAINS AND FLUORINE SUBSTITUENTS OF CONJUGATED DONOR POLYMERS ON THE PERFORMANCE OF PHOTOVOLTAIC BLENDS

3.1. Introduction

Any conjugated polymer for photovoltaic applications contains three key constituting components: the conjugated backbone, the side chains and the substituents (both on the conjugated backbone).[9] While the creative design and synthesis of conjugated backbones has received the greatest amount of attention and has driven the efficiency of BHJ solar cells to record highs,[12,21,23,26,28-30,110-112] the side chains and the substituents have largely been overlooked until recently.[12,28,30,35,37,106-108,113-115]

Conjugated polymers require side chains to ensure their solubility in the processing solvent prior to the device fabrication. Further, these side chains are critical to achieving high polymer molecular weight which improves charge transport in the related BHJ solar cells and leads to higher currents.[35] However, recently people[12,37,106,107,113] have shown that in addition to addressing the concerns on the solubility and the molecular weight of related polymers, these seemingly "trivial" side chains can significantly affect the device characteristics of related BHJ solar cells (e.g., V_{oc}, J_{sc}, and FF).[38,118,123,129,130] These chains influence the intermolecular interaction (among polymers and between polymers and fullerenes) and related stacking/packing *in the solid state*, all of which have a large impact on the performance of the BHJ solar cell, a solid state device. Specifically, in

Chapter 2, we showed that long branched side chains weaken intermolecular interactions, leading to an increased V_{oc} but a lower J_{sc}.[114] On the other hand, short straight side chains promote intermolecular interaction, rendering an enhanced J_{sc} (though at the expense of V_{oc}). Therefore, we concluded that side chain optimization of conjugated polymers requires a balance between V_{oc} and J_{sc} to reach optimum efficiencies, since achieving both a high V_{oc} and a high J_{sc} seemed irreconcilable.

While side chains do not significantly perturb the electronic and optical properties of related conjugated polymers (if anchored properly to minimize steric hindrance), substituents on the backbone such as fluorine (F) and oxygen (O), can fine-tune properties including the energy levels and band gaps.[106,108] For example, we recently showed that for two separate polymers, adding F atoms to the conjugated backbone leads to a higher V_{oc}, a higher J_{sc} and a better *FF* for F-substituted polymer-based solar cells than those of their non-fluorinated analogs.[28,30] Interestingly, in both cases, even with long and bulky side chains attached to the conjugated backbones (which would have led to a lower J_{sc}), very respectable currents were still obtained together with high V_{oc} as well as better *FF*. These observations imply that F substituents could mitigate the negative impact on J_{sc} due to long and branched side chains – a very interesting observation that warrants further investigation.

C6,2-C6,2 X = H R$_1$ = 2-ethylhexyl R$_2$ = 2-ethylhexyl
C8,4-C6,2 X = H R$_1$ = 2-butyloctyl R$_2$ = 2-ethylhexyl
C6,2-C6,2F X = **F** R$_1$ = 2-ethylhexyl R$_2$ = 2-ethylhexyl
C8,4-C6,2F X = **F** R$_1$ = 2-butyloctyl R$_2$ = 2-ethylhexyl
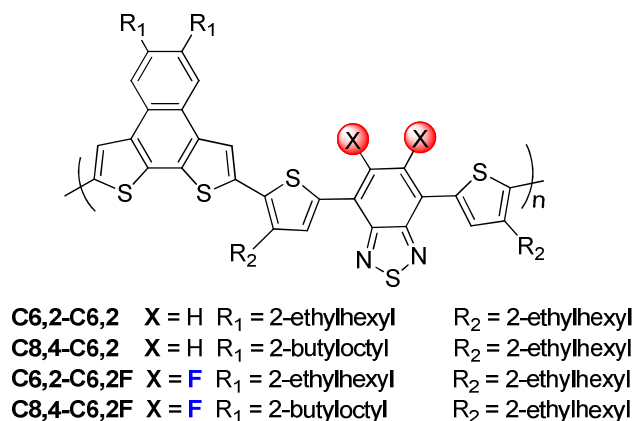
Figure 3.1. The chemical structures of four polymers based on the PNDT-DTBT backbone.

In order to disentangle the intertwined influence on photovoltaic performance of side chains and F substituents, we carried out a systematic study on a series of polymers containing identical conjugated backbones (PNDT-DTBT, the same backbone in Chapter 2) but different side chains and either hydrogen or F substituents (Fig. 3.1). To minimize possible interference from molecular weight variations, all four polymers were synthesized with similar molecular weight as shown in Table 3.1. Interestingly, polymer C8,4-C6,2F with long bulky side chains and F substituents exhibits the largest V_{oc} *and* a very high J_{sc} as well as a high *FF*, resulting in the highest efficiency observed among all four polymers, regardless of processing solvent choice (chlorobenzene or dichlorobenzene). The observed differences in V_{oc}, J_{sc} and *FF*, depending upon the side chains and F substituents, were thoroughly investigated via device characterization and optimization, modeling and calculations, and X-ray scattering. Our study clearly indicates that a proper combination of side chains and F substituents on the conjugated backbone is a viable approach to *simultaneously* obtain large V_{oc}, high J_{sc} and good *FF* of the related BHJ devices.

3.2. Experimental Section

3.2.1 Grazing-Incidence Wide-Angle X-ray Scattering (GI-WAXS)

Samples for GI-WAXS were prepared on PEDOT:PSS-coated Si substrates using the same preparation conditions as devices. Measurements were taken at beamline 7.3.3 of the Advanced Light Source using a Pilatus 1M detector. A grazing incident angle of 0.12º was used where air scatter was minimized by purging the air between the x-ray source, sample, and detector with helium gas.

3.2.2. Polymer Solar Cell Fabrication and Testing

Glass substrates coated with patterned indium-doped tin oxide (ITO) were purchased from Thin Film Devices, Inc. The 150 nm sputtered ITO pattern had a resistivity of $15\Omega/\square$. Prior to use, the substrates were ultrasonicated for 20 minutes in acetone followed by deionized water and then 2-propanol. The substrates were dried under a stream of nitrogen and subjected to the treatment of UV-Ozone over 30 minutes. A filtered dispersion of PEDOT:PSS in water (Baytron PH500) was then spun cast onto clean ITO substrates at 4000 rpm for 60 seconds and then baked at 140 °C for 10 minutes to give a thin film with a thickness of 40 nm. Blends of polymer and $PC_{61}BM$ (1:1 w/w, 10 mg/mL for polymers) were dissolved in DCB with heating at 130 °C or in CB with heating at 100 °C for 6 hours. All the solutions were spun cast at optimized rpm for 60 seconds onto PEDOT:PSS layer. The substrates were then dried at room temperature in the glovebox under nitrogen atmosphere for 12 hours. The devices were finished for measurement after thermal deposition of a 30 nm film of calcium and a 70 nm aluminum film as the cathode at a pressure of $\sim 2\times10^{-6}$ mbar. There are 8 devices per substrate, with an active area of 12 mm^2 per device. Device characterization was carried out under AM

1.5G irradiation with the intensity of 100 mW/cm^2 (Oriel 91160, 300 W) calibrated by a NREL certified standard silicon cell. Current versus potential (I-V) curves were recorded with a Keithley 2400 digital source meter. EQE were detected under monochromatic illumination (Oriel Cornerstone 260 ¼ m monochromator equipped with Oriel 70613NS QTH lamp) and the calibration of the incident light was performed with a monocrystalline silicon diode. All fabrication steps after adding the PEDOT:PSS layer onto ITO substrate, and characterizations were performed in gloveboxes under nitrogen atmosphere. For more experimental details about reagents, instrumentation, electrochemistry, and spectroscopy please check **Appendix A**.

3.3. Optical and electrochemical properties

At high temperature and in a good solvent, such as dichlorobenzene, the effect of solubilizing chains on conjugated polymers has little impact on the optical properties since the polymers are adequately solvated. Thus the absorption spectra of polymers with identical backbones collapse together, regardless of the side chain size and shape, as shown in Fig. 3.2a. Compared with those of non-fluorinated polymers, the band edges of these F substituted polymers are slightly (~0.03 eV) blue-shifted (1.93 eV vs. 1.90 eV), as observed in other similar systems.[9,28,106].
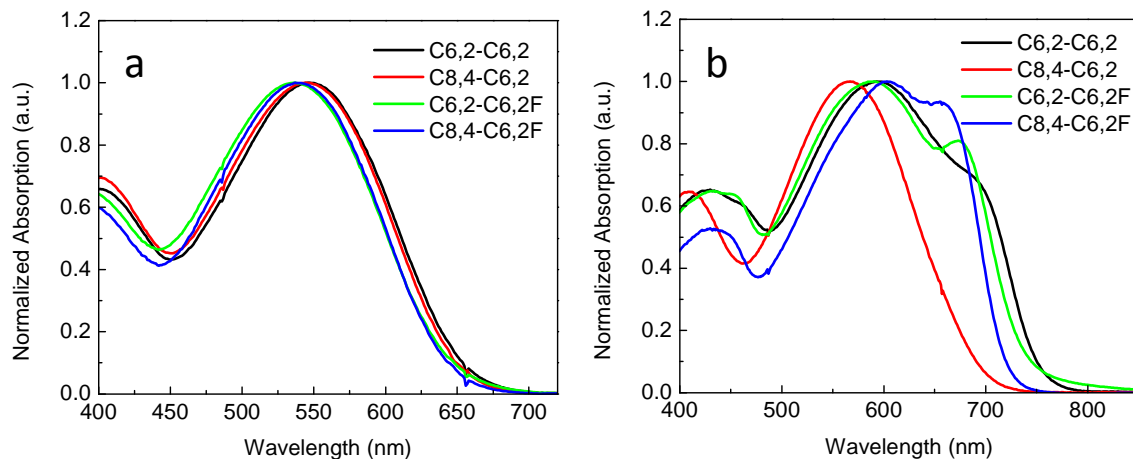
Figure 3.2. Normalized absorption spectra of four polymers in dichlorobenzene at a) 140 ºC and b) room temperature.

However, when these polymer solutions of identical concentration are cooled to room temperature, we observe noticeable differences in the optical properties of these polymer solutions (Fig. 3.2b). For example, polymer C6,2-C6,2 with short side chains exhibits much stronger aggregation when compared with C8,4-C6,2, as indicated by a pronounced absorption increase at longer wavelengths from about 690 nm to almost 750 nm. This red-shift in the absorption spectrum of C6,2-C6,2 leads to a narrow band gap of 1.65 eV, roughly 0.14 eV smaller than that of C8,4-C6,2 (1.79 eV). These results are consistent with our previous observation that introducing short side chains to the polymer backbone renders a shorter π-π overlapping distance, and strengthens π-π stacking ability of the relevant conjugated polymers.[114] On the other hand, when F substituents are added to these two polymers, both C6,2-C6,2F and C8,4-C6,2F show pronounced absorption shoulders around 655 and 672 nm, respectively, indicating strong polymer aggregation even in solution at room temperature. Strong aggregation in these fluorinated PNDT-DTBTs is likely due to the induced inter- and intramolecular interactions via C-F···H, F···F and C-F···π_F interactions.[41,116] Because of the strong stacking introduced by F substituents, polymer C8,4-C6,2F demonstrates a red shift in its absorption spectrum

when compared with that of C8,4-C6,2, leading to a smaller band gap of 1.72 eV. Finally, introducing F atoms to C6,2-C6,2 does not further decrease its band gap, as observed from the similar absorption edge of C6,2-C6,2F to that of C6,2-C6,2. It seems that the short side chains on C6,2-C6,2 already introduced such a strong π-π stacking that additional π-π stacking offered by F substituents cannot further enhance the absorption but only renders a poorer solubility of C6,2-C6,2F.

Table 3.1. Key polymer properties of four polymers

Polymer	M_n (g/mol)	M_w (g/mol)	PDI	$E_g{}^a$ (eV)		HOMO (eV)
				140°C	R.T.	
C6,2-C6,2	7,879	18,525	2.35	1.90	1.65	– 5.36
C8,4-C6,2	7,618	16,244	2.13	1.90	1.79	– 5.37
C6,2-C6,2F	7,449	18,829	2.53	1.93	1.68	– 5.41
C8,4-C6,2F	10,478	28,320	2.70	1.93	1.72	– 5.43

[a] Calculated from the intersection of the tangents on the low energetic edge of the absorption spectrum (in dichlorobenzene) with the baseline.

3.4. Morphology of Polymer:PC$_{61}$BM Thin Films

As shown in Fig. 3.3, with the strong π-π stacking ability offered by short C6,2 side chains, the BHJ film of C6,2-C6,2 polymer/PC$_{61}$BM exhibits clear phase separation with uniform separated domains as observed in the atomic-force microscopy (AFM) phase image (Fig. 3.3a), whereas a finer, less pronounced phase separation was observed in the blend film of C8,4-C6,2 polymer/PC$_{61}$BM (Fig. 3.3b). On the other hand, compared with the non-fluorinated polymers, both BHJ films with the fluorinated polymers exhibit very large separated domains (Fig. 3.3c,d), indicative of enhanced inter- and intramolecular interactions via C-F···H, F···F and C-F···π$_F$ interactions.[41,116]
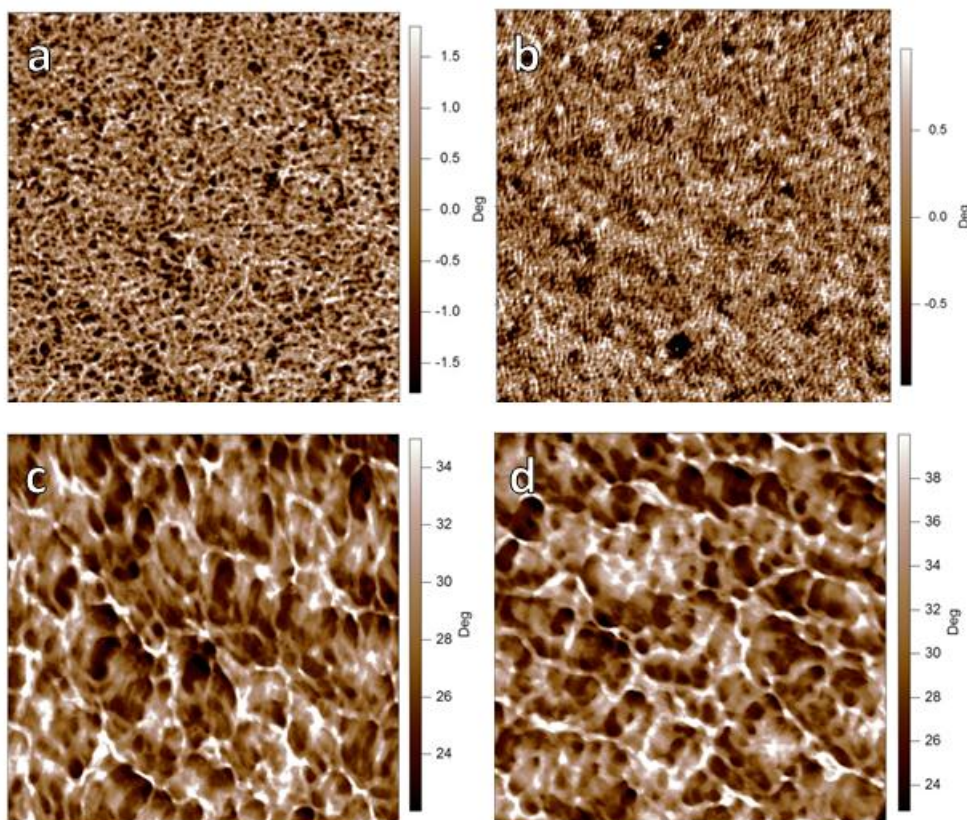
Figure 3.3. AFM phase images (2×2 μm) of a) C6,2-C6,2, b) C8,4-C6,2, c) C6,2-C6,2F and d) C8,4-C6,2F-based BHJ devices processed with dichlorobenzene.

Grazing-incidence wide-angle X-ray scattering (GI-WAXS) was also conducted to gain further insight into the structural differences of the blend films. This measurement provides detailed information on the relative degree of crystallization along with relative crystallite orientation and a minimum crystallite size. It can also provide a relative measure of the strengths of intermolecular interaction of molecules as reflected in changes in the crystal d-spacing.[113,114] Fig. 3.4 presents 2D GI-WAXS data of these four polymer/$PC_{61}BM$ films measured on PEDOT:PSS-coated Si substrates. Representative d-spacing values and peak intensities are listed in Table 3.2, corresponding to multi-peak fitting in **Appendix B Fig. B.2**. It should be noted that the isotropic and broad ring

around q=1.4 $\mathring{A}^{-1}$ arises from amorphous $PC_{61}BM$. In terms of polymer crystallites, the strong (100) peak and higher order peaks visible for some films represent lamellar polymer spacing between backbones. On the other hand, the π-π stacking between coplanar π-conjugated polymers is represented by the (010) peak. Polymers with short C6,2 side chains (C6,2-C6,2 and C6,2-C6,2F) exhibit both smaller (100) and (010) spacing than their corresponding polymers with C8,4 side chains. The shorter (100) spacing by ~1 $\mathring{A}$ for the C6,2-based polymer blends is consistent with the shorter C6,2 side chains when compared with the blends with C8,4-based polymers. This same argument could be used to explain the slight reductions in (010) spacing for C6,2-based polymer blends where these side chains require less space next to the polymer backbone. This would indicate stronger intermolecular interactions between polymer chains as argued previously to influence device performance.[114]
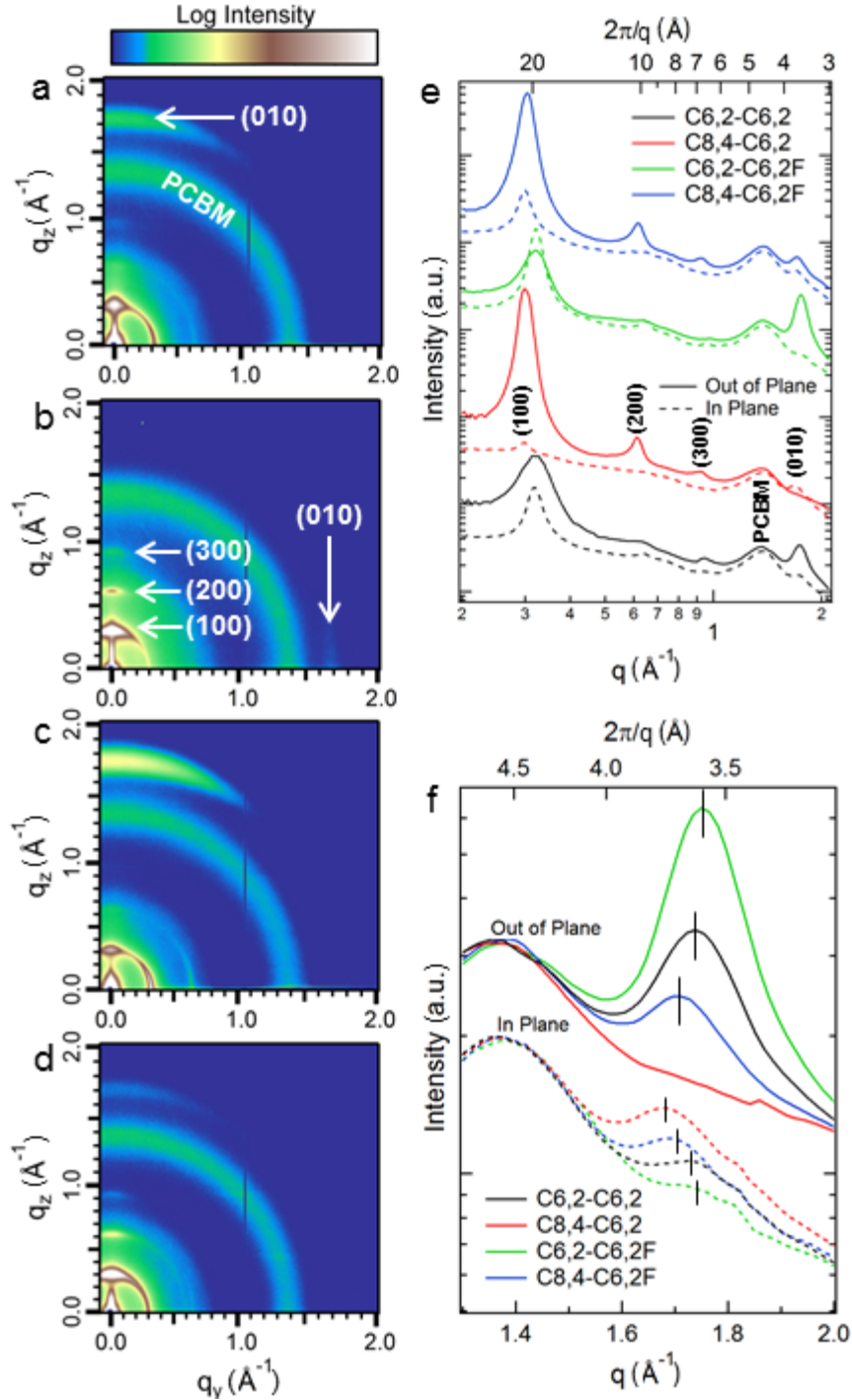
Figure 3.4. GI-WAXS data of a) C6,2-C6,2, b) C8,4-C6,2, c) C6,2-C6,2F and d) C8,4-C6,2F-based polymer:PC$_{61}$BM BHJ films processed with dichlorobenzene. e) The corresponding sector averages in plane (q$_y$) and out of plane (q$_z$) along with f) a zoom-in comparison of the (010) peaks.

In terms of relative degrees of polymer crystallinity and orientation, introducing shorter side chains to the polymer backbone increases the scattering intensity of the (010) peak in the out-of-plane (OOP) direction compared to the analogous polymer blends with C8,4 side chains. Similar to the influence of shortening the side chains, introducing F to the polymer backbones also increases the OOP (010) peak intensities (Fig. 3.4e,f). By comparing intensity ratios of OOP to in-plane (IP) in the 010 direction, relative comparisons of the orientation of π-π stacking planes can also be made. With addition of fluorine or when shortening the side chains, the polymer orientation becomes increasingly "face-on" with the π-π stacking direction perpendicular to the substrate. This can also be noted in the intensity distribution of the (100) peaks for the IP and OOP directions where the (100) and (200) peaks have larger IP components for polymers that are more "face-on". From the ratio of (010) intensities, blends with C6,2-C6,2F exhibit the most "face-on" polymer configuration while those with C8,4-C6,2 exhibit the least and are preferentially "edge-on" with the side chains perpendicular to the substrate. This is also evident in that this blend has the highest IP (010) intensity and largest anisotropy between IP and OOP (100) intensity. Interestingly, shortening (010) polymer d-spacing via shortening the side chain and/or adding F substituents promotes increasing "face-on" polymer orientations. It is possible that strong π-π stacking ability helps the coplanar π-conjugated backbone interact strongly with the substrate, thereby facilitating a "face-on" structure. Finally, compared to polymer orientation, less significant changes occur for the polymer crystallite size calculated from the inverse full width at half maximum of the (010) peak width (see **Appendix B Fig. B.2**).

Table 3.2. Representative GIWAXS results of four polymer/PC$_{61}$BM blends

Polymer	(100) d-spacing $(\mathring{A})$	(010) d-spacing $(\mathring{A})$	(010) OOP Intensity	(010) IP Intensity	(010) OOP/IP Intensity Ratio
C6,2-C6,2	19.6	3.60	145	25	5.8
C8,4-C6,2	21.0	3.72	<5	40	<0.13
C6,2-C6,2F	19.6	3.57	401	13	31
C8,4-C6,2F	20.8	3.66	49	25	2.0

3.5. Photovoltaic Properties of BHJ Devices Processed with *o*-Dichlorobenzene (DCB)
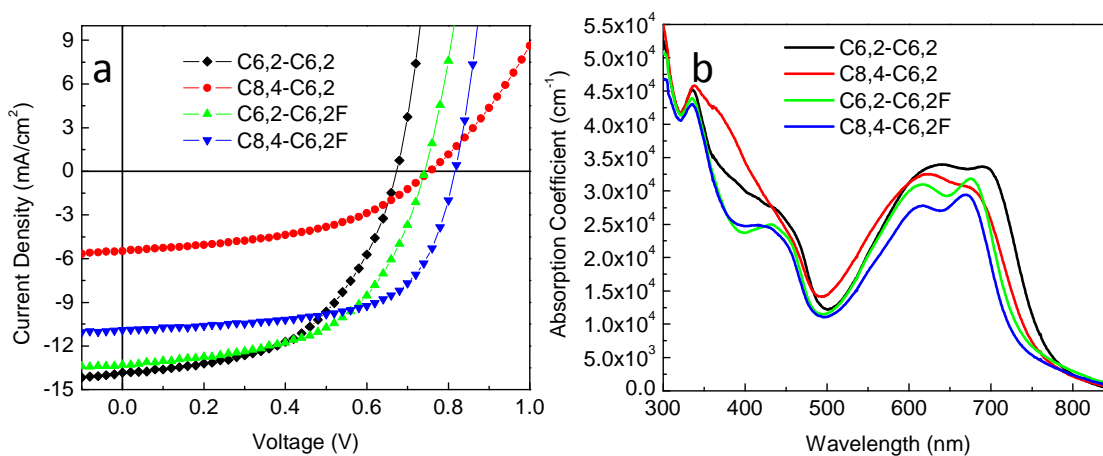
Figure 3.5. a) Light current density vs. voltage characteristics of optimized BHJ solar cells processed in dichlorobenzene under 1 Sun condition (100 mW/cm^2). b) Absorption coefficient of polymer/PC$_{61}$BM thin films processed in dichlorobenzene.

Quite surprisingly, the marginal changes in polymer structure that led to minor changes in the optical and electrochemical properties resulted in significant changes in the morphological properties, as we discussed in the previous section. Correspondingly, significant differences were noted in the photovoltaic properties of BHJ devices where the efficiency varies as much as three fold (from 1.91% to 5.62%, Table 3.3). The current-voltage characteristics of solar cells based on these four polymers are shown in Fig. 3.5a with representative performance parameters listed in Table 3.3. Please note that

for fair comparison and accurate interpretation of structure-property relationships, we maintained identical processing conditions for all polymers for their representative devices (e.g., weight ratio of polymer to $PC_{61}BM$ was 1:1 in DCB). The high boiling solvent (DCB) extends the solvent annealing time compared to chlorobenzene, which allows more time for polymer chains to organize into their natural morphology dominated by the intermolecular interactions among polymers.

Table 3.3. Photovoltaic performances of optimized devices processed in dichlorobenzene.

Polymer	Polymer: $PC_{61}BM$	Processing Solvent	Thickness (nm)	V_{oc} (V)	J_{sc} (mA/cm^2)	FF (%)	η (%)
C6,2-C6,2	1:1	DCB	85	0.67	13.82	53.09	4.92
C8,4-C6,2	1:1	DCB	83	0.75	5.47	46.54	1.91
C6,2-C6,2F	1:1	DCB	116	0.75	13.29	54.38	5.42
C8,4-C6,2F	1:1	DCB	118	0.81	10.91	63.64	5.62

Detailed analysis of the BHJ device characteristics further discloses the impact on related photovoltaic properties introduced by the subtle change in alkyl chains and substituents on these polymers. Since the efficiency of all solar cells is determined by the

equation: $\eta = \dfrac{J_{sc} \times V_{oc} \times FF}{P_{input}}$, where η and P_{input} are the cell's energy conversion efficiency and input power, respectively; in the following, we will individually discuss the impact of F substituents and side chains on V_{oc}, J_{sc} and FF of related BHJ devices based on these four polymers.

3.5.1 Open Circuit Voltage (V_{oc})

Derived from the Shockley equation, V_{oc} can be described by[98,114]

$$V_{OC} \approx \frac{nkT}{q} \ln\left(\frac{J_{SC}}{J_{SO}}\right) + \frac{\Delta E_{DA}}{2q}$$

(3.1)

Where, q is the fundamental charge, n is the diode ideality factor, ΔE_{DA} is the energy difference between the LUMO level of the Acceptor (A) and the HOMO level of the Donor (D), and the pre-exponential term, J_{so}, depending on a number of materials properties that affect the generation and recombination of free carriers. Previous studies successfully demonstrated a direct relationship between the strength of intermolecular interactions in the polymer/$PC_{61}BM$ blends and the magnitude of J_{so}.[98,114] The calculated values of the V_{oc}[98,114] match the corresponding experimental data exceptionally well (Table 3.4), demonstrating a clear validation of this calculation for V_{oc}. For the non-fluorinated polymers with only variation of the side chains (i.e., C8,4-C6,2 vs. C6,2-C6,2), we observe higher V_{oc} for the polymer with C8,4 side chains than that of the corresponding polymer with C6,2 side chains. As discussed previously, different side chains barely change the HOMO level of donor polymers and hence lead to very similar ΔE_{DA} between C6,2-C6,2 and C8,4-C6,2 polymers. Therefore, the increased V_{oc} of devices based on the polymer with longer side chains of C8,4 is attributed to a smaller J_{so}, according to equation (3.1). This is because the long bulky C8,4 side chains require large space volumes next to the polymer backbone and hence reduce the intermolecular interaction between polymer chains in polymer crystallites (as indicated by GI-WAXS above) and potentially between polymer/$PC_{61}BM$, leading to a small J_{so}.[114]

Table 3.4. Calculated photovoltaic performances of four polymers in their BHJ devices

Polymer	Solvent	J_{so} (mA/cm^2)	n	$\frac{nkT}{q} ln\left(\frac{J_{SC}}{J_{SO}}\right)$	$\frac{\Delta E_{DA}}{2q}$	V_{oc} (V) Cal	V_{oc} (V) Measured
C6,2-C6,2	DCB	9.64	3.88	0.036	0.630	0.666	0.67
C8,4-C6,2	DCB	1.36	3.84	0.138	0.635	0.773	0.75
C6,2-C6,2F	DCB	3.25	3.09	0.113	0.655	0.768	0.75
C8,4-C6,2F	DCB	1.06	2.52	0.152	0.665	0.817	0.81

On the other hand, adding F substituents to the PNDT-DTBT backbone leads to a noticeably higher V_{oc} of its related BHJ device than that of its non-fluorinated analog-based BHJ cell, even with identical side chains (i.e., C6,2-C6,2F vs. C6,2-C6,2), which can be explained according to equation (3.1). First, the electron-withdrawing nature of the F substituents lowers the HOMO energy level of the fluorinated polymer by ~ 0.05 eV relative to that of the non-fluorinated analog, resulting in a larger ΔE_{DA} for the fluorinated polymer. Second, the fluorinated polymer exhibits a smaller J_{so} value than that of the non-fluorinated analog, leading to a larger value in the first term of equation (3.1) (Table 3.4). A smaller J_{so} implies weakened polymer/PC$_{61}$BM interactions in the blend of C6,2-C6,2F polymer and PC$_{61}$BM, which seemingly contradicts the enhanced polymer/polymer intermolecular interaction in the C6,2-C6,2F polymer/PC$_{61}$BM blend as we discussed earlier (Fig. 3.4, Section 3.4). We offer the following explanation. The impact on J_{so} by the alkyl chain is different from that exerted by the F substitution. While these bulky side chains distance the conjugated polymer from PC$_{61}$BM, thereby weakening the interaction between the polymer and PC$_{61}$BM and thus a small J_{so}, we believe the smaller J_{so} obtained with these fluorinated polymers can be attributed to the suppressed recombination rate at D/A interfaces via introducing these electronegative F

substituents. A detailed discussion will be provided in Section 3.5.3. Combining a low HOMO energy level and a small J_{so}, the fluorinated polymer C6,2-C6,2F exhibits significantly larger V_{oc} in its BHJ device than that in the non-fluorinated C6,2-C6,2-based BHJ device.

Based on the above discussion, the synergistic effects of incorporating both long bulky side chains and F substituents in the case of polymer C8,4-C6,2F should lead to the largest V_{oc} in its BHJ device in this series of polymers, which is indeed what we observed (0.81 V for the C8,4-C6,2F-based BHJ device).

3.5.2 Short Circuit Current Density (J_{sc})

Similar to what we observed before,[114] replacing the long bulky side chain with short side chain results in a significant increase of J_{sc} from 5.47 mA/cm^2 in the case of the C8,4-C6,2 polymer to 13.82 mA/cm^2 in the C6,2-C6,2 polymer. The higher J_{sc} from the polymer of shorter chains can be ascribed to a) higher optical absorption, b) improved generation of free charge carriers, and c) potentially improved charge extraction due to favorable π-π stacking and favorable average backbone orientation along the sample normal as derived from the GI-WAXS and UV-Vis spectra, respectively. As indicated in the previous discussion, the value of (100) spacing corresponds to the distance between polymer lamellas, which is determined by the longest alkyl side chain. Thus, the C6,2-C6,2 polymer with a smaller value of (100) spacing has a larger density of polymer backbone and consequently a higher absorption coefficient (Fig. 3.5b). Furthermore, the short side chains of C6,2 occupy less space than the long bulky side chains of C8,4, resulting in stronger π-π stacking of coplanar conjugated backbones for the C6,2-C6,2 polymer than that for C8,4-C6,2. This stronger π-π stacking explains the smaller optical

band gaps in the C6,2-C6,2 polymer thin film (Fig. 3.5b). Both a high absorption coefficient and a smaller band gap should lead to an improved J_{sc}. Also related to the strong stacking ability offered by these short chains, C6,2-C6,2 crystallites in BHJ film exhibit more "face on" structure compared with the "edge on" structure obtained in the blend film of C8,4-C6,2 polymer/PC$_{61}$BM (Fig. 3.4, Section 3.4). This desirable orientation of polymer crystallites in the case of C6,2-C6,2 polymer/PC$_{61}$BM blend could provide more efficient hole charge transport and improved charge collection efficiency.[117-120] Similar analyses can be applied to explain the observed similar trend for both fluorinated polymers: the BHJ device based on C6,2-C6,2F with short side chains exhibits a higher J_{sc} (13.29 mA/cm^2) than that of C8,4-C6,2F-based device (10.91 mA/cm^2).

The absorption coefficients from Fig. 3.5b are used to calcluate the imaginary part of the index of refraction, k, from k = α·λ/4π, where α is the absorption coefficient and λ is the incident wavelength. The real part of the index of refraction for all wavelengths is then assumed to be 2.0, which has been shown to not significantly influence the overall absorption compared to using the true index dispersion.[121] Using the transfer matrix optical model, absorption in the active layer is then simulated using variable active layer thickness and the following device architecture: glass/ITO (150 nm)/PEDOT:PSS (40 nm)/active layer/aluminum. The optical properties of glass, ITO, PEDOT:PSS, and aluminum were measured using spectroscopic ellipsometry and are given elsewhere[122] where the model accounts for parasitic absorption losses by the electrodes and optical interference due to each device interface. Absorption in the active layer is then convoluted with the standard 1 Sun solar spectrum and integrated between 350 and 875

nm to give a maximum achievable photocurrent assuming 100% internal quantum efficiency. These values are then normalized to the first peak of the C6,2-C6,2 polymer blend as shown below to compare how active layer thickness and differences in intrinsic absorption by each blend would affect the measured photocurrent, especially the short-circuit current.
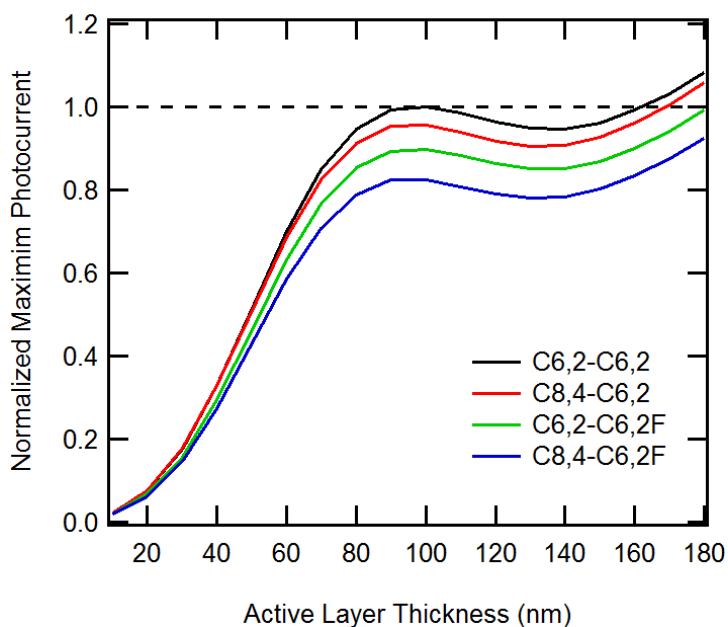
Figure 3.6. Normalized maximum photocurrent as function of active layer thickness for each polymer blend processed from DCB

Compared with the non-fluorinated PNDT-DTBT polymers, both fluorinated analogues have lower absorption coefficients. Though the weaker intrinsic absorption of the fluorinated polymer-based blends are compensated by thicker active layers in their optimized devices, this thickness change amounts to a minor modification (~4%) in absorption as deduced from optical modeling of complete devices (Fig. 3.6). On the other hand, differences in absorption strength from the absorption coefficients (Fig 3.5b) plays a larger role and suggests 11% higher absorption for the C6,2-C6,2-based blend

compared to the fluorinated analogue. However, the J_{sc} improvement amounts to only 4% signifying a non-optical enhancement to the J_{sc} for the blend with C6,2-C6,2F The same is true when comparing the C8,4-based blends where the absorption is 16% *higher* for the non-fluorinated case, but the J_{sc} is actually 2 times *lower* for devices with C8,4-C6,2. Both comparisons indicate that addition of fluorine creates an electrical enhancement that compensates for the weaker intrinsic absorption. This yields nearly equivalent J_{sc} when comparing devices with C6,2-based polymers or significantly higher J_{sc} when comparing those with C8,4. As postulated above, changes in J_{sc} not related to absorption differences could be due to modifications in the structure introduced by F substituents, such as polymer crystal orientation (C8,4-C6,2/PC$_{61}$BM is the most "edge-on" of the four blend films) or morphology (C8,4-C6,2/PC$_{61}$BM has the finest surface morphology) in blend films, leading to improved charge generation and/or transport.

3.5.3 Charge Separation Probability
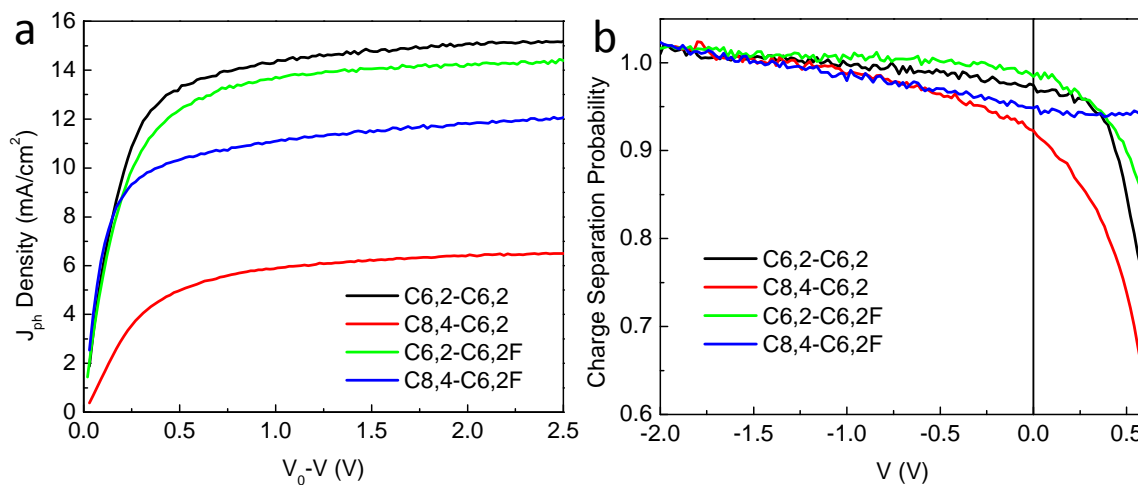
Figure 3.7. a) Photo current density vs. effective voltage and b) charge separation probability vs. applied voltage curves of optimized BHJ solar cells processed in dichlorobenzene under 1 Sun condition (100 mW/cm^2).

Along with enhanced J_{sc} that is not related to improved optical absorption, the devices based on fluorinated polymers consistently show better *FF* when compared with the non-

fluorinated polymer-based ones; in particular, the C8,4-C6,2F-based device demonstrates a high *FF* up to 63.6% (Table 3.3). In order to qualitatively understand the influence of fluorine substituents on *FF* of BHJ devices, we calculate the charge separation probability of each device. First, we obtain the photocurrent (J_{ph}) by subtracting the current density in the dark from that under the illumination. From the resulting J_{ph}-*V* characteristics, we determine the compensation voltage (V_0) at which J_{ph}=0. Fig. 3.7a plots the J_{ph} at room temperature (T=300K) against the effective voltage across the device (given by V_0-*V*). For a small reverse voltage (V_0–*V* <0.5), the photocurrent increases rapidly with effective voltage. However, for large reverse voltages (V_0–*V* >1), every generated bound e-h pair dissociates into free carriers by the applied field, and consequently the photocurrent becomes saturated and field-independent.[123] Because the J_{ph} dependence on cell voltage mainly arises from geminate pair recombination[124] and bimolecular recombination only dominates in the range of voltages close to V_{oc},[125] the recombination of free charge carriers can be neglected in the voltage-dependent J_{ph} loss. However, it has been recently argued that geminate pair recombination is independent of applied voltage[126] and the J_{ph} dependence on voltage is dominated by bimolecular recombination[127]. In this case, we take the former interpretation simply as an appropriate means to quantify differences in the J_{ph} voltage dependence of the different blends. For this case, the calculation of charge separation probability was then derived from Sokel and Hughes's solution for the photocurrent:[128]

$$J_{ph} = eGL\left[\frac{\exp\left(e(V_0 - V)/kT\right)+1}{\exp\left(e(V_0 - V)/kT\right)-1} - \frac{2kT}{e(V_0 - V)}\right]$$

(3.2)

where k is the Boltzmann constant, T is the temperature, e is the electric charge, L is the thickness of the active layer, and G is the generation rate of charge carriers. In reality, not all photogenerated bound e-h pairs (represented by G_{max}) dissociate into free charge carriers, which is determined in-part by the electric field strength (i.e., applied voltage). Consequently, the generation rate of free charge carriers (G) can be described by[123]

$$G = G_{max} P$$
(3.3)

where P is the charge separation probability. At high effective voltage ($\frac{\exp(e(V_0 - V)/kT) + 1}{\exp(e(V_0 - V)/kT) - 1} - \frac{2kT}{e(V_0 - V)} \approx 1$) where all photogenerated bound e-h pairs dissociate into free charge carriers ($G = G_{max}$), the photocurrent becomes saturated (J_{ph}^{sat}) and can be described by $J_{ph}^{sat} = eG_{max}L$. Substitution of equation (3.3) into equation (3.2) and then replacing $eG_{max}L$ with J_{ph}^{sat}, equation (3.2) can be further solved to yield equation (3.4), in which the charge separation probability P is given by:

$$P = \frac{J_{ph}}{J_{ph}^{sat}} / \left[\frac{\exp(e(V_0 - V)/kT) + 1}{\exp(e(V_0 - V)/kT) - 1} - \frac{2kT}{e(V_0 - V)} \right]$$
(3.4)

According to equation (3.4), the charge separation probability in BHJ devices based on each of four polymers can be calculated and plotted as a function of applied voltage (Fig. 3.7b). At large applied reverse voltages ($V < -1.5$), charge separation probabilities of all four BHJ devices is close to 100%, implying every photogenerated bound e-h pair is dissociated into free carriers by the high applied field as discussed previously. However, charge separation probability decreases with decreasing reverse voltage. This occurs

because only a certain fraction of *e-h* pairs escape recombination (due to their mutual Coulomb attraction) under small external electric field.

Fig. 3.7b clearly indicates a higher charge separation probability from devices based on fluorinated polymers than that of the corresponding polymer with identical side chains (e.g., C8,4,-C6,2F vs. C8,4-C6,2), especially near maximum power point. Fluorine (F) is the most electronegative element in the periodic table, with a Pauling electronegativity of 4.0, much larger than that of hydrogen (2.2).[129] It is very likely that introduction of the most electronegative element (F) creates strong internal dipole moments which lower the Coulombic potential between the *e-h* pairs.[130] It is also possible that adding F atoms at the polymer/PC$_{61}$BM interface increases the *e-h* pair separation distance after charge transfer. Both effects would lead to weaker Coulombic attractions between *e-h* pairs after exciton splitting, indicating a low recombination rate via the introduction of these fluorine substituents. Attributed to the retardation of the recombination rates, devices based on the fluorinated polymers exhibit larger charge separation probability and generate more photocurrent at weaker fields, which results in an improved *FF* when compared with the non-fluorinated polymers. For example, the C8,4-C6,2F-based device with high charge separation probability even for weak electric fields exhibits the highest *FF* among all devices.

The retardation, via these F substituents, of the recombination rates also contributes to the differences in J_{sc}. However, J_{sc} is determined by (a) the maximal amount of potentially separable photogenerated *e-h* pairs (represented by J_{ph}^{sat}) and (b) charge separation probability at short circuit, both of which are largely influenced by the morphology of the BHJ blend. Take the C6,2-C6,2 polymer and its fluorinated analog for

example. Although the C6,2-C6,2F-based devices show a higher charge separation probability than the non-fluorinated analogs at short circuit (Fig. 3.7b), a slightly lower J_{sc} was observed in the C6,2-C6,2F-based devices (Table 3.3) due to the smaller amount of available charges in the C6,2-C6,2F-based devices (lower J_{ph}^{sat} shown in Fig. 3.7a and partially dictated by differences in light absorption). As discussed earlier, if an optimal morphology was reached (e.g. C6,2-C6,2 polymer blend), the extra π-π stacking of conjugated backbones via the introduction of F atoms could decrease polymer solubility and thereby promote the formation of large phase-separated domains and non-uniform BHJ films (e.g. C6,2-C6,2F polymer blend). This would reduce the interfacial area between the donor molecules and acceptor molecules, thereby diminishing the amount of photogenerated e-h pairs (lower J_{ph}^{sat}). On the other hand, adding F substituents to the C8,4-C6,2 polymer optimizes orientation of these conjugated backbones to "face on" (Fig. 3.4d vs. 3.4b) and promotes their weak π-π stacking in C8,4-C6,2 thin films (Fig. 3.3d vs. 3.3b), which likely facilitates the generation of potentially separable e-h pairs (a higher J_{ph}^{sat}). The much improved J_{ph}^{sat}, together with the retardation of recombination at short circuit, leads to a significantly increased J_{sc} in the C8,4-C6,2F-based BHJ device than that of the non-fluorinated analog-based BHJ device. Together with very high *FF* and enhanced V_{oc}, which are attributed to the combined effect of long C8,4 side chains and fluorine substituents, a high overall efficiency exceeding 5.6% was observed for the C8,4-C6,2F-based device, the highest of the blends studied in this work.

3.6. Photovoltaic Properties of BHJ Devices Processed with Chlorobenzene (CB)
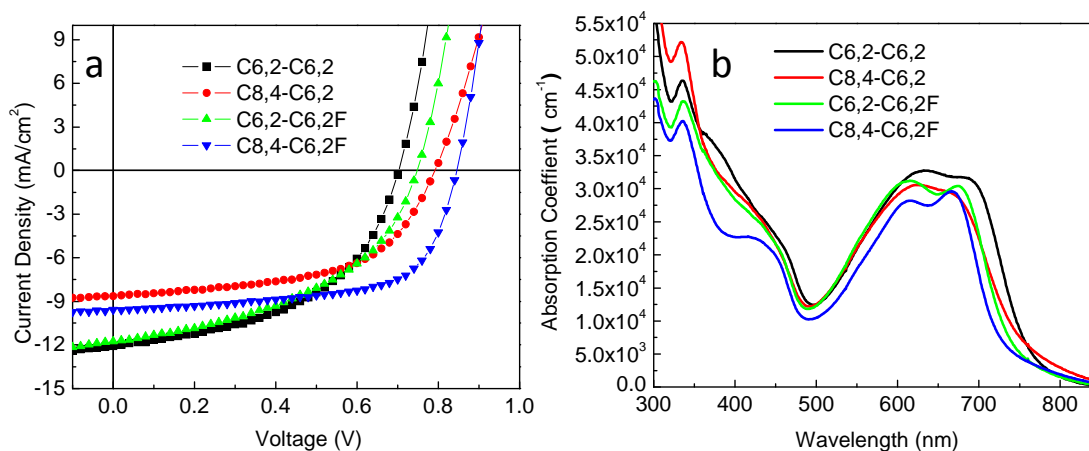
Figure 3.8. a) Current density vs. voltage characteristics of optimized BHJ solar cells processed in chlorobenzene under 1 Sun condition (100 mW/cm^2). b) Absorption coefficient of polymer/PC$_{61}$BM thin films spun coated with chlorobenzene.

Compared with *o*-dichlorobenzene (DCB) which has a high boiling point of 180°C, lower boiling point solvents, such as chlorobenzene (CB), can provide limited solubility of polymers and short solvent annealing time of the BHJ blend. Thus, using lower boiling solvents can change the stacking ability and orientation of polymer backbones. In order to further study the influence of fluorine and side chain on the performance of polymer solar cells, devices based on these four polymers were also processed in their CB-based solutions at low temperature (100°C). As we already observed in devices processed in DCB, the two fluorinated polymers exhibit more pronounced absorption shoulders than the non-fluorinated polymers (Fig. 3.8b), indicating strong π-π stacking introduced by these F substituents. Similarly, due to the less space occupied by short side chains, polymers with short side chains exhibit larger polymer backbone density and consequently slightly higher absorption coefficients.

Table 3.5. Photovoltaic performances of optimized devices processed in chlorobenzene.

Polymer	Polymer: $PC_{61}BM$	Processing Solvent	Thickness (nm)	V_{oc} (V)	J_{sc} (mA/cm^2)	FF (%)	η (%)
C6,2-C6,2	1:1	CB	82	0.71	12.06	48.89	4.19
C8,4-C6,2	1:1	CB	104	0.79	8.76	56.10	3.83
C6,2-C6,2F	1:1	CB	106	0.75	11.76	46.04	4.06
C8,4-C6,2F	1:1	CB	111	0.85	9.58	64.49	5.25

Indeed, switching to lower boiling point solvent has noticeable impact on device performance (Fig. 3.8a and Table 3.5). In some cases, the impact is quite dramatic. First, we observe a significantly improved performance in the C8,4-C6,2-based device fabricated from the CB solution: its efficiency doubles that of the device processed with DCB, mainly due to the much improved J_{sc}. This is likely because CB, with a lower boiling point, can shorten solvent annealing time for molecular rearrangement, thereby partially 'freezing' the random orientational alignment of polymer backbones prior to crystallization. This is indeed the case from GI-WAXS measurements on C8,4-C6,2/$PC_{61}BM$ blend films processed from CB as shown in Fig. 3.9. The strong (100) reflections in the OOP direction are completely destroyed, rendering the polymer much more amorphous. The random orientation of polymer backbones rather than "edge-on" for C8,4-C6,2/$PC_{61}BM$ processed from DCB may help explain the J_{sc} improvement from 5.47 mA/cm^2 in DCB To 8.46 mA/cm^2 in CB. Second, it appears that the introduction of fluorine to the C6,2-C6,2 polymer has some negative effect on photovoltaic properties of the resulting polymer C6,2-C6,2F. As indicated in previous discussion, both the short side chain C6,2 and the F substituent can induce very strong π-π stacking among polymer backbones. As a result, we noticed that polymer C6,2-C6,2F with both the short side

chain C6,2 and fluorine substituent had a very poor solubility in low boiling point solvent CB. This poor solubility of the C6,2-C6,2F polymer in CB was also reflected by the large agglomerations in the AFM height image of its thin film (Fig. 3.10). This agglomeration and non-uniform morphology in the C6,2-C6,2F/PC$_{61}$BM BHJ thin film led to a decreased *FF* and corresponding slight decrease in the overall efficiency.
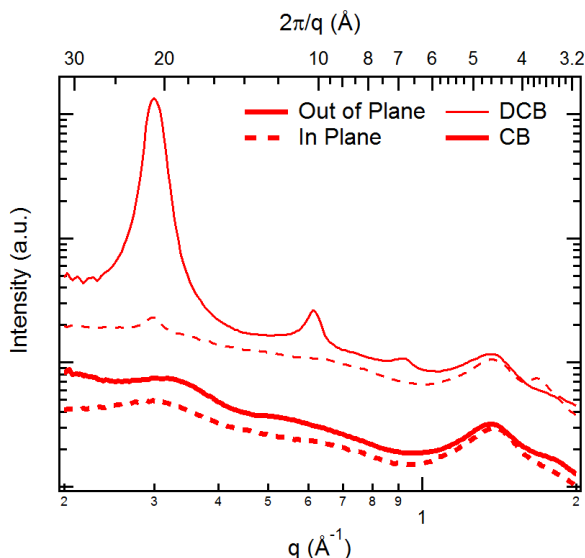
Figure 3.9. The GI-WAXS sector averages of C8,4-C6,2-based polymer:PC$_{61}$BM BHJ films processed with different solvents.

As discussed earlier, switching from C6,2 to long branch side chain C8,4 weakens π-π stacking in the polymer C8,4-C6,2F, resulting a good solubility in CB. A good solubility, together with the effect of the F substituent, leads to a high *FF* in C8,4-C6,2F-based devices. Combing a high *FF* with a respectable J_{sc} and high V_{oc} ascribable to the synergistic effect of long bulky side chain and fluorine, the C8,4-C6,2F-based BHJ device exhibits the highest efficiency of 5.25% among all these polymer-based devices processed by CB. Therefore, varying the processing solvent has little effect on the performance of devices based on the C8,4-C6,2F polymer. This "solvent-insensitivity" with consistently high efficiency could be beneficial to future roll-by-roll processing.
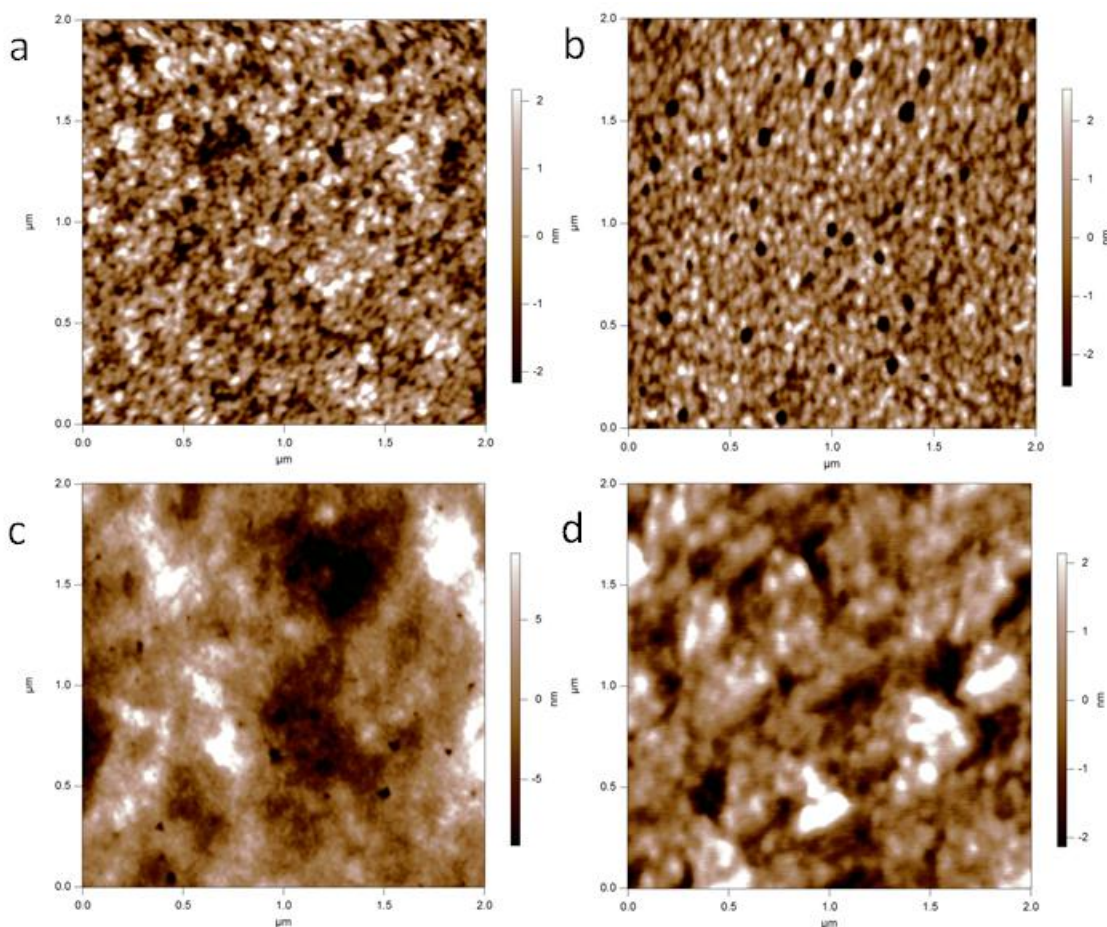
Figure 3.10. AFM height images of a) C6,2-C6,2, b) C8,4-C6,2, c) C6,2-C6,2F and d) C8,4-C6,2F based BHJ devices processed with chlorobenzene.

3.7. Conclusion

This detailed study of PNDT-DTBT polymers with an identical conjugated backbone but different side chains and F substituents complements our previous independent discoveries of the effects of the side chains and the F substations on photovoltaic properties of polymer-based solar cells. It becomes clear that side chains and F substituents have strong influences on the intermolecular interactions (in particular, at the polymer/fullerene interface), thereby exerting significant impacts on the photovoltaic properties of conjugated polymer-based BHJ cells. For the C8,4-C6,2 polymer with long chains of C8,4, introducing the most electronegative element, F, to the conjugated

70

backbone noticeably increases the charge separation probability as manifested in improvements in the J_{sc} and *FF*. Furthermore, the polymer with F substituents tends to adopt an increasingly "face on" orientation to the substrate. This preferred orientation could assist charge transport, and when combined with increased charge separation probability, explains a significantly higher J_{sc} for the fluorinated polymer-based BHJ devices than that of the non-fluorinated polymer-based ones. Additionally, long, branched side chains such as C8,4 help weaken the polymer/$PC_{61}BM$ intermolecular interaction and suppresses the dark current, which together with a lower HOMO level by the electronegative F substituents, leads to the highest V_{oc} for the C8,4-C6,2F-based BHJ device. These factors contribute to the observed highest efficiency of C8,4-C6,2F-based solar cells in the studied series of polymers. On the other hand, polymers with shorter side chains (e.g., C6,2-C6,2) have a strong tendency to aggregate, which indeed helps optical absorption and potentially charge transport yielding a higher J_{sc}, when compared with the C8,4-C6,2-based device. However, these short chain polymers also show concomitant poor solubility and difficult morphological control, which are exacerbated by the addition of F substituents. Thus only little improvement on the efficiency is observed for the fluorinated short chain polymer (C6,2-C6,2F) based BHJ cell when compared with the C6,2-C6,2-based one. In conclusion, our results indicate that an appropriate combination of side chains and F substituents can maximize the energy harvesting potential of a given conjugated backbone in its BHJ devices.

CHAPTER 4

POLY(3-METHYLTHIOPHENE) AS A HOLE TRANSPORT LAYER FOR HIGH PERFORMANCE POLYMER SOLAR CELLS

4.1. Introduction

In most BHJ polymer solar cells, PEDOT:PSS has become the standard material for increasing the work function of ITO for effective hole collection. However, a number of drawbacks exist with this approach that limits the application of polymer solar cells: the acidic nature of PEDOT:PSS can corrode the ITO electrode,[44,45] leading to a chemical instability at the interface,[46] and PEDOT:PSS does not have sufficient electron blocking capability,[45] which could render electron leakage at anode to reduce the J_{sc}.

The research community has proposed several new interfacial layers as viable replacements for PEDOT:PSS for polymer solar cells applications.[24,27,47-54] For example, a self-doped, grafted conductive copolymer (PSSA-g-PANI), has been reported for photovoltaic applications. The conductivity and acidity of this copolymer can be easily tuned by varying the PSSA and PANI molar ratio.[55] Most importantly, OPV devices based on optimized PSSA-g-PANI film exhibited better thermal stability and efficiency than those of the PEDOT:PSS-based control device. PSSA-g-PANI can also be doped by introducing perfluorinated ionomer (PFI). Devices based on the PFI-doped PSSA-g-PANI showed a more than 30-fold increase in lifetime compared to the PEDOT:PSS based device. However, the acidic and hygroscopic nature of these conducting polymers may lead to similar degradation problems as found in PEDOT:PSS. Recently, p-Type

transition metal oxides such as vanadium oxides (V_2O_5)[56], nickel oxides (NiO_x)[57], and molybdenum oxide (MoO_3)[24,47] have also been used as another class of hole transport layer for OPVs. Compared with PEDOT:PSS, these large bandgap metal oxides possess better optical transparency in the visible and near infrared regions. In addition, the conduction band of these p-type semiconducting oxides is sufficiently higher than the LUMO of acceptor materials, which can effectively work as electron blocking layer, leading to small electron leakage through the anode. However, most of the p-type metal oxide films required vacuum deposition processes, which are incompatible with the high throughput printing processes.

In this Chapter, uniform poly(3-methylthiophene) (P3MT) films are fabricated with thickness values ranging from 3 to 20 nm on ITO surfaces by surface-initiated Kumada catalyst-transfer polycondensation (SI-KCTP) using surface bound (aryl)Ni(II)-Br Initiators.[131-133] The P3MT interfacial layer is covalently bound, preventing delamination during processing of additional layers, which successfully served as the hole transport layer (HTL) for solution-processed BHJ polymer solar cells with a typical configuration of ITO/P3MT/polymer:$PC_{61}BM$/Ca/Al (Fig. 4.1). We were able to obtain cell efficiencies as high as 5% based on doped thin P3MT interfacial layers in our investigation. Moreover, due to the stability of P3MT/ITO substrates, devices based on reused P3MT/ITO substrates extracted from old devices exhibit satisfactory efficiency as high as the original devices. All these doped P3MT-based devices exhibited satisfactory performance with little optimization, indicating that P3MT interfacial layers are a promising alternative to PEDOT:PSS as the hole transport layer for OPVs.
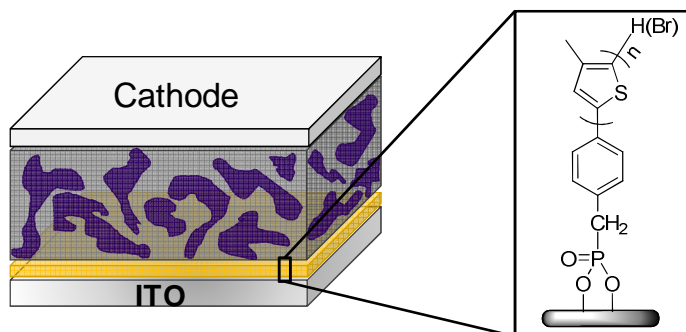
Figure 4.1. The device structure of the BHJ polymer solar cell based P3MT interfacial layer. The P3MT interfacial layer is covalently bound to ITO surfaces by surface-initiated Kumada catalyst-transfer polycondensation (SI-KCTP) using surface bound (aryl)Ni(II)-Br Initiators, preventing delamination during processing of additional layers.

4.2. Experimental Section

4.2.1. Fabrication of Interfacial Modifiers.

All interfacial layers were fabricated using SI-KCTP. Film thickness was varied by adjusting the concentration of monomer, where films 3-5 nm thick were derived from the lowest concentration of 0.02M and films >20 nm were derived from a 0.2M concentration. A glass slide holder was used to hold large area substrates (4 total in each trial) in an upright fashion and polymerization was conducted without stirring. Control substrates that did not undergo the catalyst immobilization step demonstrated no signs of P3MT, implying the absence of physisorption processes. Film thickness values were estimated based on the UV-Vis absorption max and AFM, where a 0.1 absorbance unit correlates to a 10 nm film thickness.[131]

A typical procedure involves the cleaning of patterned ITO substrates in an ultrasonic bath for 15 minutes in water, then 15 minutes in IPA. After drying under a nitrogen stream, substrates were ozone cleaned for 15 minutes. Immediately after, cleaned

substrates were placed in a 5 mM solution of phosphonic acid for 48 hours. The functionalized substrates were then removed from the solution and annealed under nitrogen for 12 hours (150 C). After annealing, the functionalized substrates were extensively rinsed with ethanol, dried under a nitrogen stream, and transferred to a glovebox. A 20 mL toluene solution of Ni(COD)2 (60 mg) and 2,2'-bipyridine (34 mg) was prepared and poured over the substrates in a glass slide holder. This was left for one hour. The solution was decanted and the Ni(II)bpy functionalized substrates were rinsed 2x with toluene and 1x with THF. A 20 mL solution of dppp (100 mg) was poured over the substrates and left for 1 hour. The ligand exchange solution was decanted and the Ni(II)dppp functionalized substrates were rinsed 3 times with THF. A solution of monomer was then poured over the Ni(II)dppp functionalized substrates and left for 12 hours at room temperature. After polymerization, substrates were carefully removed from the solution and rinsed extensively with water, ethanol, and DCM. Slides were sonicated in chloroform to ensure no physisorbed polymers were present on the substrates.

Synthesis of 2-bromo-5-iodo-3-methylthiophene is reported elsewhere.[131] For the magnesiation step, 0.9 equiv. of isopropylmagnesium chloride was added dropwise to a THF solution of 2-bromo-5-iodo-3-methylthiophene at 0 C. This was stirred for 1 hour at 0 C and warmed to room temperature prior to use.

4.2.2. Polymer Solar Cell Fabrication and Testing.

Prior to use, bare ITO substrates were ultrasonicated for 20 minutes in acetone followed by deionized water and then 2-propanol. The ITO substrates were dried under a stream of nitrogen and subjected to the treatment of UV-Ozone over 30 minutes. A

filtered dispersion of PEDOT:PSS in water (Baytron PH500) was then spun cast onto clean ITO and Ag NW substrates at 4000 rpm for 60 seconds and then baked at 140 °C for 10 minutes to give a thin film with a thickness of 40 nm.   No further treatment was applied to P3MT/ITO substrates before using.   Blends of polymer and $PC_{61}BM$ (1:1 weight ratio) were dissolved in DCB with heating at 120 °C for 6 hours. All the solutions were spun cast at 500 rpm for 60 seconds onto the substrates. The substrates were then dried at room temperature in the glovebox under a nitrogen atmosphere for 12 hours. The devices were finished for measurement after thermal deposition of a 30 nm film of calcium and a 70 nm aluminum film as the cathode at a pressure of $\sim 2 \times 10^{-6}$ mbar. There are 8 devices per substrate, with an active area of 12 mm^2 per device.   All fabrication and characterization steps after adding the PEDOT:PSS layer onto ITO were performed in gloveboxes under a nitrogen atmosphere. For more experimental details about reagents, instrumentation, and spectroscopy please check **Appendix A**.

4.3. Properities of P3MT Interfacial Layer

Fig. 4.2a compares the optical transmittance of undoped P3MT on ITO substrates, with that of a PEDOT:PSS-coated reference substrate. All of the undoped P3MT films exhibit excellent transparency at wavelengths over 650 nm.   The lowest transmittances of undoped P3MT layers appear at 450 nm, which is lower than reports of P3HT in the dry state.[134] This can be attributed to the presence of oligomeric material resulting from early chain termination.[131] With the thickness of P3MT increasing to 20 nm, the transmittance of the P3MT film decreased to 75% at 450 nm, which implies that P3MT layers over 20 nm thick may have negative effect on the performance of solar cells due to low transmittance.   On the other hand, the optical transmittance of PEDOT:PSS peaks

(99.2 %) around 430 nm, but continually decreases to 90 % at 850 nm. Thus, while PEDOT:PSS/ITO substrates might be slightly advantageous for applications targeting the visible region, P3MT outperform PEDOT:PSS for applications requiring optical transparency extending into longer wavelength (e.g., small band gap solar cells). Interestingly, after electrochemically doping the film, the transmittance of P3MT film dramatically decreased at a long wavelength range (over 450 nm); and the lowest transmittance red shifts to 500 nm (Fig 4.2b). This is indicative of polaronic and bipolaronic states along the P3MT backbone, which leads to red shift in the transmittance spectra.
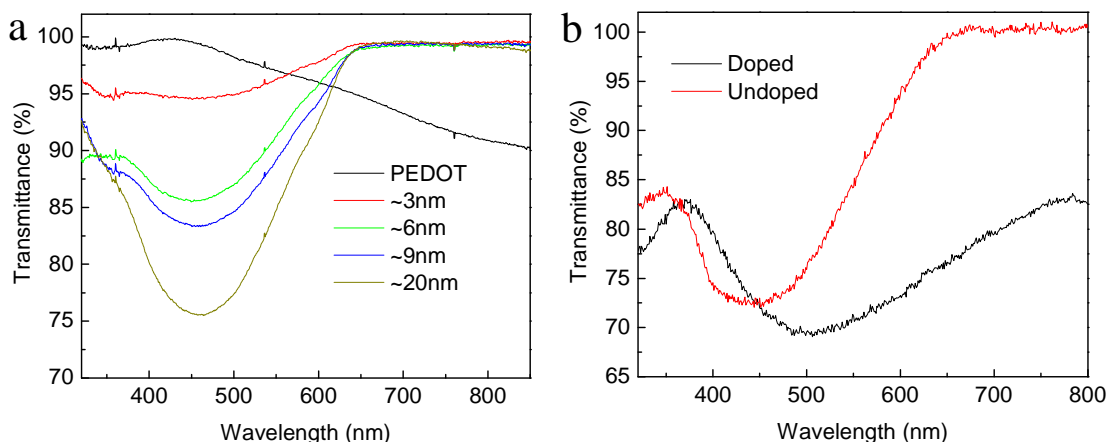
Figure 4.2. Transmission spectra for a) 40 nm PEDOT:PSS reference and a series of undoped P3MT layers with different thicknesses, and b) P3MT layer before and after doping.

4.4. Photovoltaic Properties of Devices Based on Doped P3MT Layer

In order to comprehensively investigate the application of these P3MT interfacial layers as the hole transport layer in solution-processed BHJ polymer solar cells, we selected two representative polymers, P3HT and PBnDT-DTffBT[30]. These two polymers

are largely different in energy levels and band gaps: the HOMO energy level and optical band gap are – 5.2 eV and 1.9 eV in P3HT,[52] and are – 5.54 eV and 1.7 eV in PBnDT-DTffBT.[30] Representative current-voltage curves of devices based on 9 nm P3MT HTL and reference cells are shown in Fig. 4.3, with key photovoltaic characteristics and processing conditions summarized in Table 4.1 and Table 4.2.
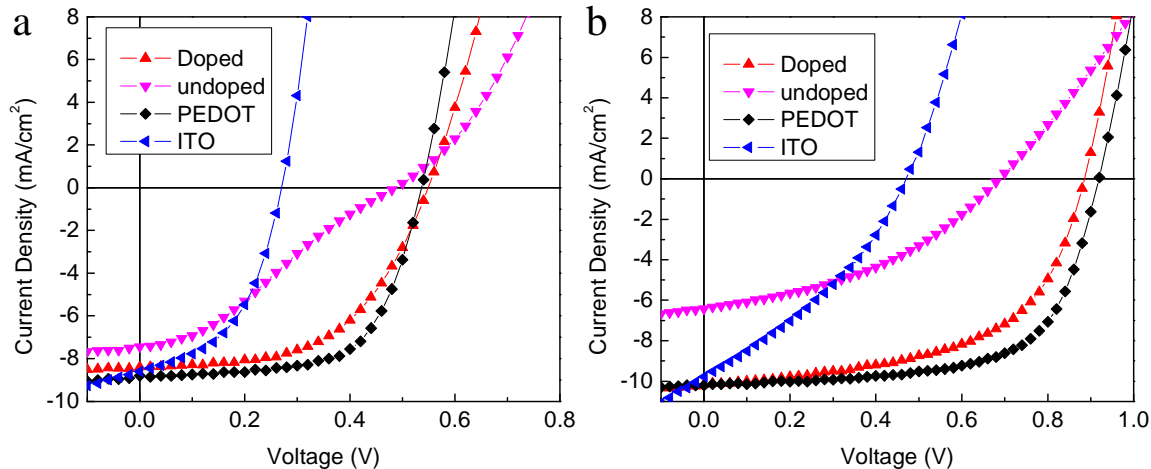
Figure 4.3. Characteristic *J-V* curves of the BHJ solar cell devices based on a) P3HT and b) PBnDT-DTffBT under one Sun condition (100 mW/cm^2)

Compared with the reference devices based on bare ITO anodes, there is a noticeable increase in the V_{oc} of all devices based on undoped P3MT/ITO substrates, due to the modified work function of ITO surface. However, the lower J_{sc} and FF of undoped P3MT-based devices counteract the effect of increased V_{oc}, leading to a similar low efficiency as that of bare ITO-based devices. The low J_{sc} and FF of these undoped P3MT-based devices are largely attributed to the low mobility and poor charge transport of undoped P3MT interfacial layers. The hole mainly transports through the intermolecular π-π stacking of conjugated polymer backbones. However, the π-π stacking of P3MT randomly orientated to the ITO anode due to low grafting density,[131] leading to a low mobility and poor charge transport in the vertical direction. Therefore, the undoped

P3MT interfacial layers work as free charge blocking layer between the active layer and ITO anode, which results in low J_{sc} and poor FF. Surprisingly, all the devices based on doped P3MT interfacial layers exhibit an improved J_{sc} and V_{oc}, which is closed to that of the PEDOT reference cells. This is attributed to doping of the P3MT layer, which generates polaronic and bipolaronic states to facilitate charge transport. In addition, the relatively high LUMO level of P3MT inhibits the electron transfer from active layer to ITO anode. Therefore, the doped P3MT interfacial layer can be considered as a hole only transport layer for BHJ solar cells based on conjugated polymers with a wide range of HOMO levels (e.g. – 5.2 eV in P3HT and are – 5.54 eV in PBnDT-DTffBT). However, relatively low FF were observed in the doped P3MT-based devices when compared with PEDOT:PSS based reference cell, which may be attributed to the low HOMO level of P3MT layer. These results imply after further optimization of the P3MT interfacial layer electronic properties, the performance should be as good as that of PEDOT:PSS based devices.

Table 4.1. Photovoltaic properties of devices based on undoped P3MT/ITO.

Polymer	P3MT layer	V_{oc} (V)	J_{sc} (mA/cm^2)	FF (%)	η (%)
P3HT	~3nm	0.39	7.14	36.87	1.03
	~6nm	0.45	6.57	40.01	1.18
	~9nm	0.49	7.54	29.38	1.07
	~20nm	0.45	5.26	43.35	1.03
PBnDT-DTffBT	~3nm	0.77	7.05	39.76	2.16
	~6nm	0.71	6.48	34.10	1.57
	~9nm	0.69	6.42	39.63	1.76
	~20nm	0.67	6.61	32.51	1.44

4.5. Effect of P3MT Thickness on the Performance of Devices
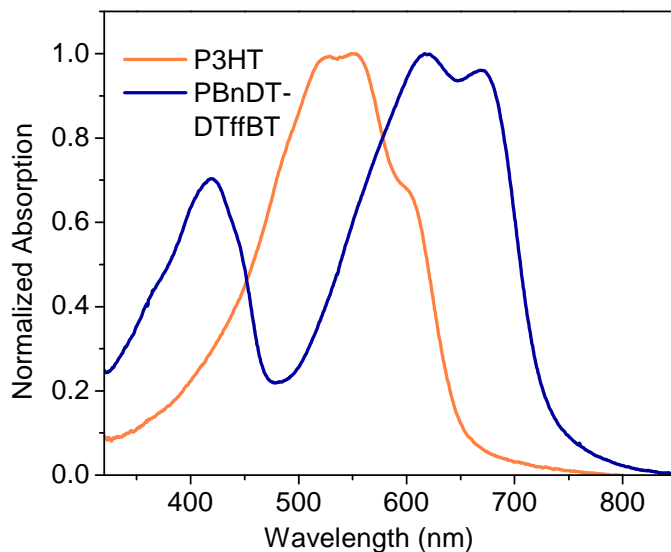
Figure 4.4. Optical properties of P3HT and PBnDT-DTffBT

The effect of thickness of P3MT interfacial layers on the photovoltaic properties of BHJ devices was also investigated. All the doped P3MT-based devices (Table 4.2) exhibit better performance than that of undoped P3MT-based devices with corresponding P3MT thickness (Table 4.1). It is consistent with our previous discovery that doping can significant improve the charge transport efficiency of P3MT layer, leading to a better performance. For these doped P3MT-based devices, the best performance is observed in the device based on a 9nm P3MT layer, regardless of which donor polymer is used (P3HT and PBnDT-DTffBT). It is possible that P3MT can hardly form a uniform layer on ITO surface under a small thickness (~3 nm), leading to relatively low FF and J_{sc}. On the other hand, thick P3MT layer (~20 nm) significantly reduces the transmittance of P3MT/ITO substrate, resulting in a decreased J_{sc}. Therefore, ~ 9nm thick P3MT layer provides a balance between the hole transport and the transmittance, resulting in the highest possible efficiency in both P3HT and PBnDT-DTffBT based BHJ devices.

Interestingly, the J_{sc} of P3HT-based devices dramatically decreased from 8.4 to 5.8 mA/cm^2, when the thickness of P3MT interfacial layer increased from 9 nm to 20 nm. Meanwhile, only a small decease of J_{sc} was observed in the PBnDT-DTffBT-based devices under the same conditions. It is because the absorption of the doped P3MT interfacial layer is largely overlapped with the absorption of P3HT (Fig. 4.4). For devices based on a smaller band gap polymer, the thick P3MT interfacial layer will have less effect on the photovoltaic properties. For example, a device of PBnDT-DTffBT based on 20 nm P3MT interfacial layer still exhibits efficiency as high as 4.7%, which is only 6% lower than that of the 9 nm P3MT based device.

Table 4.2. Photovoltaic properties of devices based on doped P3MT/ITO, PEDOT:PSS/ITO, and bare ITO. [a]

Polymer	Substrates	V_{oc} (V)	J_{sc} (mA/cm^2)	FF	η (%)
P3HT	Bare ITO	0.27	8.61	48.43	1.12
	~3nm P3MT	0.45	6.81	47.52	1.46
	~6nm P3MT	0.49	7.45	55.06	2.03
	~9nm P3MT	0.55	8.39	54.49	2.51
	~20nm P3MT	0.47	5.81	46.51	1.27
	PEDOT:PSS	0.53	8.80	64.76	3.02
PBnDT-DTffBT	Bare ITO	0.47	9.78	34.32	1.58
	~3nm P3MT	0.87	7.62	52.27	3.42
	~6nm P3MT	0.89	10.10	53.89	4.85
	~9nm P3MT	0.89	10.16	55.72	5.04
	~20nm P3MT	0.87	9.76	55.82	4.74
	PEDOT:PSS	0.91	10.21	65.59	6.09

[a] All polymers were blend with PC$_{61}$BM at a weight ratio of 1:1 in dichlorobenzene.

4.6. Stability and Re-usability of P3MT Interfacial Layer

Due to the covalent immobilization of the P3MT chains, the P3MT interfacial layers on ITO substrates are very stable in air and insoluble in water and organic solvents. Therefore, the P3MT/ITO substrates can be reused for BHJ devices after wiping out the polymer/$PC_{61}BM$ active layer. In this study, old devices (over one month since fabrication) based on 9 nm doped P3MT were ultrasonicated for 20 minutes in hot DCB followed by acetone, deionized water and then 2-propanol to clean all the layers above P3MT/ITO substrate. In order to investigate the stability of doping level, half of these cleaned old P3MT/ITO substrates were electrochemically redoped; and no further treatment was applied to the other half. Representative current-voltage curves of devices based on these reused P3MT/ITO substrates using PBnDT-DTffBT as donor polymers are shown in Fig. 4.5. Efficiency of the device based on reused P3MT/ITO substrate with no treatment is significantly low than that of the original doped devices (5% in Table 4.2). After redoping the reused P3MT/ITO substrate, the efficiency of devices based on the redoped substrate recovers to 4.7%, which is as high as that of the original doped devices. These results indicate that no damage to the P3MT layer occured during the cleaning procedures, which can be attributed to covalent attachment to the ITO substrate. The counter ions on doped P3MT layers were partially washed out in water and organic solvents under sonication. Due to the residual counter ions, devices based on reused P3MT with no treatment still exhibit better performance than that of the undoped original P3MT device.
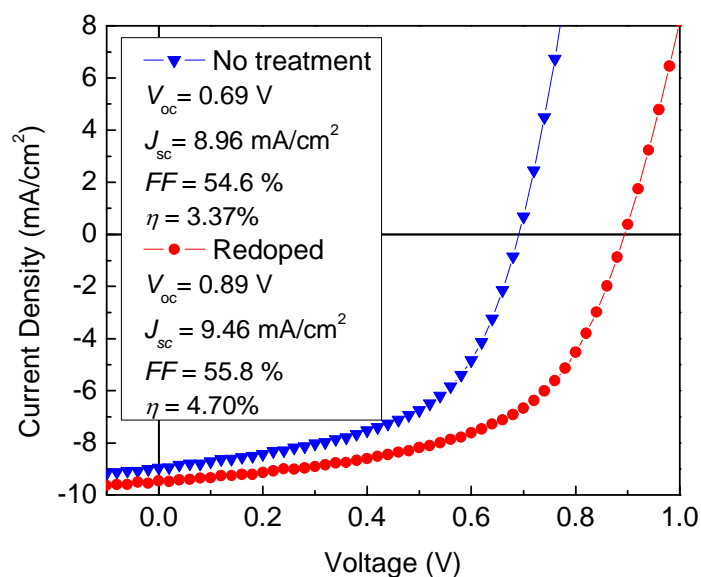
Figure 4.5. Characteristic *J-V* curves of the BHJ solar cell devices based on reused P3MT/ITO substrates under one Sun condition (100 mW/cm^2)

4.7. Conclusion

P3MT interfacial layers on ITO electrodes were fabricated through SI-KCTP. After doping, these P3MT interfacial layers successfully served as the hole transport layer for solution-processed BHJ polymer solar cells. With an optimized thickness of P3MT layers, the doped P3MT devices exhibit high efficiency, which is closed to that of the PEDOT reference cells. More importantly, unlike acidic PEDOT:PSS which leads to chemical instability at the ITO/PEDOT:PSS interface, the P3MT/ITO substrate is stabile in air, water, and organic solvents, even under sonication in hot DCB. Devices based on P3MT/ITO substrates from old devices by removal of active layer and metal electrode exhibit efficiency as high as the original devices. Though the best devices based on P3MT/ITO substrate in our investigation still exhibit a lower FF compared that of PEDOT:PSS-based devices, we believe after further investigation and optimization, the

modification of ITO with a covalently bound P3MT interfacial layer is a promising approach to replace PEDOT:PSS in OPV devices.

CHAPTER 5

SOLUTION PROCESSED FLEXIBLE POLYMER SOLAR CELLS WITH SILVER NANOWIRE ELECTRODES [*]

5.1 Introduction

Rapid progresses in the development of new materials and device optimization have brought commercialization of polymer solar cells closer to reality, with recent reports citing efficiencies over 7 %.[12,21,26,28,30] However, a critical roadblock to the commercialization of polymer solar cells is the transparent conductive electrode (e.g., the anode). The conventional anode of choice for organic solar cells has been indium tin oxide (ITO) due to its excellent transparency and conductivity. However, ITO has several longstanding disadvantages. First, the cost of ITO thin films is very high, primarily because ITO thin films must be vapor-deposited at rates orders of magnitude slower than solution-based coating processes. Second, indium is a relatively scarce element. Third, the brittleness of ITO renders it susceptible to mechanical damage, making it unsuitable for use with mobile, flexible electronic systems.[60]

The research community has proposed several new transparent electrodes as viable replacements for ITO for OPV applications, including single-wall carbon nanotubes (SWNTs), multiwall-carbon nanotubes (MWNTs), and graphene.[61-68] However, the high sheet resistance of MWNTs or graphene-based electrodes (typically several hundred $\Omega/\square$

---

at 80% optical transmittance in the visible range) results in solar cells fabricated with these electrodes having a relative low efficiency.[64,68] Conductive transparent SWNTs films have met much more successes: for example, Blackburn *et al.* achieved an efficiency over 3% with P3HT:PC$_{61}$BM cells on SWNTs electrodes with PEDOT:PSS as the hole transport layer,[135] and 2.65 % without the hole transport layer,[136] a noticeable improvement over previous literature results.[65] However, these SWNTs electrodes are fabricated via multiple steps, which could potentially lead to a high manufacturing cost. Metal nanogrids based on copper and silver have been developed as transparent electrodes with low sheet resistance,[69,70] but the fabrication of these nanogrids requires costly lithographical steps that cannot be easily scaled in a cost-effective manner. More recently, a high-performance transparent electrode (90 % at 50 Ω/□) based on electrospun copper nanofiber networks was developed.[71] Organic solar cells using these copper nanowire networks as transparent electrodes have reached power efficiencies of 3.0 %, comparable to control devices made with ITO electrodes. Unfortunately, electrospinning is an inherently low-throughput process that has not yet witnessed much commercial success despite being first patented in the 1930's.[137]

Solution-processed networks of silver nanowires (Ag NWs) have a sheet resistance and transmittance comparable to those of ITO (10-20 Ω/□ at 80 % transmittance), together with a relatively high work function of 4.5 eV (Fig. 5.1a).[72-74] Therefore, films of Ag NWs have been touted as one of the most promising alternatives to ITO for high-throughput roll-to-roll manufacturing of low-cost transparent conducting films for OPV applications. For example, solution-processed Ag NW transparent electrodes have recently been used as the cathode for a BHJ solar cell,[75] and as the anode for an inverted

cell.[76] Ag NW films have also been demonstrated as the anode for a vacuum-deposited bilayer solar cell.[72] However, there is no prior report that uses Ag NW thin films to replace ITO as the bottom anode in solution-processed BHJ devices, likely due to the significant challenges associated with such a demonstration. One challenge is that Ag NW network electrodes are relatively rough; the Ag NWs that make up the film can easily penetrate the thin layer (~ 100 nm) of solution-processed polymer/$PC_{61}BM$ blend atop the Ag NW electrode, resulting in a short-circuited device. To address these challenges, we fabricated highly conductive Ag NW films by spraying an aqueous solution of Ag NWs onto a substrate (glass or plastics) with an air brush. These highly transparent yet remarkably conductive Ag NW films successfully served as the anode for solution-processed, flexible BHJ organic solar cells with a typical configuration of Ag NWs/PEDOT:PSS/polymer:$PC_{61}BM$/Ca/Al (Fig. 5.1b). We were able to obtain cell efficiencies as high as 2.5 % with a new low band gap polymer in our investigation (*vide infra*). To further probe the effects of the Ag NW electrode on the performance of OPVs and the underlying performance-limiting principles, we have investigated three different polymers, each having different energy levels and processing parameters in the device fabrication, in OPV devices with Ag NW films as the anode. All these OPV devices exhibited satisfactory performance with little optimization, indicating that Ag NWs are a promising alternative to ITO as the anode for OPVs.
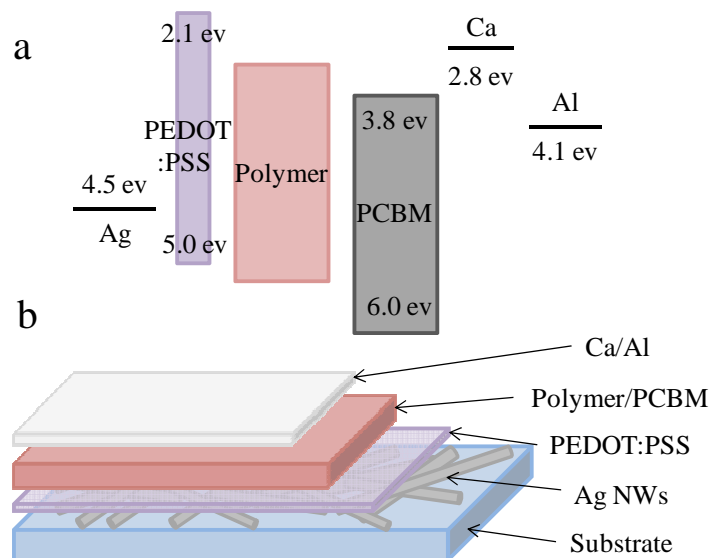
Figure 5.1. a) Energy-level diagram showing the highest occupied molecular orbital (HOMO) and lowest unoccupied molecular orbital (LUMO) energies and work functions of each of the component materials. b) The device structure of the solution-processed BHJ polymer solar cell with the Ag NW anode.

5.2. Experimental Section

5.2.1. Synthesis of Silver Nanowires

Round bottom flasks and stir bars were cleaned with concentrated nitric acid and rinsed with deionized water. They were dried in an oven at 80 °C. To start a reaction, 158.4 ml of J.T. Baker ethylene glycol (EG) was added to a 500 ml flask, and this flask was stoppered and placed in an oil bath set to 140 °C. Four solutions were then prepared: (1) 0.257 g of NaCl in 20 ml EG, (2) 0.081 g $Fe(NO_3)_3$ in 10 ml EG, (3) 1.05 g polyvinylpyrrolidone (55,000 MW) in 25 ml EG, and (4) 1.05 g $AgNO_3$ in 25 ml EG. After preheating the EG in the oil bath for 1 hour, 0.2 ml of solution (1), 0.1 ml of solution (2), 20.76 ml of solution (3), and 20.76 ml of solution (4) were added to the flask in that order with a single addition from a pipette, with about 30 seconds between the addition of each solution (the time between additions is not critical). The flask was

stoppered and allowed to react for 2 hours. The wire solution was then distributed evenly into 6 centrifugation tubes each with 10 ml of acetone. The tubes were vortexed and then centrifuged for 1 hour at 2000 rpm. The supernatant was removed down to the 5 mL level, and the wires were re-dispersed in DI water before another round of centrifugation for 1 hour at 2000 rpm. The wires were washed with DI water in the same way one additional time before use. Wire solution concentration was determined using atomic absorption spectroscopy.

5.2.2. Fabrication of Silver Nanowires Films

Ag NW films were fabricated by spraying an aqueous solution of Ag NWs onto a surface, followed by pressing. The wire solution was diluted to 800 ppm of Ag with DI water. A microscope glass slide was cut into 1 inch squares and plasma cleaned in a Harrick Plasma Cleaner/Sterilizer (Model PDC) for 5 minutes. The squares were preheated on a heating pad covered by aluminum foil for 5 minutes at 130 °C. Temperature was controlled with a Staco Energy Type 3-PN-1010 Variable Autotransformer. The spray rate was set to between .05 and .09 ml/s. Spraying was performed in a laboratory hood with an Aztek A470 Airbrush with a 0.4 mm nozzle attached to a Sun Mines Electrics mini air compressor. The spray gun was moved back and forth across the slides from a height of several inches. It was important that the temperature of the heating pad did not drop below 100 °C during the spraying process. The conductivity of the slides was measured by a Signatone S-1160A-5 four -point probe every 2 minutes. Spraying continued until the average conductivities of all slides were below 50 Ω/□. The percent transmittance of each slide was measured at 550 nm using a Cary 6000i UV-Vis-NIR spectrophotometer.

The same procedure was used with the polyethylene terephthalate (PET) film as the substrate. The material was cut into 1 inch by 3 inch strips and plasma cleaned for 5 minutes. The strips were then taped to a large glass slide for the spraying and conductivity measurements to ensure they were not blown away by the spray gun, and to obtain good contact with the four-point probe.

The glass slides were pressed between aluminum plates using a Model C Carver Laboratory Press. The slides were placed on an aluminum plate with the wires facing up, and then a clean microscope slide was carefully placed on the wires before setting the other plate on top. The slides were pressed with 1 metric ton of pressure. The same pressing procedure was used with the PET slides, but the clean microscope slides were fluorinated before pressing to reduce the amount of nanowire transfer from the polyethylene terephthalate to the glass. To fluorinate the microscope slides, they were plasma cleaned for 1 minute, and then placed in a desiccator under vacuum with 50 μL of 1H, 1H, 2H, 2H-perfluorooctyltriethoxysilane (98%, Sigma-Aldrich, Product Code 667420) for at least one day before pressing.

5.2.3. Polymer Solar Cell Fabrication and Testing

Prior to use, the ITO substrates were ultrasonicated for 20 minutes in acetone followed by deionized water and then 2-propanol. The ITO substrates were dried under a stream of nitrogen and subjected to the treatment of UV-Ozone over 30 minutes. No further treatment was applied to Ag NW substrates before using. A filtered dispersion of PEDOT:PSS in water (Baytron PH500) was then spun cast onto clean ITO and Ag NW substrates at 4000 rpm for 60 seconds and then baked at 140 °C for 10 minutes to give a thin film with a thickness of 40 nm. Blends of polymer and $PC_{61}BM$ were dissolved in

corresponding solvents with heating at 120 °C for 6 hours. All the solutions were spun cast at 400 rpm for 30 seconds onto the PEDOT:PSS layer. The substrates were then dried at room temperature in the glovebox under a nitrogen atmosphere for 12 hours. The devices were finished for measurement after thermal deposition of a 30 nm film of calcium and a 70 nm aluminum film as the cathode at a pressure of $\sim 2 \times 10^{-6}$ mbar. There are 8 devices per substrate, with an active area of 12 mm^2 per device. Device characterization was carried out under AM 1.5G irradiation with an intensity of 100 mW/cm^2 (Oriel 91160, 300 W) calibrated by a NREL certified standard silicon cell. Current versus potential (I-V) curves were recorded with a Keithley 2400 digital source meter. EQE were detected under monochromatic illumination (*Oriel Cornerstone* 260 ¼ m monochromator equipped with Oriel 70613NS QTH lamp) and the calibration of the incident light was performed with a monocrystalline silicon diode. All fabrication and characterization steps after adding the PEDOT:PSS layer onto ITO and Ag NW substrates were performed in gloveboxes under a nitrogen atmosphere. For more experimental details about reagents, instrumentation, and spectroscopy please check **Appendix A**.

5.3. Properties of Silver Nanowire Films

Fig. 5.2a presents a scanning electron microscopy (SEM) image of a flattened Ag NW film on a glass substrate fabricated by spraying a solution of nanowires, followed by pressing. A high-magnification image in the inset shows the Ag NWs appear to be squashed. The NWs used for the electrode were about 60 nm in diameter and 20 μm in length. This Ag NW film appears to have a lower density compared with films of a

similar conductivity (~36 Ω/□) in a previous report.[74] This is likely due to the fact that

the NWs used here are longer (over 20 μm) than those used previously (~ 20 μm). As the

number density of NWs required for percolation is inversely proportional to L^2, where L

is the length of a NW, the longer NWs used here can achieve the same conductivity as the

shorter NWs at a number density 4 times smaller than that necessary for the shorter

NWs.[138]
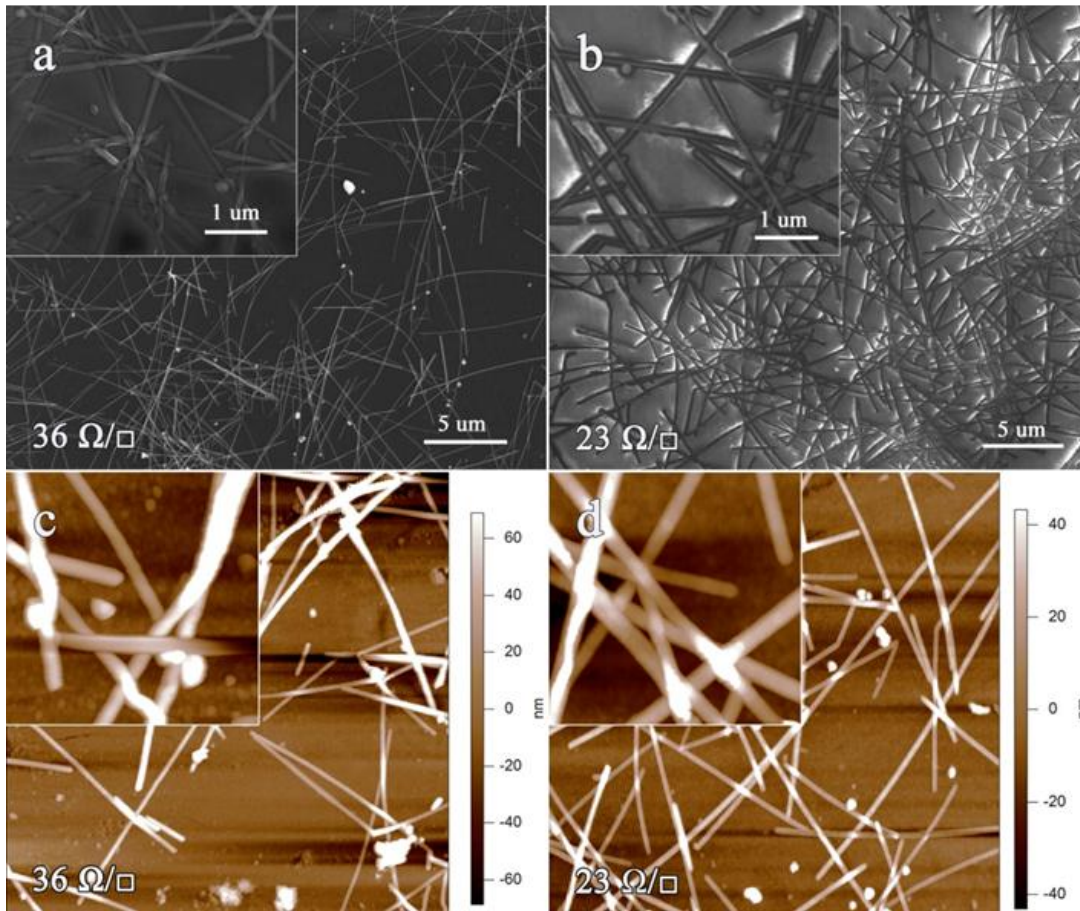
Figure 5.2. SEM images of Ag NW network a) before and b) after PEDOT:PSS coating; AFM images (10 × 10 μm; inset 2 × 2 μm) of the Ag NW network b) before and c) after PEDOT:PSS coating.

As shown in Fig. 5.2b, a uniform film of PEDOT:PSS can be spin-coated onto the Ag

NWs without washing away the NWs. The PEDOT:PSS coating decreases the sheet

resistance of the NW film from 36 Ω/□ to 23 Ω/□, which is very close to that of the

commercial ITO (~ 15 $\Omega/\square$) with similar transmittance in the visible region. It has previously been noted that the resistance at NW junctions is larger than that of individual Ag NWs.[72,74] The PEDOT:PSS coating likely decreases the resistance of junctions between the NWs, and thereby increases the overall conductivity of the film. Additionally, this PEDOT:PSS coating reduces the surface roughness of the Ag NWs from 100 ~ 120 nm in height (twice large as the diameter of Ag NWs due to their overlap) to ~ 80 nm, since the nanowires are partially embedded into the PEDOT:PSS coating (Fig. 5.2c and d). This reduced roughness decreases the possibility of an electrical short[65] caused by protruding Ag NWs.
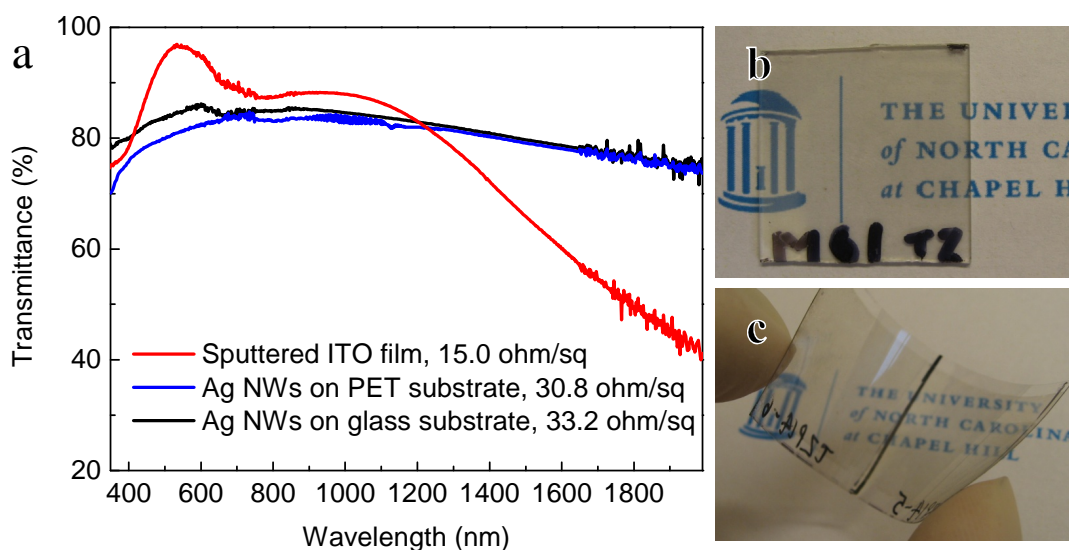
Figure 5.3. a) Transmission spectra for ITO reference, Ag NW films on glass and on PET; Photographs of highly transparent Ag NW films transferred onto b) glass and c) PET.

High optical transmittance over a large wavelength range from 400 to 2000 nm is an important property for the transparent electrode in a polymer BHJ solar cell, since one must minimize any optical loss due to the transparent electrode. Fig. 5.3a compares the optical transmittance of Ag NW films on glass and on PET substrates, with that of an ITO-coated reference substrate. Both of the Ag NW films (either on glass or PET)

exhibit excellent transparency (~ 80%) from 400 to 2000 nm. For example, the optical transmittance of the Ag NW film (33.2 Ω/□) on glass decreases slightly from 83.9 % at 500 nm, to 74.0 % at 2000 nm. The Ag NW film on PET exhibits a slightly lower transmittance compared with the Ag NW film on glass, but this is compensated for by its slightly lower sheet resistance (30.8 Ω/□), indicating the transmittance to sheet resistance ratio is similar for Ag NWs on either substrate. On the other hand, the optical transmittance of the ITO-coated substrate peaks (96.2 %) around 550 nm, but decreases to 42.1 % at 2000 nm. Thus, while ITO substrates might be slightly advantageous for applications targeting the visible region, Ag NW electrodes outperform ITO for applications requiring optical transparency extending into longer wavelength (e.g., solar cells and photodetectors).
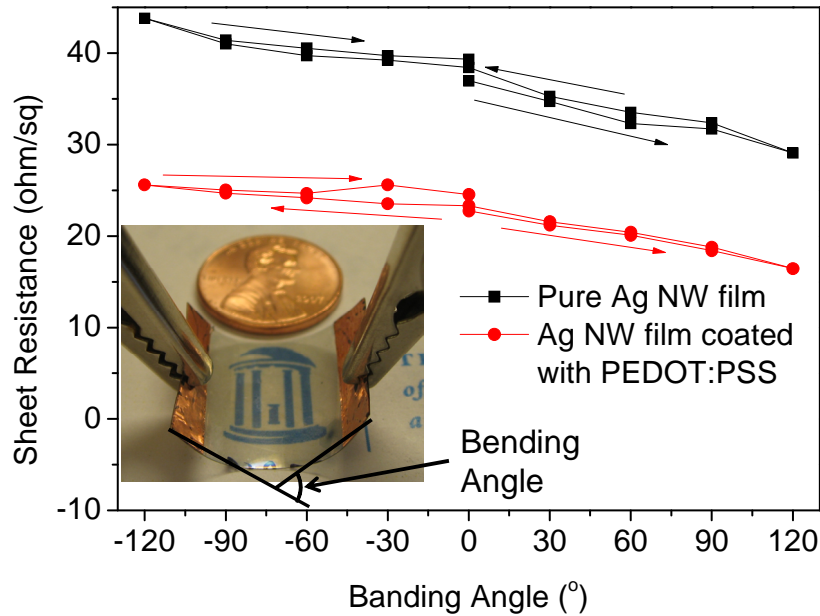
Figure 5.4. Sheet resistance of the pure Ag NW and PEDOT:PSS coated Ag NW films on PET substrates under different bending conditions. Inset shows the experimental setup of the two-probe electrical measurement. Direct contact of alligator clips to copper tape electrodes on Ag NW films was used in order to ensure good electrical contact during bending.

In addition to high optical transparency on par with ITO electrodes, Ag NW electrodes offer excellent mechanical flexibility while maintaining high conductivity, a significant advantage over traditional ITO electrode that will crack under a large degree of bending.[68] Fig. 5.4 shows the electrical conductivity of Ag NW films on PET with or without PEDOT:PSS coating while bending the substrate. For concave bending angles (curvature radii) up to 120° (5.7 mm), a slight decrease in the resistance of the Ag NWs/PET film with increased bending angle was observed. In contrast, the resistance of the Ag NWs/PET film slightly increases with decreased bending angle from 120° to – 120°. This change in resistance with bending angle may be due to the change in pressure at the nanowire junctions, or a change in the number of nanowire junctions in given area. More importantly, the original conductivity of the Ag NW film can be fully recovered once the strain is released from the Ag NWs/PET film, even after bending to 120° (5.7 mm in curvature radii) over one hundred times. Similar results were observed for the Ag NWs/PET film coated with PEDOT:PSS. The mechanical flexibility and recoverable conductivity of these Ag NW electrodes not only makes them compatible with low cost, roll-to-roll manufacturing, but also helps them find promising applications in emerging technologies (such as foldable displays or flexible solar cells) in which the electrode must withstand mechanical deformation without a loss in the conductivity.

5.4. Performance of BHJ Solar Cells Based on Silver Nanowires

In order to comprehensively investigate the application of these Ag NW electrodes as the anode in solution-processed BHJ polymer solar cells, we selected a set of three representative polymers. The first one is the well-studied and commercially available P3HT, widely used as a donor polymer in BHJ OPVs.[18] The other polymers (PBnDT-

FTAZ[28] and PBnDT-DTffBT[30]) were recently synthesized following the weak donor-strong acceptor strategy,[96,97] by alternating benzo[1,2-*b*:4,5-*b'*]dithiophene (BnDT) and either fluorinated 2-alkyl-benzo[*d*][1,2,3]triazoles (FTAZ) or 4,7-di(thiophen-2-yl)benzothiadiazole (DTffBT) (Fig. 5.5). This set of polymers represent a wide range of key materials properties and processing conditions: (a) energy levels and band gaps: the HOMO energy level is varied from – 5.2 eV in P3HT,[52] – 5.36 eV in PBnDT-FTAZ,[28] to – 5.54 eV in PBnDT-DTffBT[30] and the optical band gap from 1.9 eV in P3HT, 2.0 eV in PBnDT-FTAZ, to 1.7 eV in PBnDT-DTffBT; (b) processing condition: P3HT based BHJ cells were processed in chlorobenzene (CB) followed by thermal annealing at 150 °C to reach its maximum performance.[16] Devices based on the two amorphous donor polymers PBnDT-FTAZ and PBnDT-DTffBT were fabricated in 1,2,4-trichlorobenzene (TCB) and 1,2-dichlorobenzene (DCB), respectively, followed by a solvent annealing process. By comparing the properties of devices based on these three different polymers (in reference to the characteristics of devices based on ITO substrates), we aim to gain insights into the effect of the Ag NW electrode as the anode on the performance of solution-processed BHJ solar cells.
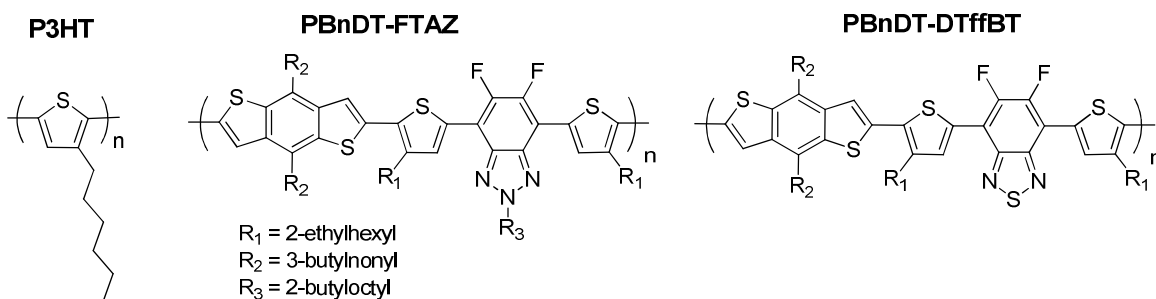
Figure. 5.5. Chemical structures of P3HT, PBnDT-FTAZ, and PBnDT-DTffBT.

A typical device consists of Ag NWs/PEDOT:PSS (40 nm) as the anode, polymer:PC$_{61}$BM as the active layer, and Ca (30 nm)/Al (70 nm) as the cathode. The

cross-section SEM images (Fig. 5.6a, b and c) clearly show the flattened Ag NWs were covered by the polymer/$PC_{61}BM$ active layer. The PEDOT:PSS layer was difficult to observe in the cross-section images, since it is relatively thin compared to the Ag NW film. We found it was necessary to use thick active layers (~ 300 nm) in order to prevent the Ag NWs from penetrating the device and causing a short circuit. Fortunately, unlike other high performance polymers with an optimized thickness around ~100 nm,[111] the polymers used in this study perform well with thicker films. For example the PBnDT-FTAZ and PBnDT-DTffBT polymers exhibit an optimized thickness over 200 nm.[28,30] For comparison, reference devices with identical polymer:$PC_{61}BM$ blends were fabricated on the conventional ITO anode with identical processing parameters in order to control for factors such as active layer thickness. As shown in Fig. 5.6d, the thickness (~ 300 nm) of the ITO reference device based on PBnDT-DTffBT is nearly identical to that of the device fabricated with the Ag NW electrode (Fig. 5.6c). Therefore any observed difference in the performance of the otherwise identical solar cells can be safely ascribed to the difference in the properties of Ag NW and ITO electrodes.
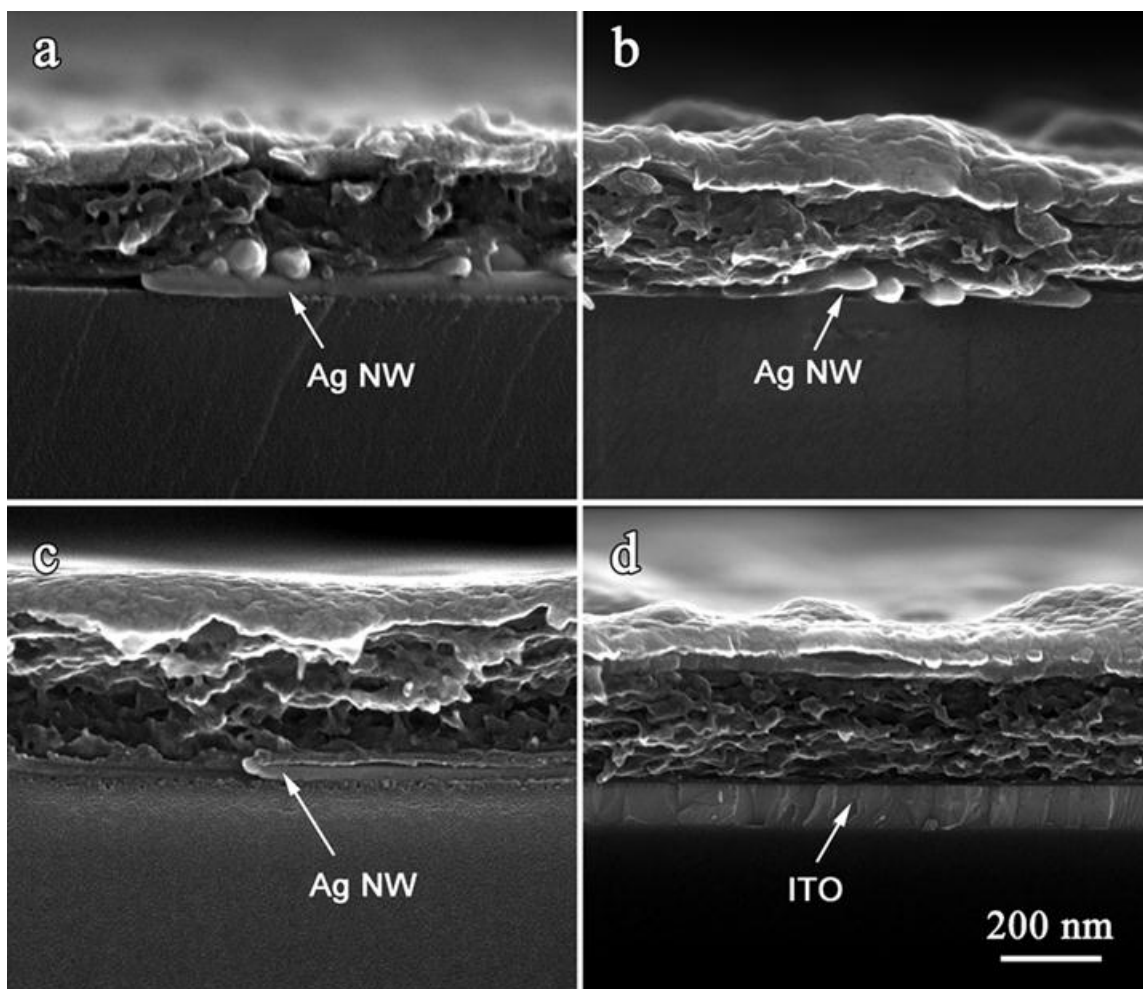
Figure 5.6. Cross-sectional SEM images of Ag NW-based devices made with a) P3HT, b) PBnDT-FTAZ, and c) PBnDT-DTffBT; d) ITO-based reference device based on PBnDT-DTffBT.
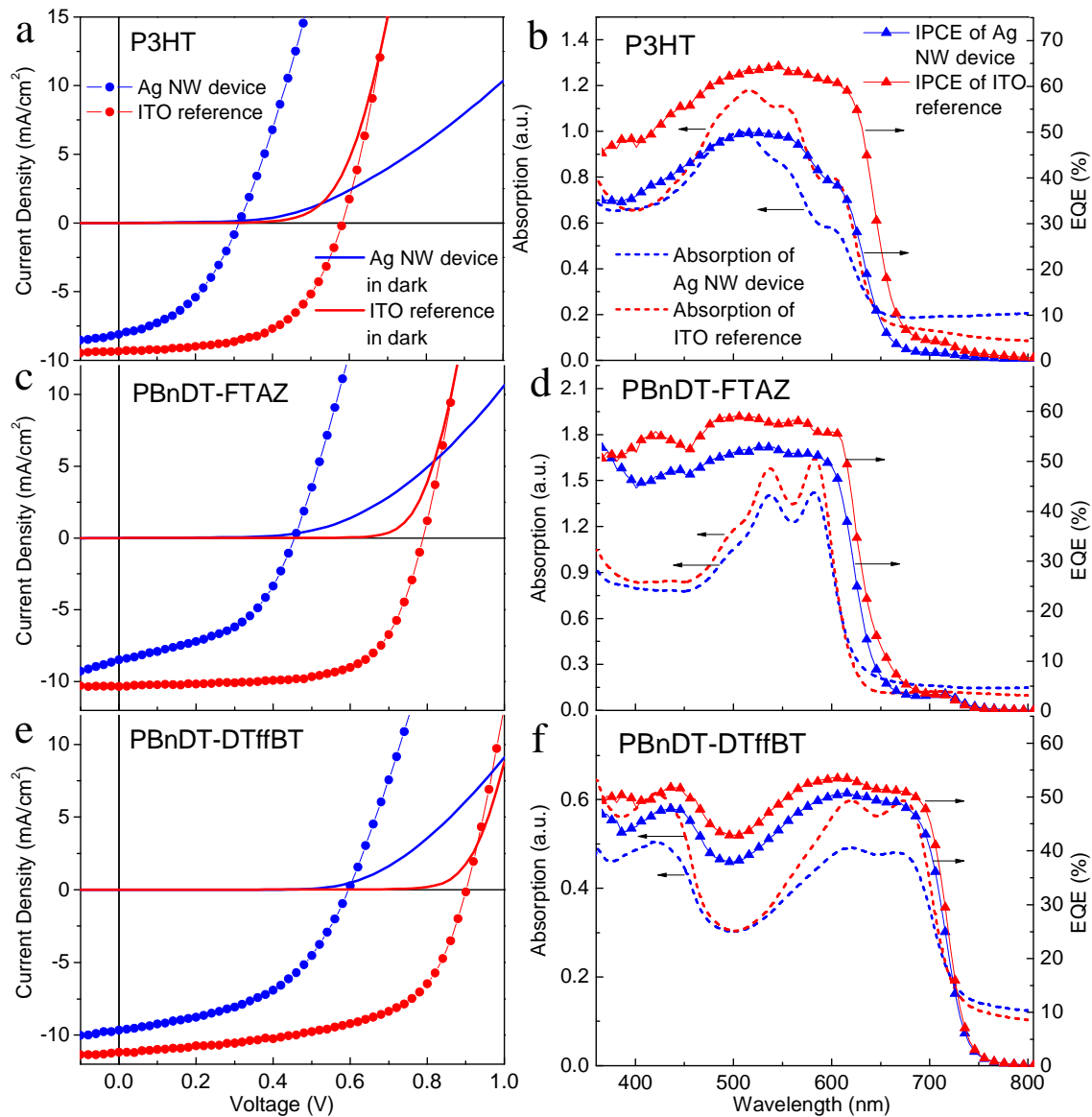
Figure 5.7. Characteristic *J-V* curves of the BHJ solar cell devices based on a) P3HT, c) PBnDT-FTAZ, and e) PBnDT-DTffBT under one Sun condition (100 mW/cm²); EQE and absorption of the BHJ solar cell devices based on b) P3HT, d) PBnDT-FTAZ, and f) PBnDT-DTffBT.

Representative current-voltage curves of devices under both illumination and dark are shown in Fig. 5.7, with key photovoltaic characteristics and processing conditions summarized in Table 5.1. The series resistance (R_s) and shunt resistance (R_{sh}) were calculated from the slope of the dark current curves. In general, all devices fabricated

with Ag NW electrodes demonstrate lower performance than their counterparts based on ITO electrodes, with a slightly smaller short circuit current (J_{sc}) and significantly lower fill factor (*FF*) and open circuit voltage (V_{oc}). We ascribe the reduced J_{sc} and *FF* to the decreased R_{sh} and increased R_s in devices based on Ag NW electrodes. In general, both a high R_{sh} and a low R_s are desirable for any solar cell. Compared with the reference devices with conventional ITO anodes, there is a noticeable decrease in the R_{sh} of all devices based on Ag NW electrodes, but still large enough for use in OPVs. On the other hand, the R_s of the Ag NW-based devices is significantly greater than that of the ITO-based device, which is likely the main reason for a 10 % decrease in J_{sc} of the device based on Ag NW electrodes when compared with the reference device based on ITO electrodes. Although the conductivity of Ag NW electrodes is comparable with that of ITO, these Ag NW networks are not as continuous and smooth as the sputtered ITO thin film, thereby resulting in more conduction taking place through the polymer in the device based on Ag NWs. This fact could explain the increased R_s in the Ag NW-based devices. Taken together, the larger R_s and lower R_{sh}, lead to a 20 % decrease in the *FF* for the Ag NW-based solar cells.

Table 5.1. Fabrication parameters and photovoltaic performances of devices.[a]

Polymer	Polymer: $PC_{61}BM$	Solvent	J_{sc} (mA/cm²)	V_{oc} (V)	FF (%)	η (%)	R_s (Ω)	R_{sh} (Ω)
P3HT (NWs)	1:1	CB	8.12	0.31	43	1.1	285	3.3×10^4
P3HT (Reference)	1:1	CB	9.22	0.58	57	3.1	29.3	2.0×10^5
PBnDT-FTAZ (NWs)	1:2	TCB	8.84	0.45	49	1.9	125	5.0×10^4
PBnDT-FTAZ (Reference)	1:2	TCB	10.33	0.79	67	5.5	32.3	2.5×10^5
PBnDT-DTffBT (NWs)	1:1	DCB	9.64	0.59	48	2.8	196	2.0×10^5
PBnDT-DTffBT (Reference)	1:1	DCB	11.17	0.91	58	5.8	29.6	1.0×10^6

[a] All polymer/$PC_{61}BM$ solutions were spun cast at 400 rpm for 30 seconds to obtain similar film thicknesses.

The primary reasons for the lower efficiency of all the devices based on Ag NWs is the significantly smaller V_{oc} compared with that of the ITO-based device. It is generally accepted that the V_{oc} of polymer/fullerene BHJ solar cells is primarily determined by the difference between the HOMO energy level of the polymer and the LUMO of the acceptor.[93,139,140] In our study, the V_{oc} of devices based on ITO electrodes traces the different HOMO energy levels of the polymers that were used (Table 5.1). However, we observed a consistent decrease of ~ 0.3 V for the Ag NW-based devices compared with their ITO-based counterparts, regardless of the HOMO energy level of the donor polymer. One plausible reason could be the change in the microstructure and intermolecular interaction in the polymer active layer when switching from ITO electrodes to Ag NW electrodes, which could affect the V_{oc}.[114] However, the absorbance and External quantum

efficiency (EQE) of the Ag NW-based devices exhibit nearly identical absorption edge and EQE curve shape compared with those of ITO reference devices of each polymer (Fig. 5.7b, d and f), indicating that the microstructure and intermolecular interaction in the polymer active layer was not strongly affected by the Ag NW electrode. Therefore, we are inclined to the alternative explanation that the observed difference in the V_{oc} between ITO based devices and Ag NW based devices could be due to the difference in the work function of these electrode materials (ITO, Ag NWs, and PEDOT:PSS), since a non-ohmic contact between the anode and the active layer (e.g., polymer) could diminish the V_{oc} of polymer solar cells.[139,141,142] To explore this hypothesis further, ultraviolet photoelectron spectroscopy (UPS) was performed to measure the work function (φ_m) of the Ag NW electrodes, the PEDOT:PSS and the ITO. The φ_m was calculated according to equation (5.1),[143]

$$\varphi_m = E_{min} + hv - E_{max} \qquad (5.1)$$

where, E_{min}, the low photoelectron kinetic energy, defines the lowest energy electrons able to overcome the work function of the surface; E_{max}, the high kinetic energy onset of the photocurrent, is a manifestation of the electron population around the Fermi level of the metal; and hv is a known energy provided to the electrons (21.2 eV in our experiment). As summarized in Table 5.2, due to the high work function of PEDOT:PSS, the φ_m of the ITO anode coated with PEDOT:PSS is 0.17 eV higher than that of the bare ITO anode. This thin PEDOT:PSS layer on top of ITO enhances the ohmic contact between the anode and the polymer, thereby improving the V_{oc} of BHJ devices. It proved difficult to determine the φ_m of the pure Ag NW film due to charges build-up on the insulating substrate, likely due to the low density of the Ag NWs. Thus the φ_m of a high-

density Ag NW film was measured instead (~ 4.04 eV) to estimate the φ_m of the pure Ag NW film. As we demonstrated earlier (Fig. 5.2d), a ~ 40 nm thin PEDOT:PSS layer cannot fully cover these Ag NW networks, therefore the φ_m of Ag NW electrode after coating PEDOT:PSS is only slightly increased to 4.19 eV, 0.39 eV lower than that of ITO coated with PEDOT:PSS electrode. The lower φ_m of the Ag NW electrode (even after coated with PEDOT:PSS), combined with its greater roughness, would very likely make the contact between the anode (Ag NWs) and the polymer less ohmic than that between the smooth films of ITO and the same polymer. Therefore the difference in the work function (0.39 eV) between Ag NWs/PEDOT:PSS and ITO/PEDOT:PSS can account for the observed roughly 0.3 V decrease of V_{oc} in all the Ag NW-based devices. Although the performance of Ag NW-based devices is currently lower than the ITO based reference devices, we still achieved a respectable power conversion efficiency of 2.8 %, including a high J_{sc} of 9.64 mA/cm^2, a V_{oc} of 0.59 V and a fill factor of 48% with the solution-processed BHJ solar cell based on the Ag NW anode and a novel polymer (PBnDT-DTffBT).

Table 5.2. Work function of anode electrodes [a]

Substrates	E_{min} (eV)	E_{max} (eV)	φ_m (eV)
ITO	9.41	26.2	4.41
ITO (coating PEDOT)	9.58	26.2	4.58
Ag NWs	9.04	26.2	4.04
Ag NWs on Glass (coated with PEDOT:PSS)	8.49	25.5	4.19
Ag NWs on PET (coated with PEDOT:PSS)	9.44	26.2	4.44

[a] Ultraviolet photoelectron spectrum are provided in **Appendix B3**.

5.5. Photovoltaic Properties of Flexible BHJ Solar Cells

A significant advantage of the Ag NWs over ITO is their excellent resilience to mechanical deformation with minimal loss of their conductivity and transparency (Fig. 5.4). To investigate the impact of flexion on the performance of solar cells based on these flexible electrodes, BHJ solar cells made from each of these three polymer:$PC_{61}BM$ blends as the active layer were fabricated on Ag NWs/PET films. The photovoltaic data of the flexible BHJ solar cells were acquired with two probe electrical measurements performed by the direct contact of an alligator clip to the Ca/Al cathode and to the copper tape covered Ag NW anode, respectively. The copper tape between the alligator clip and the Ag NW anode was used in order to ensure good electrical contact during the measurement (Fig. 5.8). This setup allowed us to monitor the change in photovoltaic properties of flexible solar cells as a function of the bending angle without detaching and

repositioning the electrical contacts. Unfortunately, solar cells using P3HT/PC$_{61}$BM as an active layer always exhibited the characteristics of a short circuit, even when fabricated with thicker polymer layers. This is likely due to the fact that the annealing process for P3HT:PC$_{61}$BM cells takes place at 150 °C, a temperature much higher than the glass transition temperature (T_g) of PET (75 °C), which would cause the PET substrate to deform. The deformation of the PET substrate would in turn increase the likelihood of Ag NWs penetrating the active layer. Devices made with the amorphous donor polymers PBnDT-FTAZ and PBnDT-DTffBT did not require annealing, so these devices were successfully fabricated.
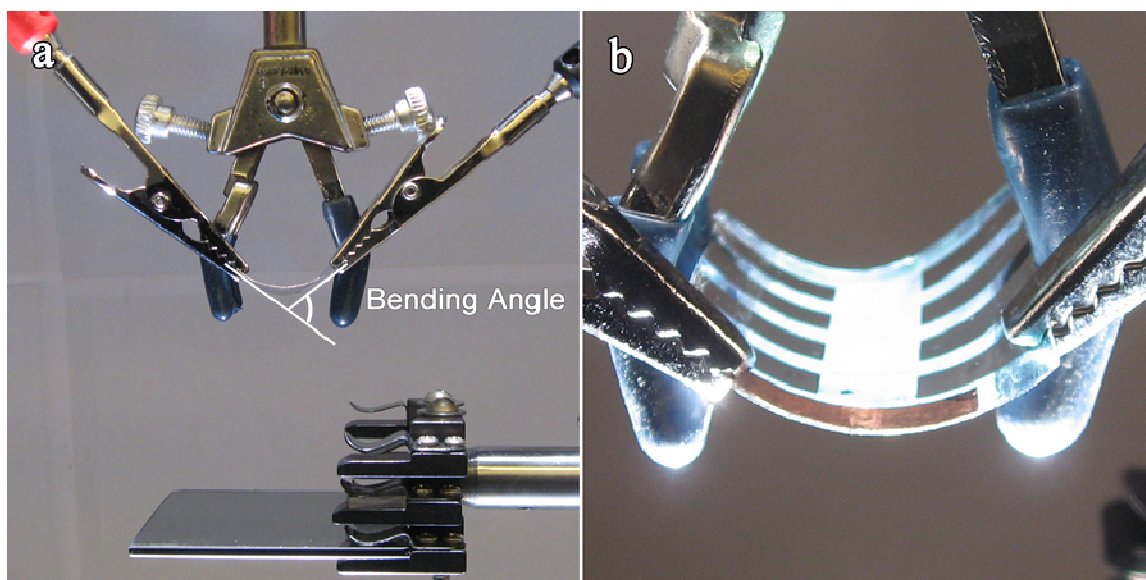
Figure 5.8. a) The experimental setup used for measuring the *J-V* curves of flexible devices. b) Direct contact of alligator clips to copper tape on the Ag NW anode was used in order to ensure good electrical contact during the bending.

The current-voltage characteristics of Ag NWs/PET-based flexible solar cells made with either PBnDT-FTAZ or PBnDT-DTffBT under different bending conditions are shown in Fig. 5.9a and b, respectively. Representative performance parameters of solar cells are tabulated in Table 5.3. Compared with the devices fabricated on Ag NWs/glass substrates, there is a noticeable decrease in J_{sc} for both of the flexible solar cells, which

perhaps resulted from the technical challenge of achieving a uniform coating of the active layer on top of Ag NWs/PET via spin coating, since these flexible PET substrates are prone to deformation. Interestingly, the V_{oc} of PBnDT-FTAZ and PBnDT-DTffBT based flexible devices improves from 0.45 V to 0.67 V and from 0.59 V to 0.75 V, respectively. This large improvement of V_{oc} (~ 0.2 V) is likely due to a higher work function of the PEDOT:PSS/Ag NWs/PET film (~ 0.25 eV higher) compared with the PEDOT:PSS/Ag NWs/Glass substrate (Table 5.2); however, the exact nature of the observed higher work function of the PEDOT:PSS/Ag NWs/PET film is not yet clear.
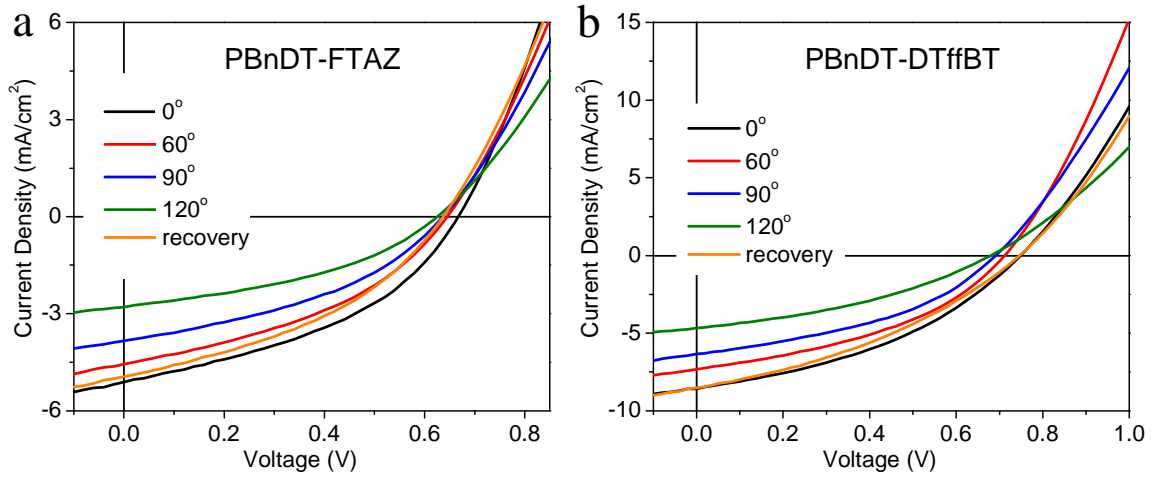
Figure 5.9. Characteristic *J-V* curves of flexible devices during bending.

As shown in Fig. 5.9 and Table 5.3, with increased bending angle, the current density drops for both of the flexible Ag NWs/PET devices, which is likely due to the decreased angle of incidence of the illumination. The V_{oc} also decreased slightly under bending, which can be explained by equation (5.2),[98,114]

$$V_{oc} \approx \frac{nkT}{q} \ln\left(\frac{J_{sc}}{J_{so}}\right) + \frac{\Delta E_{DA}}{2q}$$

(5.2)

106

where, n is the diode ideality factor, J_{so} is related to intermolecular interaction, and ΔE_{DA} is the energy difference between the LUMO level of the $PC_{61}BM$ and the HOMO level of the donor polymer. Since n, J_{so}, and ΔE_{DA} remain unchanged for devices based on the identical polymer/$PC_{61}BM$ blend, a smaller J_{sc} for an increased bending angle would slightly diminish the V_{oc} of the flexible device. There is no noticeable change on the FF under bending, implying that the R_s and R_{sh} of the devices barely change while varying the bending angle. This observation is consistent with the minimal change of the conductivity of these Ag NW electrodes as shown in Fig. 5.4. More importantly, even after 10 convex bending–recovery cycles with significantly large deformation (e.g., a bending angle/curvature radii of 120°/7.2 mm), these flexible devices can still recover their original performance with only little performance degradation. For example, we achieved an efficiency of 2.3 % for the PBnDT-DTffBT/$PC_{61}BM$ based flexible devices even after these devices were bent to 120° (7.2 mm) and returned to 0°, 90% of the original value (2.5 %) before bending. In sharp contrast, BHJ devices based on ITO/PET only withstood bending to curvature radii of 15.9 mm with poor performance. Further, these devices failed completely (becoming an open circuit) after being bent to curvature radii of 9.5 mm due to the development of micro-cracks generated by the mechanical stress in ITO.[68] These results clearly exhibit the superiority of these Ag NWs over ITO in fabricating highly flexible solar cells with high efficiency.

Table 5.3. Photovoltaic performances of flexible devices under bending condition.

Polymer	Bending Angle (°)/ Curvature Radii (mm)	J_{sc} (mA/cm^2)	V_{oc} (V)	FF (%)	η (%)
PBnDT-FTAZ	0/-	5.11	0.67	40.77	1.4
	60/14	4.56	0.65	39.25	1.2
	90/9.5	3.84	0.63	40.11	1.0
	120/7.2	3.79	0.63	39.17	0.69
	recover	4.95	0.63	39.45	1.2
PBnDT-DTffBT	0/-	8.58	0.75	38.72	2.5
	60/14	7.33	0.71	40.37	2.1
	90/9.5	6.35	0.69	40.57	1.8
	120/7.2	4.68	0.69	36.05	1.2
	recover	8.52	0.75	35.58	2.3

5.6. Conclusion

Fully solution-processed polymer BHJ solar cells with Ag NW anodes have been fabricated with three representative donor polymers (P3HT, PBnDT-FTAZ, and PBnDT-DTffBT). Comparison of these devices with reference devices based on ITO revealed several unique characteristics of Ag NW anodes when they are paired with different polymers. As Ag NW electrodes offer electrical and optical properties comparable to those of ITO, the short circuit current was not strongly affected by the type of anode that was used. In contrast, the open circuit voltage of Ag NW-based BHJ devices is consistently ~ 0.3 V lower than that of corresponding ITO-based devices, which significantly reduced the observed efficiency of the Ag NW-based devices. This lower open circuit voltage is ascribed to the low work function of the Ag NWs/PEDOT:PSS film and the poor ohmic contact between the Ag NW anode and the active layer. Future work will focus on engineering the nanowire anode to improve the work function

matching. However, even with this relatively low open circuit voltage, devices on glass substrates exhibited efficiencies as high as 2.8 %. Further, we demonstrated for the first time that highly flexible BHJ solar cells can be fabricated on Ag NWs/PET anode via a simple solution processing, the flexible devices retained an efficiency of 2.3 %, even after 10 convex bending–recovery cycles with large deformation up to 120° (7.2 mm in curvature radii), whereas devices based on ITO/PET exhibited an open circuit after being bent to 9.5 mm in curvature radii. This study demonstrates that the Ag NW electrode meets the most important criteria of conductivity, transparency, flexibility, and solution-processability necessary to replace ITO in organic photovoltaics. Such nanowire electrodes will likely enable high-throughput roll-to-roll manufacturing of low-cost OPVs.

CHAPTER 6

PARALLEL BULK HETEROJUNCTION POLYMER SOLAR CELLS [*]

6.1. Introduction

In a typical BHJ polymer solar cell which employs a conjugated polymer as a p-type semiconductor and a fullerene derivative as the n-type semiconductor, the polymer is the major light absorber. However, the intrinsic narrow absorption width of these conjugated polymers, usually with a full width at half maximum (FWHM) on the order of 200 nm,[77] can only overlap with a small fraction of the solar spectrum. This in-efficient light absorption leads to noticeably low current (usually around 10 mA/cm^2) when compared with other types of high efficiency solar cells (e.g., over 40 mA/cm^2 in crystalline Si solar cell), which limits the further improvement on the efficiency of polymer solar cells. Therefore, intensive research efforts have been devoted to the development of new p-type conjugated polymers with better match to the solar spectrum, and the pursuit of non-fullerene based n-type materials that absorb complimentary region of the solar spectrum.[144] Unfortunately, only incremental progress has been made in both fronts.

Alternatively, one can increase the absorption breadth of a solar cell by stacking multiple sub-cells in either series or parallel connection such that each sub-cell incorporating a polymer absorbing specific range of the solar spectrum (Fig. 6.1). Specifically, a serially connected tandem cell benefits from a significantly higher V_{oc},

which is the sum of those from each sub-cell; however, the J_{sc} of such a device is pinned to the smallest J_{sc} among those individual J_{sc} from sub-cells.[84] This poses the first technical challenge: each sub-cell must be carefully engineered (e.g., control of the light absorbing layer thickness) to ensure the current matching with maximum possible value. Second, instead of dealing a sandwiched structure of electrode/active layer/electrode with two interfaces (between electrode and active layer) in a single junction BHJ solar cell, one has to carefully design and optimize additional intercellular recombination layers between the sub-cells. These recombination layers not only create more interfaces which need to be optimized to reach the designed efficiency, also reduce the amount of transmitted light, let alone the added cost of fabrication. On the other hand, the J_{sc} in a parallel connected tandem cell combines those from each sub-cell, whereas the V_{oc} is in between those of single sub-cells.[85-88] However, even worse than the serially connected tandem cell, the parallel connection employs not only more intercellular electrodes, also requires additional optical spacers to separate these BHJ sub-cells (Fig. 6.1),[85] both of which create a number of technical difficulties and increase the cost of fabrication.

Recently, Zhang et al. fabricated a simple parallel tandem cell by spin coating P3HT/ $PC_{61}BM$ solution directly onto a pre-evaporated copper phthalocyanine (CuPc) layer.[87] In this simple parallel tandem cell, the $PC_{61}BM$ in the top P3HT/$PC_{61}BM$ bulk heterojunction (BHJ) sub-cell is believed to be in contact with the underlying CuPc to form the CuPc/$PC_{61}BM$ bilayer sub-cell. Unfortunately, limited by the low current generated from the CuPc/$PC_{61}BM$ bilayer solar cell, no noticeable improvement in the overall efficiency was observed in this simple design of parallel tandem cell. Most importantly, the fabrication of this parallel tandem structure took advantage of the solvent

resistance of the evaporated CuPc layer. Thus similar approaches cannot be directly applied to adding the top sub-cell via solution processing onto the solution-processed BHJ bottom sub-cell (Fig. 6.1), because the bottom sub-cell could be easily damaged by the solvent when spin coating the subsequent layers if no interfacial layer were used.
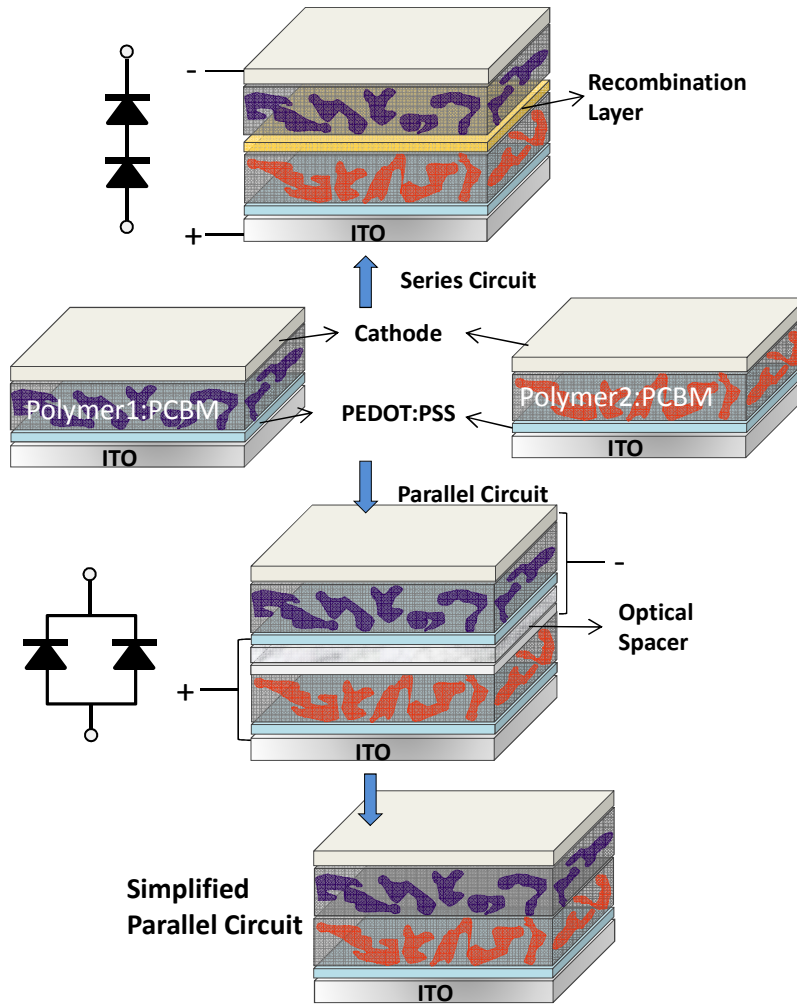
Figure 6.1. Schematic structure of different types of polymer tandem cells.

6.2. Concept of Parallel Bulk Heterojunction (PBHJ)

Our new design, parallel bulk heterojunction (PBHJ) solar cell, overcomes aforementioned technical challenges and increased cost associated with tandem cell,

since it maintains the fundamental structure of a single junction BHJ cell (two electrodes sandwiching the active layer) (Fig. 6.2). Meanwhile, PBHJ bears the advantage of conventional multi-blend systems – an increased absorption width. Importantly, compared with conventional multi-blend system which can only incorporate a small quantity of additional donor molecules/polymers as sensitizers, PBHJ solar cells can employ two or more polymers of different band gaps at any composition, regardless of their HOMO (or LUMO) levels. In our PBHJ device incorporating two donor polymers and $PC_{61}BM$ as the acceptor (*vide infra*), excitons generated in individual donor polymer would migrate to respective polymer/$PC_{61}BM$ interface and then dissociate into free electrons and holes, as would occur in a conventional BHJ cell. Electrons would transport through the $PC_{61}BM$ enriched domain prior to their collection by the cathode. Meanwhile, besides a possible charge transfer at the interface of polymer/polymer, holes generated from different donor polymers would mainly travel through their corresponding polymer linked channel to the anode. Thus, all free charge carriers generated from two donor polymers and $PC_{61}BM$ (i.e., two polymer/$PC_{61}BM$ blends) can be collected by the same cathode and anode, which indicates this structure is equivalent to a parallel connection of two single BHJ cells. PBHJ essentially merges two (or more) single junction cells into one integrated design that combines the simple device structure (and low fabrication cost) of single junction BHJ cells *and* the much improved light harvesting from tandem cells.
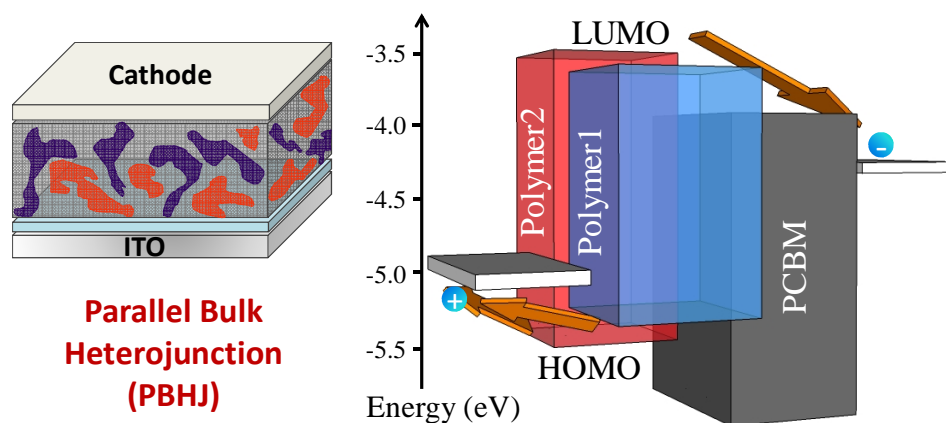
Figure 6.2. Schematic structure and energy diagram of PBHJ devices

6.3. Experimental Section

All devices were fabricated by spin-coating the active-layer blend solutions on top of electronic-grade PEDOT:PSS (Baytron PH500) coated indium tin oxide/glass slides (ITO) (Thin Film Devices). PBHJ solar cells were fabricated from one single blend of two donor polymers with $PC_{61}BM$, and single BHJ devices were fabricated from binary blends of donor polymer and $PC_{61}BM$. All blends were dissolved in dichlorobenzene (10 mg/mL for donor polymers) with heating at 100 °C for 6 hours. The devices were finished for the measurements after the thermal deposition of a 30 nm film of calcium and a 70 nm aluminum film as the cathode at a pressure of ~ 1×10^{-6} mbar. There are 8 devices per substrate, with an active area of 12 mm^2 per device. Device characterization was carried out under AM 1.5G irradiation with the intensity of 100 mW/cm^2 (Oriel 91160, 300 W) calibrated by a NREL certified standard silicon cell. Current versus potential (I-V) curves were recorded with a Keithley 2400 digital source meter. EQE were detected under monochromatic illumination (Oriel Cornerstone 260 ¼ m monochromator equipped with Oriel 70613NS QTH lamp) and the calibration of the incident light was performed with a monocrystalline silicon diode. All fabrication steps

after adding the PEDOT:PSS layer onto ITO substrate, and characterizations were performed in gloveboxes under nitrogen atmosphere. For more experimental details about reagents, instrumentation, and spectroscopy please check **Appendix A**.

6.4. Proof of PBHJ Concept

As the proof-of-concept, we chose two groups of polymers to construct PBHJ devices (poly(benzodithiophene-dithienyl-benzotriazole) (TAZ)[28] and poly(benzodithiophene-dithienyl-benzothiadiazole) (DTBT)[30]; poly(benzodithiophene-dithienyl-difluoro-benzothiadiazole) (DTffBT)[30] and poly(benzodithiophene-dithienyl-thiadiazolo-pyridine) (DTPyT)[111]). Each group contains two polymers of different band gaps and HOMO levels (Fig. 6.3). Two PBHJ devices were then fabricated with ~ 100 nm thick active layers consisting of TAZ/DTBT/PC$_{61}$BM (weight ratio of 0.5:0.5:1) and DTffBT/DTPyT/PC$_{61}$BM (weight ratio of 0.5:0.5:1) respectively. For the purpose of comparison, we also fabricated four conventional single junction BHJ sub-cells based on individual polymer blended with PC$_{61}$BM (1:1) with an active layer of ~ 50 nm thickness. The first notable feature is that the absorption spectra of these PBHJ cells are essentially the linear combination of spectra of two single sub-cells (Fig. 6.4a and b), since PBHJ cells have no interfacial layers that could undesirably reflect and absorb the incident light and thereby reduce the total amount of light absorbed by the active layer. Because two polymers of different band gaps and absorption behavior are employed, these PBHJ cells exhibit much broader absorption width when compared with that of the large band gap polymer based sub-cells, and significantly increased absorption strength in low wavelength regions than that of small band gap polymer based sub-cells. For example,

the peak absorption of TAZ/PC$_{61}$BM film is located between 500 and 600 nm with the absorption edge only extending to approximately 650 nm. On the other hand, the DTBT/PC$_{61}$BM film absorbs relatively weakly between 500-600 nm, but has a strong absorption band between 600–750 nm. The PBHJ device of TAZ/DTBT/PC$_{61}$BM captures absorption features of both sub-cells and results in a strong absorption covering a significantly wider range (350 nm to 750 nm) with much increased absorption intensity. Similar absorption features are also observed in the PBHJ device of DTffBT/DTPyT/PC$_{61}$BM.
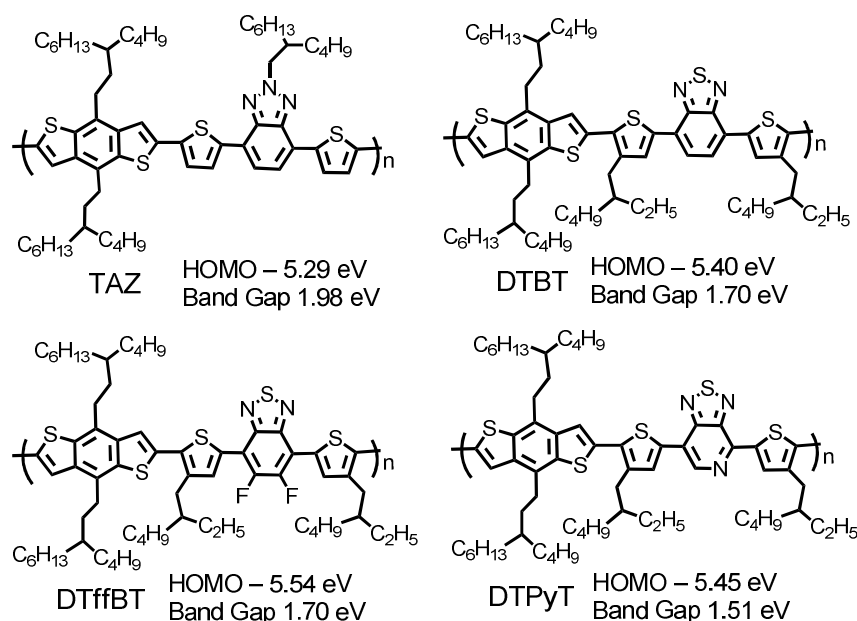
Figure 6.3. Chemical structures and band gaps of TAZ, DTBT, DTffBT and DTPyT.

The most interesting feature of these PBHJ devices is the external quantum efficiency (EQE) spectra. As shown in Fig. 6.4c and d, the EQE spectra of PBHJ devices are approximately the sum of those of individual "sub-cells" in the low wavelength range where both donor polymers contribute to *e-h* pairs (and thereby the photocurrent). This indicates that most of the free charge carriers generated in each "sub-cell" of the PBHJ device are successfully collected by respective electrodes. Interestingly, in high

116

wavelength range where the larger band gap polymer no longer absorbs photons and thereby contributes zero current, the EQE of the PBHJ device is higher than that of the lower band gap "sub-cell". For example, the EQE numbers of DTBT "sub-cell" and DTPyT "sub-cell" are around 30% at wavelength of 700 nm and 750 nm, respectively, whereas the EQE numbers of TAZ/DTBT and DTffBT/DTPyT based PBHJ cells are over 40 % at the corresponding wavelength. It is highly possible that the large band gap polymer with high mobility can serve as additional charge transport channel in the PBHJ device, to facilitate charge transport and consequently enhance the internal quantum efficiency (IQE) in the lower band gap absorption range. Collectively, much enhanced EQE spectra – over 40% across a width of over 400 nm – were observed in both of our PBHJ devices. As a result, the J_{sc} of PBHJ devices are significantly increased and almost identical to the sum of those in two single "sub-cells" (as shown in Fig. 6.4e and f). On the other hand, the V_{oc} of PBHJ devices is in between of those measured in individual "sub-cells", which establishes that PBHJ solar cells are different from conventional multi-blend systems where the observed V_{oc} is pinned to the smallest V_{oc} of the corresponding binary blends.[79,145] This is because in conventional multi-blend systems, dominant hole transport and collection occurs through the donor component with the highest HOMO level. This highest HOMO level determines the observed V_{oc} of the multi-blend system, independent of the origin of photocurrent generation.[79] However, in our PBHJ devices, both the energy transfer and charge transfer between different donor materials are not dominant. Holes generated from individual donor polymers would mainly travel through their corresponding polymer connected channel to the anode, similar to the parallel connection of two single junction BHJ cells. Thus the observed J_{sc}

117

combines those from each "sub-cell", whereas the V_{oc} is in between those of single "sub-cells", both of which are a clear indication of a parallel connection.[85-88]
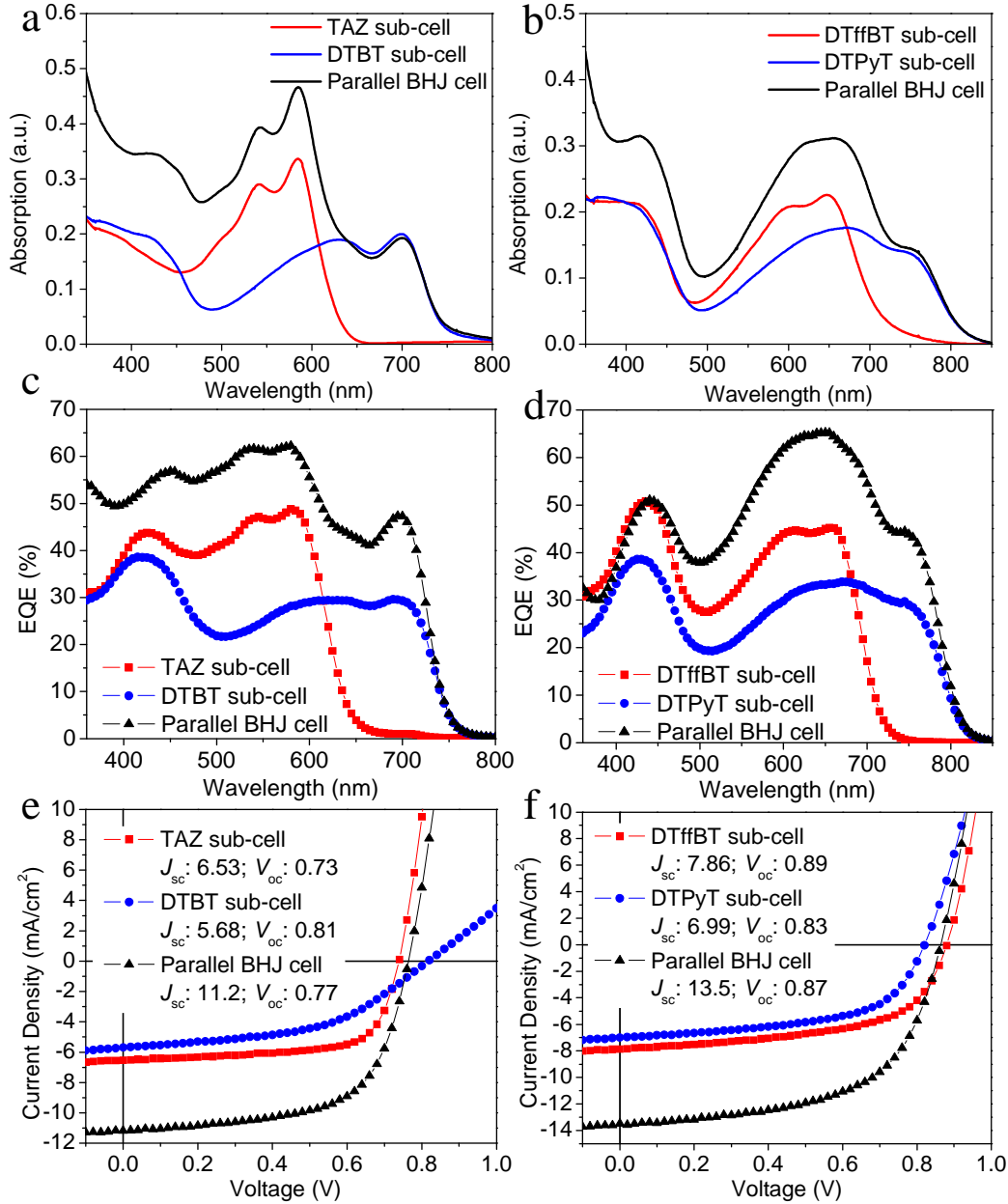
Figure 6.4. Absorption of the PBHJ devices and their sub-cells based on a) TAZ/DTBT and d) DTffBT/DTPyT; EQE of the PBHJ devices and their sub-cells based on b) TAZ/DTBT and e) DTffBT/DTPyT; Characteristic *J-V* curves of the PBHJ devices and their sub-cells based on c) TAZ/DTBT and f) DTffBT/DTPyT.

6.5. Photovoltaic Properties of PBHJ Solar Cells
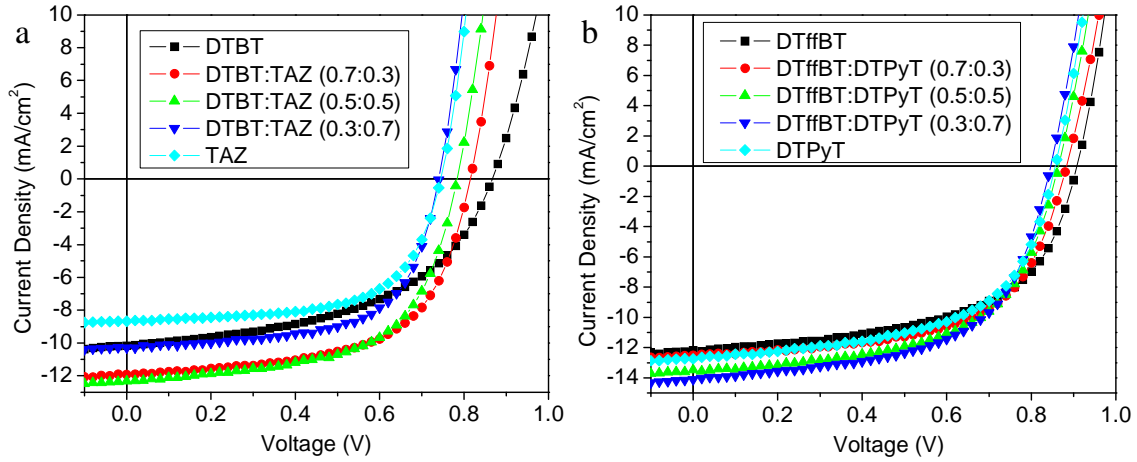
Figure 6.5. Characteristic J-V curves of the PBHJ devices and single BHJ cells with optimum thickness based on a) TAZ/DTBT and d) DTffBT/DTPyT.

In order to investigate the individual contribution from each sub-cell in the PBHJ device and identify the optimal device condition (e.g., blending ratio and film thickness), we varied the composition of related two sub-cells for each PBHJ device and also optimized the film thicknesses. Fig. 6.5 shows the J-V curves of the PBHJ devices based on various compositions of related two sub-cells, with the representative photovoltaic properties tabulated in Table 6.1. Fig. 6.6a and b summarize the EQE spectra of PBHJ devices consisting of systematically varied composition of two sub-cells, together with these of the single junction BHJ devices with optimal thickness for reference. In the PBHJ device based on TAZ/DTBT, as the proportion of TAZ sub-cell decreases, the EQE in the region between 450 and 600 nm attenuates (Fig. 6.6a). However, this does not lead to a decreased J_{sc} (Fig. 6.6c), since the correspondingly increased proportion of DTBT sub-cell results in an increased EQE response from 600 to 750 nm, which compensates the decrease of EQE in the low wavelength region.
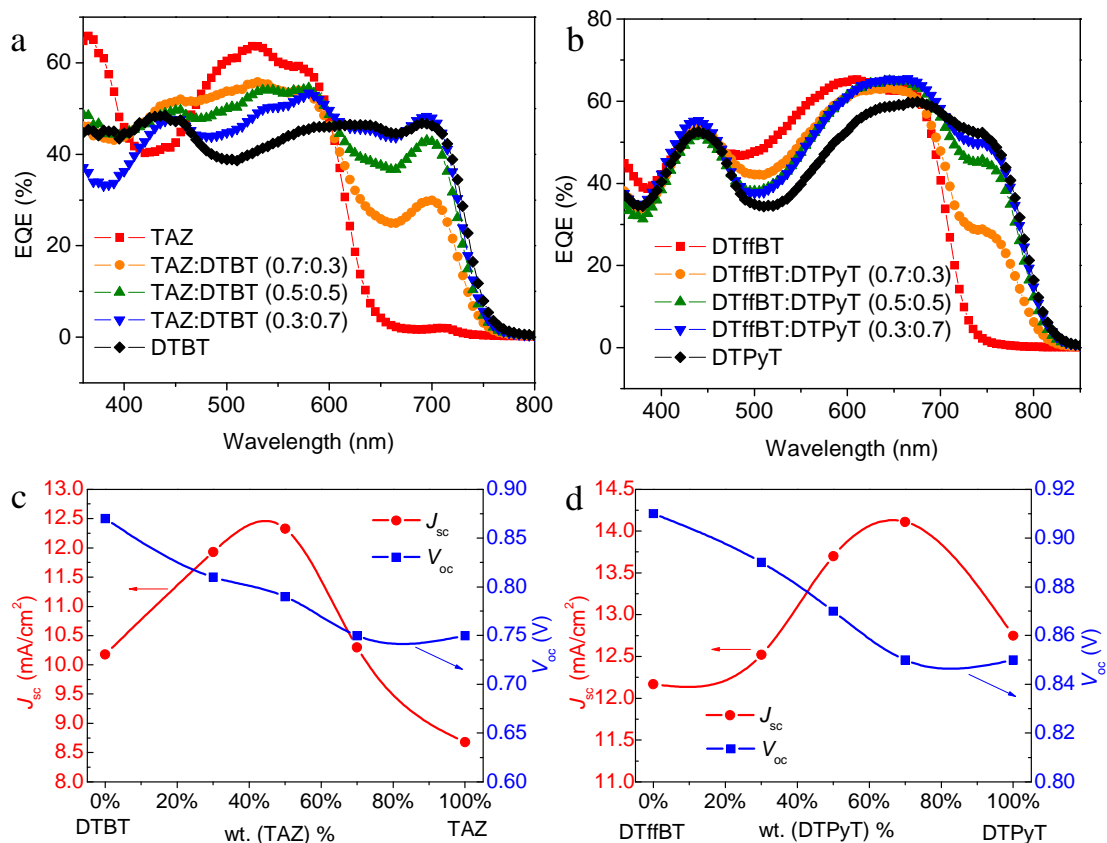
Figure 6.6. EQE of the PBHJ devices with different composition of a) TAZ/DTBT and b) DTffBT/DTPyT; J_{sc} and V_{oc} of the PBHJ devices as a function of the amount of c) TAZ in DTBT and d) DTffBT in DTPyT.

As a result, the J_{sc} in the PBHJ devices with all compositions (entry 2, 3, 4 in Table 6.1) has significantly improved when compared with single junction BHJ devices (entry 1 and 5 in Table 6.1). In particular, the PBHJ device consisting of equivalent amount of TAZ and DTBT sub-cells shows a J_{sc} of 12.3 mA/cm^2, which is about 40% and 20% higher than that of TAZ (8.68 mA/cm^2) and DTBT (10.2 mA/cm^2) based single junction BHJ devices, respectively. Similar composition-dependent behavior is also observed in the EQE spectra of PBHJ devices consisting of DTffBT and DTPyT based sub-cells (Fig. 6.6b), resulting in enhanced J_{sc} observed in all PBHJ cells (entry 7, 8, 9 in Table 6.1). The highest J_{sc} of the DTffBT/DTPyT based PBHJ solar cell is 14.1 mA/cm^2, about 16% and

10% higher than those of single BHJ devices based on DTffBT (12.2 mA/cm^2) and DTPyT (12.8 mA/cm^2), respectively. Interestingly, unlike the TAZ/DTBT based PBHJ cells where the highest J_{sc} appears at the 50:50 ratio, the highest J_{sc} in the DTffBT/DTPyT based PBHJ devices is achieved from the device consisting of 70% DTffBT and 30% DTPyT (Fig. 6.6d and entry 9 in Table 6.1), which indicates the optimum composition of a PBHJ device depends on the optical and electronic properties of constituting polymers, such as the overlap of EQE spectra of individual polymer based sub-cells. On the other hand, as the proportion of the sub-cell with higher V_{oc} increases, the V_{oc} of the related PBHJ solar cell shows a continuous improvement from 0.75 V to 0.87 V in the TAZ/DTBT system and 0.85 V to 0.91 V in the DTffBT/DTPyT system, respectively (Fig. 6.6c and d, Table 6.1). This further confirms that the PBHJ device belongs to the parallel connection of single junction sub-cells, since the voltage of a parallel circuit is the weighted average of individual voltages from these single sub-cells. Because of the much improved J_{sc}, all PBHJ devices (though with different compositions) exhibit increased overall efficiency when compared with corresponding single BHJ devices (Table 6.1). However, we note that the highest efficiency observed in these two exemplary PBHJ systems is not from the PBHJ device with highest J_{sc}, since the overall efficiency of solar cells is also affected by the V_{oc} and the *FF*. In these two specific PBHJ systems, the TAZ/DTBT PBHJ system exhibits the highest efficiency of 5.88% with a composition of 30% TAZ and 70% DTBT based sub-cells, whereas the DTffBT/DTPyT PBHJ system with equivalent proportion of DTffBT and DTPyT based sub-cells offers the best efficiency over 7%.

Table 6.1. Photovoltaic performances of devices with optimized thickness.[a]

Entry	Cells	Thickness (nm)	J_{sc} (mA/cm^2)	V_{oc} (V)	FF (%)	η (%)
1	TAZ:DTBT 1:0	96	8.68	0.75	62.4	4.06
2	TAZ:DTBT 0.7:0.3	102	10.3	0.75	62.0	4.79
3	TAZ:DTBT 0.5:0.5	111	12.3	0.79	59.8	5.80
4	TAZ:DTBT 0.3:0.7	79	11.9	0.81	60.8	5.88
5	TAZ:DTBT 0:1	88	10.2	0.87	49.6	4.39
6	DTffBT:DTPyT 1:0	138	12.2	0.91	56.5	6.26
7	DTffBT:DTPyT 0.7:0.3	84	12.5	0.89	59.3	6.60
8	DTffBT:DTPyT 0.5:0.5	94	13.7	0.87	58.9	7.02
9	DTffBT:DTPyT 0.3:0.7	81	14.1	0.85	56.5	6.78
10	DTffBT:DTPyT 0:1	89	12.8	0.85	58.1	6.30

[a] All polymers were blend with $PC_{61}BM$ at a weight ratio of 1:1 in dichlorobenzene.

6.5. Conclusion

A conceptually new device configuration, Parallel Bulk Heterojunction (PBHJ), was proposed and successfully demonstrated with two prototypical systems. PBHJ eliminates the needs of careful design and precise control of the interfacial layers, which are key components in conventional tandem cells, thereby significantly reducing the complexity of the devices and photon loss from these interfacial layers. More importantly, PBHJ enables the effective use of multiple sub-cells with much improved light absorption and conversion. Thus PBHJ represents a major advancement over the conventional parallel connected or series connected tandem cells. In the two prototypical systems, the J_{sc} of

PBHJ device can be increased up to 40% when compared with the optimum single BHJ devices, resulting in noticeably enhanced overall efficiency. Though detailed working mechanism and specific rationale in paring multiple polymers in PBHJ remain to be investigated, we believe PBHJ opens a new avenue to accelerate the efficiency improvement of polymer solar cells.

CHAPTER 7

CONCLUSION AND FUTURE DIRECTIONS

7.1. Importance of this Thesis

Further increasing efficiency and reducing the cost of manufacturing polymer solar cells are crucial for future commercialization of polymer solar cells. In previous chapters, some quantitatively investigations of side chains and substituents to construct ideal conjugated polymers for organic solar cells have been presented. With understanding the influence of side chains and substituents, highly efficient conjugated polymers for solar cells were successfully designed. Moreover, new interfacial layer and device structures of polymer solar cell demonstrated in previous chapters indicate that rational design of interface and structure not only facilities low cost roll-to-roll fabrication and stability, but also improve the performance of solar cells.

7.1.1 "Trivial" Things Are Non-Trivial

Conventional wisdom dictates that the band gap and energy levels of a conjugated polymer are primarily determined by the molecular structure of the conjugated backbone, while the solubilizing alkyl chains should have a negligible impact on these properties. Hence the side chains should have minimal impact on the J_{sc} and V_{oc} of corresponding polymer-based BHJ solar cells. However, contrary to the "conventional wisdom", we demonstrate in Chapter 2 that the side chain of a low band gap polymer (PNDT-DTBT) significantly impacts the observed V_{oc} and J_{sc} of the corresponding BHJ solar cell with

variations as much as 100%, depending upon the length and shape of these alkyl chains. The long and branched side chains would weaken the intermolecular interaction, which is beneficial to the V_{oc}. though at the expense of J_{sc}.   In chapter 3, we indicated a possible new strategy to increase efficiency of conjugated polymer-based solar cell via optimal combination of side chains and F substituents. Although long bulky side chains weaken π-π stacking and intermolecular interaction, thereby leading to reduced J_{sc} in the related polymer-based BHJ cells, the reduced J_{sc} is significantly improved by F substitution on the conjugated backbone, partly because of enhanced π-π stacking and optimized polymer orientation relative to the electrodes. Further, the introduction of F substituents lowers the HOMO and suppresses charge recombination, both of which benefit a higher V_{oc}. Finally, F substitution yields high charge separation probability even under very small external electric field, which not only leads to a very high *FF* over 60% in related BHJ devices, but also helps to improve the J_{sc}. Because of the synergistic effects of long bulky chains and F substituents, the related polymer-based BHJ solar cell exhibits the highest efficiency of up to 5.62%.

7.1.2. Engineer Interface

In chapter 4, uniform P3MT films were successfully fabricated on ITO surfaces by surface-initiated Kumada catalyst-transfer polycondensation (SI-KCTP) using surface bound (aryl)Ni(II)-Br Initiators. The P3MT interfacial layer is covalently bound, preventing delamination during processing of additional layers, which successfully served as the HTL for solution-processed BHJ polymer solar cells with a typical configuration. PCE of 5% has been achieved on doped thin P3MT interfacial layers in our investigation. Moreover, due to the good stability of P3MT/ITO substrates, devices

based on reused P3MT/ITO substrates extracted from old devices exhibit satisfactory efficiency as high as the original devices. All these doped P3MT-based devices exhibited satisfactory performance, indicating that P3MT interfacial layer is a promising alternative to PEDOT:PSS as the hole transport layer and thereby improve the stability of OPVs.

7.1.3. Design of Device Structure Is Crucial

Fully solution-processed polymer BHJ solar cells with anodes made from silver nanowires (Ag NWs) were successfully fabricated with a configuration of Ag NWs/PEDOT:PSS/ $PC_{61}BM$/Ca/Al in Chapter 5 Efficiencies of 2.8 % and 2.5 % were obtained for devices with Ag NW network on glass and on PET, respectively. .More importantly, highly flexible BHJ solar cells have been firstly fabricated on Ag NWs/PET anode with recoverable efficiency of 2.5% under large deformation up to 120°. These results indicate that, with improved engineering of the nanowires/polymer interface, Ag NW electrodes can serve as a low cost, flexible alternative to ITO, and thereby improve the economic viability and mechanical stability of OPVs. One can further improve efficiency of a solar cell by stacking multiple sub-cells in either series or parallel connection such that each sub-cell incorporating a polymer absorbing specific range of the solar spectrum. However, this approach is technically challenging, leading to an increased cost of fabrication. Therefore, we demonstrated a conceptually new approach, parallel bulk heterojunction (PBHJ) in Chapter 6. This PBHJ solar cell maintains the simple device configuration and low cost processing of single junction BHJ cells while inherits the major benefit of incorporating multiple polymers in tandem cells. In this PBHJ, free charge carriers travel through their corresponding donor polymer linked channels and fullerene enriched domain to the electrodes, equivalent to a parallel

connection. The J_{sc} of the PBHJ solar cell is nearly identical to the sum of individual J_{sc} of each single sub-cell, while the V_{oc} is in between of those from sub-cells. Preliminary optimization of PBHJ devices leads up to 40% improvement in J_{sc} and 30% in overall efficiency when compared with these of single BHJ devices.

7.2. Looking Forward

In the rest of this Chapter, I will try to expand the horizon beyond existing polymer and device architecture design and discuss some future development directions for the whole field of polymer solar cell.

7.3.1. Is a Higher PCE Possible?

So far the J_{sc} can reach as high as 17.3 mA/cm^2,[110] with absorption up to 900 nm (~ 1.3 eV); the highest V_{oc} obtained has been over 1 V; [146-148] and the highest obtained FF has breached 70%.[28,149] If we could achieve all these impressive values with one system, this champion BHJ solar cell would offer an unprecedented value of 12%! Unfortunately, all these high values are obtained from different polymer based BHJ systems, partly due to the inter-relation between some of the properties such as the balance between J_{sc} and V_{oc} as discussed in chapter 2. A more rigorous model calculation on the ultimate performance of polymer:fullerene BHJ cells predicts a maximum power efficiency of 11.7% for single cells and 14.1% for tandem structures.[80] However, if polymer solar cells (and organic solar cells in general) intend to compete with other thin film PV technologies (such as CIGS or CdTe) as a viable economic solution for renewable energy future, higher efficiencies (15 – 20%) will be strongly desirable if not required. Is a higher PCE for polymer solar cells possible? To answer this challenge, one has to analyze

the J_{sc}, V_{oc} and *FF* individually, since these three parameters finally determine the efficiency.

Short circuit current (J_{sc}). It is generally agreed that a smaller band gap favors a higher short circuit current. However, this trend reaches its maximum around 1.3 eV. Polymers with even smaller band gap than 1.3 eV fail to offer more current as expected from their absorption extending into near IR. It is because the usually small full width at half maximum (FWHM) of these conjugated polymers, normally on the order of 200 nm. Thus continuously shifting the absorption of the polymer towards IR end of the solar spectrum would inevitably diminish its ability to absorb the light in the visible region. There are several possible solutions have emerged to increase the absorption of conjugated polymers: 1) using random copolymerization to bring more than two monomers into the conjugated backbone. 2) stacking multiple sub-cells in tandem cells that each sub-cell incorporating a polymer absorbing specific range of the solar spectrum, 3) multi-blend system that mix several polymers absorbing specific ranges of the solar spectrum with fullerene and 4) applying light trapping for better light harvesting[73]. Alternatively, one can employ electron accepting materials that absorb complementary part of the solar spectrum in regard to the absorption of the electron donating polymers, thereby broadening the light harvesting of the active layer. The most successful example is the $PC_{71}BM$, whose less symmetry (compared with $PC_{61}BM$) renders a much enhanced absorption from 300 to 600 nm.[150] This strong absorption in the UV-Vis region by the $PC_{71}BM$ effectively complements the absorption usually ranging from 600 nm to 800 nm offered by these narrow band gap polymers, thereby leading to an appreciable increase (20% or more) in the J_{sc} of related solar cells when compared with that of $PC_{61}BM$ based

ones.   In addition to the low absorption polymer solar cells, the external quantum efficiency (EQE) remains relatively low (50% – 80%), even in these highly efficient polymers/fullerene BHJ solar cells. This is mainly due to the low mobility of charge carriers in these polymer:fullerene blends and the intrinsically disordered morphology of the BHJ cells, leading to poor charge transport.   Thus further improving the carrier mobilities (both holes and electronics), controlling the morphology, and finding methods to slow down or diminish charge recombination, should be among the research priorities.

Open circuit voltage (V_{oc}).   After years of investigation, it is generally accepted that the V_{oc} is proportional to the difference between the HOMO of the donor and the LUMO of the acceptor, though recent advances in understanding the origin of the V_{oc} have provided further insights.[98,99,151,152]   Therefore, the first priority is to further understand the origin of Voc.   With a recently developed new π electron acceptor (D99'BF)[153] Heeger and Wudl showed that a V_{oc} of 1.2 V could be obtained from the P3HT/D99'BF BHJ solar cell,[154] as opposed to the usually obtained 0.6 V in the case of P3HT/PC$_{61}$BM solar cells.   More importantly, these authors demonstrated that electron transfer could still occur even with only 0.12 eV in the LUMOs offset.   Apparently, the exciton binding energy could be as small as 0.1 eV (at least in the case of P3HT).   However, even in this successful demonstration, a loss of over 0.5 eV was still observed since the difference between the LUMO of D99'BF and the HOMO of P3HT was 1.78 eV.   Nevertheless, there is still a lot to be done to determine a clearer structure-property relationship regarding the V_{oc}, so the chemists will know how to design better materials (both electron donating and electron accepting materials). Alternatively, before we find new acceptors that can replace the fullerene on all fronts, we can still modify the structure of this

fascinating group of molecules to raise up their LUMO energy levels, in order to gain a higher V_{oc}. There have been successful examples such as trimetallic nitride endohedral fullerenes (TNEFs, in particular $Lu_3N@C80$),[155] indene-C_{60} bisadduct (ICBA),[13] among others.[156] The V_{oc} of related P3HT:modified fullerene BHJ cells can be increased as much as 0.26 V when compared with P3HT/$PC_{61}BM$ cells,[13] because of the raised LUMO energy level of the modified fullerene.

Fill factor (*FF*). Unlike silicon solar cell or even dye sensitized solar cells, both of which give high fill factors (75 – 80% or higher), the polymer solar cells usually only offer a fill factor around 60%. It is attributed to the low charge carrier mobilities (esp. holes) and the disordered nature of the BHJ film that leads to poor charge transport. In order to get a high *FF*, research efforts are needed to reach a balanced and rapid charge transport (holes vs. electrons), to optimize and control the film morphology into more ordered structure, and to improve all electric contacts. Another possible approach is engineering anode/cathode interfacial layers as charge selective contacts between the BHJ active layer and the electrodes. These interfacial layers can work as hole selective layer at anode or as electron selective layer at cathode which facilitate charge transport and charge collection near electrode, leading to improved *FF*.

7.3.2. How to Further Reduce the Cost?

Though the rational design of the active layer (e.g., polymer and fullerene or other acceptors) and device architecture (e.g. tandem cells) can further improve the efficiency of polymer BHJ cell as discussed in previous Chapters, one still needs to further reduce

the manufacturing cost before reaching the full potential of any given cell. Listed below are two approaches to low cost polymer solar cells:

Transparent electrode. ITO has been the standard transparent contact electrode for polymer solar cells. However, the physical nature (brittleness) and the high price associated with ITO prevent a large scale roll to roll production of polymer solar cells based on this particular material. Carbon nanotubes, graphenes[61-68] and metal nanowires[69,70] have been proposed and respectable results demonstrate that these electrodes meet the most important criteria of conductivity, transparency, flexibility, and solution-processability necessary to replace ITO in polymer solar cell. Therefore, these electrodes will likely enable high-throughput roll-to-roll manufacturing of low-cost polymer solar cells.

Stability. A long lifetime of polymer solar cells is crucial for low cost and commercialization. PEDOT:PSS is commonly used as the interfacial functional layer between the photoactive polymer and electrode contacts, however, its acidic nature etches the ITO and imposes potential lifetime instability. Therefore, metal oxides recently emerged as versatile interface modifiers, such as NiO,[57] MoO_3,[24,47,48] WO_3[49,50] as the hole transport layer to replace PEDOT:PSS. Devices based on these interfacial layers showed a much longer lifetime compared to the PEDOT:PSS based device. In addition, progresses have been made in the inverted cells to increase the air stability.[157] In an inverted architecture the anode is composed of a relatively stable hole collection layer covered by a high work function metal. The absence of PEDOT:PSS and low work function metals implies promising long term stability of the inverted structure. Significant

progress has been made to improve the stability of polymer solar cells ; for example, Konarka has shown a life time of three years for their polymer solar cells.[158]

Device Engineering. As discussed in Chapter 6, tandem structure can further improve efficiency of a solar cell, however, this approach lead to an increased cost of fabrication. Another approach is to blend multiple donor components of different absorption features (ideally complementary), into a single junction BHJ devices. Recently, this simple method has been successfully demonstrated by the addition of a small fraction (1 – 20%) of dye molecules or a small band gap polymer as sensitizers into the archetypical $P3HT/PC_{61}BM$ BHJ cells.[78,79] Moreover, our PBHJ enables the effective use of multiple donors with much improved light absorption and conversion. All of these multi-blend BHJ devices eliminate the needs of careful design and precise control of the interfacial layers in tandem cells, thereby significantly reducing the complexity of the device. However, detailed working mechanism and specific rationale in paring multiple polymers in BHJ devices remain to be further investigated to accelerate the efficiency improvement of polymer solar cells.

All these challenges and opportunities compose the major part of the long wish list for the commercialization of polymer solar cells. This is a formidable task; however, if we could achieve these goals, the payoff would be huge – roll-to-roll processed single junction polymer solar cells with 15% efficiency and 10 years lifetime would be within reach!

Appendix A:

Common Experimental Details

A1. Reagents and Instrumentation

All reagents and chemicals were purchased from commercial sources (Aldrich, Acros, Strem, Fluka) and used without further purification unless stated otherwise. Reagent grade solvents were dried when necessary and purified by distillation. Glass substrates coated with patterned indium-doped tin oxide (ITO) were purchased from *Thin Film Devices, Inc*. with a 150 nm thick sputtered ITO pattern and a resistivity of 15 $\Omega/\square$. Microwave assisted polymerizations were conducted in a CEM Discover Benchmate microwave reactor. Gel permeation chromatography (GPC) measurements were performed with a Polymer Laboratories PL-GPC 220 instrument using 1,2,4-trichlorobenzene solvent (stabilized with 125 ppm BHT) at 150 ^{o}C. The obtained molecular weight is relative to the polystyrene standard. UV-Visible absorption spectra were obtained by a Shimadzu UV-2401PC spectrophotometer. For the measurements of thin films, polymers were spun coated onto pre-cleaned glass slides from 10 mg/mL polymer solutions in chlorobenzene. The thicknesses of films were recorded by a profilometer (Alpha-Step 200, Tencor Instruments). Asylum Research MFP3D Atomic Force Microscope was used for taking AFM images. The microscope was operated in AC mode at ambient conditions (T = 21 °C, RH = 45 %), using silicon cantilevers (*BudgetSensors*, Tap300Al) with resonance frequencies of approximately 300 kHz. Powder X-ray diffraction spectra were obtained using a Bruker AXS SMART APEX II instrument. Samples were first peeled off from the solar cell devices and then mounted on the sample holder for XRD measurement.

A2. Electrochemistry

Cyclic voltammetry measurements were carried out using a Bioanalytical Systems (BAS) Epsilon potentiostat equipped with a standard three-electrode configuration. Typically, a three electrodes cell equipped with a glass carbon working electrode, a $Ag/AgNO_3$ (0.01M in anhydrous acetonitrile) reference electrode, and a Pt wire counter electrode was employed. The measurements were done in anhydrous acetonitrile with tetrabutyl ammonium hexafluorophosphate (0.1 M) as the supporting electrolyte under an argon atmosphere at a scan rate of 100 mV/s. Polymer films were drop cast onto the glassy carbon working electrode from a 2.5 mg/mL chloroform solution and dried under house nitrogen stream prior to measurements. The electrochemical onsets were determined at the position where the current starts to differ from the baseline. The potential of $Ag/AgNO_3$ reference electrode was internally calibrated by using the ferrocene/ferrocenium redox couple (Fc/Fc$^+$), which has a known reduction potential of –4.8e V[159,160] The highest occupied molecular orbital (HOMO) and lowest unoccupied molecular orbital (LUMO) energy levels of copolymers were calculated from the onset oxidation potentials (E_{onest}^{ox}) and onset reductive potentials (E_{onest}^{red}), respectively, according to equation (A.1) and (A.2). The electrochemically determined band gaps were deduced from the difference between onset potentials from oxidation and reduction of copolymers as depicted in equation (A.3).

$$\text{HOMO} = -\,(E_{onest}^{ox} + 4.8)\ (\text{eV}) \tag{A.1}$$

$$\text{LUMO} = -\,(E_{onest}^{ox} + 4.8)\ (\text{eV}) \tag{A.2}$$

$$E_{gap}^{EC} = E_{onest}^{ox} - E_{onest}^{red} \tag{A.3}$$

A3. Spectroscopy:

UV-Visible absorption spectra were obtained by a Shimadzu UV-2401PC spectrophotometer. Fluorescence spectra were recorded on a Shimadzu RF-5301PC spectrofluorophotometer. For the measurements of thin films, polymers were spun coated onto pre-cleaned glass slides from 10 mg/mL polymer solutions in chloroform. The thicknesses of films were recorded by a profilometer (Alpha-Step 200, Tencor Instruments).

Appendix B:

Supporting Information

B1. SCLC Mobility Measurement in Chapter 2

For mobility measurements, the hole-only devices in a configuration of ITO/PEDOT:PSS (40 nm)/polymer:$PC_{61}BM$/Pd (50 nm) were fabricated. The experimental dark current densities J of polymer:$PC_{61}BM$ blends were measured when applied with voltage from 0 to 6 V. The applied voltage V was corrected from the built-in voltage V_{bi} which was taken as a compensation voltage $V_{bi}=V_{oc} + 0.05$ V and the voltage drop V_{rs} across the ITO/PEDOT:PSS series resistance and contact resistance, which is found to be around 35 Ω from a reference device without the polymer layer. From the plots of $J^{0.5}$ vs. V (supporting information), hole mobilities of copolymers can be deduced from

$$J = \frac{9}{8}\varepsilon_r\varepsilon_0\mu_h\frac{V^2}{L^3} \qquad (B.1)$$

where ε_0 is the permittivity of free space, ε_r is the dielectric constant of the polymer which is assumed to be around 3 for the conjugated polymers, μ_h is the hole mobility, V is the voltage drop across the device, and L is the film thickness of active layer.

Table B.1. Mobility of polymers under SCLC condition

Polymer Only	Polymer Only		Polymer:PC$_{61}$BM (1:1)	
	Thickness (nm)	Mobility (cm^2/V·s)	Thickness (nm)	Mobility (cm^2/V·s)
C10,6-C8	40	3.27E-06 ± 6.87E-07	80	2.49E-05 ± 2.61E-06
C10,6-C6,2	40	9.41E-06 ± 2.64E-06	75	3.32E-05 ± 4.81E-06
C8-C8	35	5.49E-07 ± 1.93E-08	70	1.58E-05 ± 2.47E-06
C8-C12	35	1.25E-06 ± 1.63E-07	75	2.29E-05 ± 4.28E-06
C8-C6,2	40	1.61E-06 ± 2.27E-07	70	1.61E-05 ± 9.24E-07
C6,2-C6,2	40	8.05E-06 ± 1.16E-06	70	2.06E-05± 3.80E-06

B2. Computational Simulation in Chapter 2.

The optimized geometry, HOMO and LUMO energy levels and their electron density distributions were calculated at the B3LYP/6-311+G* level of theory using density functional theory and Gaussian 03 package (Fig. B.1).
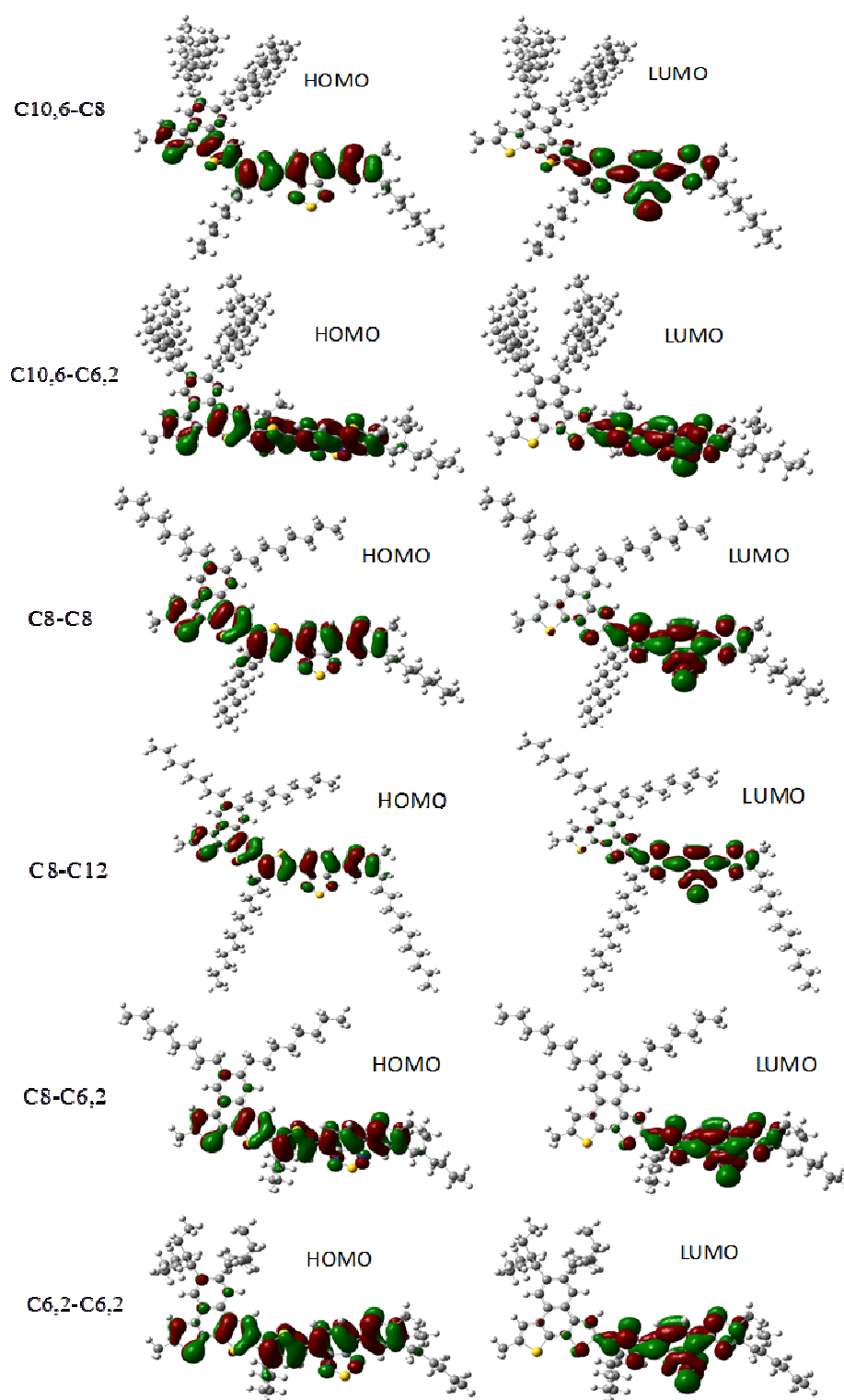
Figure B.1. Electron density distributions of all polymers at HOMO and LUMO.

B3. Multi-peak Gaussian Fitting in Chapter 3

Fig. B.2 shows the Multi-peak gaussian fitting to (a-d) out of plane and (e-h) in plane $PC_{61}BM$ and polymer 010 peaks. A cubic background is simultaneously fit along with the q location, peak width, and height of each peak. For the in plane data, an additional peak near $q = 1.8$ Å^{-1} is used. Panels (a,e) correspond to polymer/$PC_{61}BM$ blend C6,2-C6,2, while (b,f) correspond to C8,4-C6,2, (c,g) C6,2-C6,2F, and (d,h) C8,4-C6,2F.
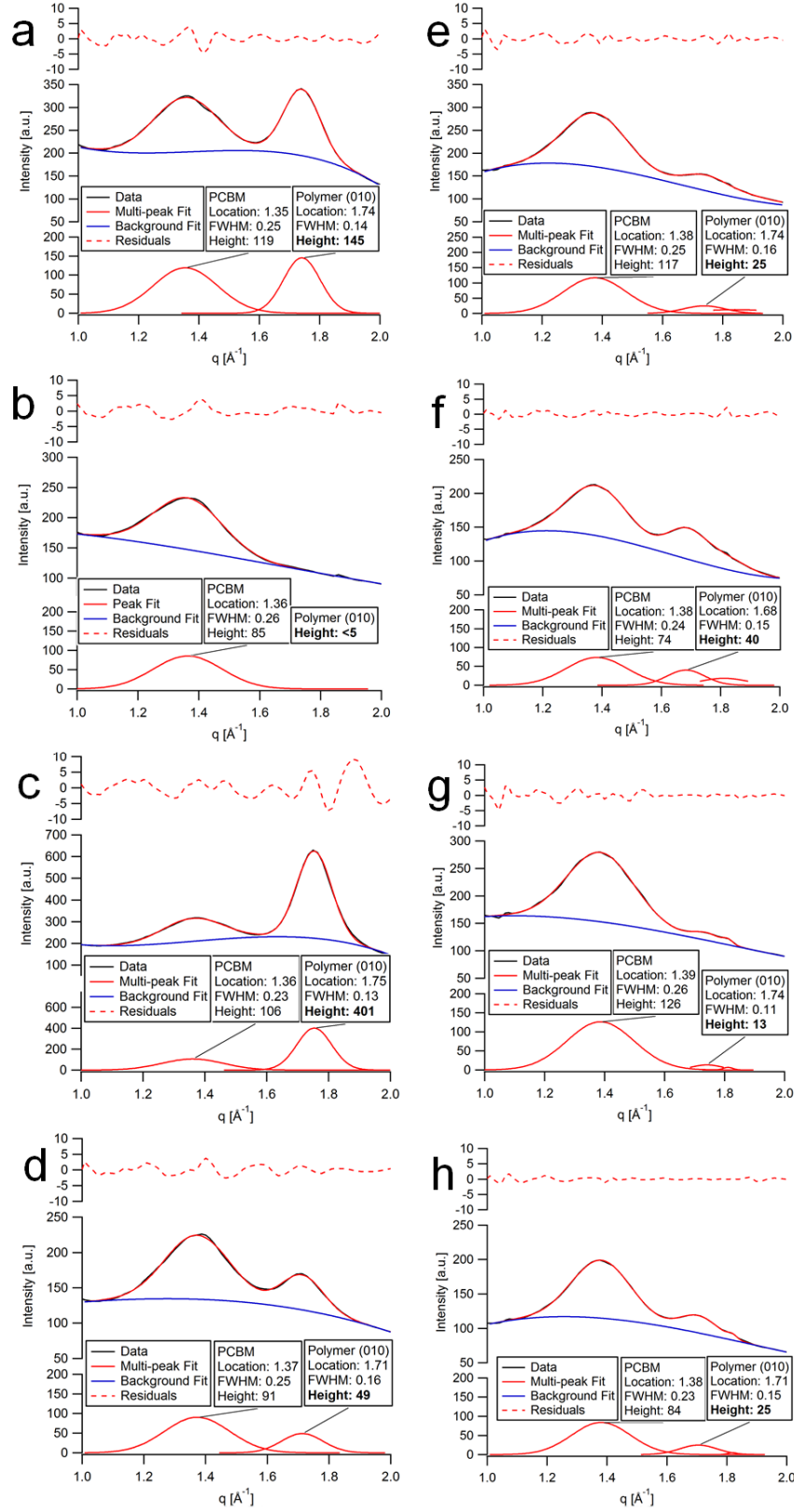
Figure B.2. Multi-peak gaussian fitting to (a-d) out of plane and (e-h) in plane PC$_{61}$BM and polymer 010 peaks.

B4. Ultraviolet Photoelectron Spectroscopy (UPS) in Chapter 4

In UPS the source of radiation is a He-discharge lamp emitting He I radiation of energy 21.2 eV . Such radiation is only capable of ionising electrons from the outermost levels of atoms - the valence levels. The UPS was performed in Chapter 5 to measure the work function (φ_m) of the Ag NW electrodes, the PEDOT:PSS and the ITO. UPS spectra of each substrate are shown below:

Figure B.3. UPS spectrum of ITO substrate (arrows indicating E_{min} on left and E_{max} on right).

FullUPS ITO 1:30(10075_UPS_AgNanowire_polymers)
UPS   Spectrum   Lens Mode:UPS   Resolution:Pass energy 5
Acqn. Time(s): 84   Sweeps: 1   Anode:He I(0 W)   Step(meV): 25.0
Dwell Time(ms): 100   Charge Neutraliser :Off   Acquired On :10/10/29 11:45:01

Kinetic Energy(eV)

LoUPS ITO 1:31(10075_UPS_AgNanowire_polymers)
UPS   Spectrum   Lens Mode:UPS   Resolution:Pass energy 5
Acqn. Time(s): 30   Sweeps: 1   Anode:He I(0 W)   Step(meV): 10.0
Dwell Time(ms): 100   Charge Neutraliser :Off   Acquired On :10/10/29 11:45:01

Kinetic Energy(eV)

HiUPS ITO 1:32(10075_UPS_AgNanowire_polymers)
UPS   Spectrum   Lens Mode:UPS   Resolution:Pass energy 5
Acqn. Time(s): 320   Sweeps: 1   Anode:He I(0 W)   Step(meV): 10.0
Dwell Time(ms): 400   Charge Neutraliser :Off   Acquired On :10/10/29 11:45:01

Kinetic Energy(eV)

Figure B.4. UPS spectrum of PEDOT:PSS coating ITO substrate (arrows indicating E_{min} on left and E_{max} on right).

Figure B.5. UPS spectrum of Ag NW sheet (arrows indicating E_{min} on left and E_{max} on right).

Figure B.6. UPS spectrum of PEDOT:PSS coating Ag NW/glass substrate (arrows indicating E_{min} on left and E_{max} on right).
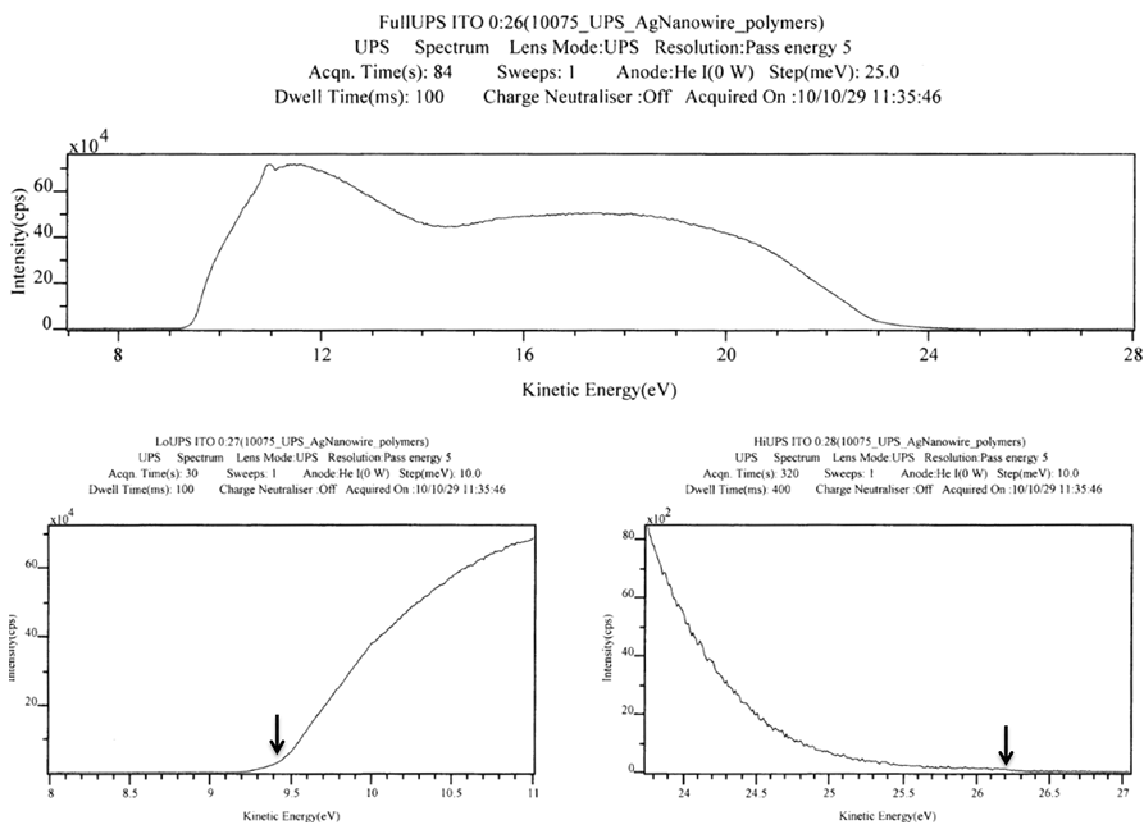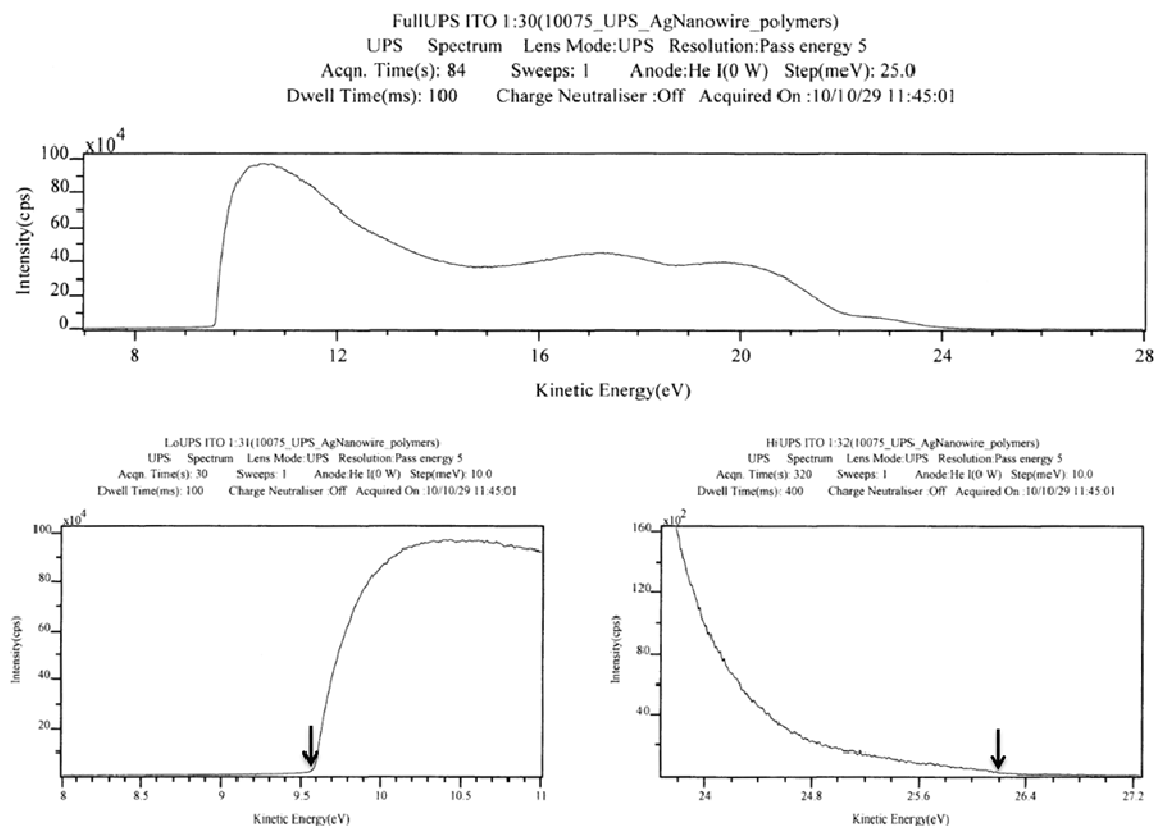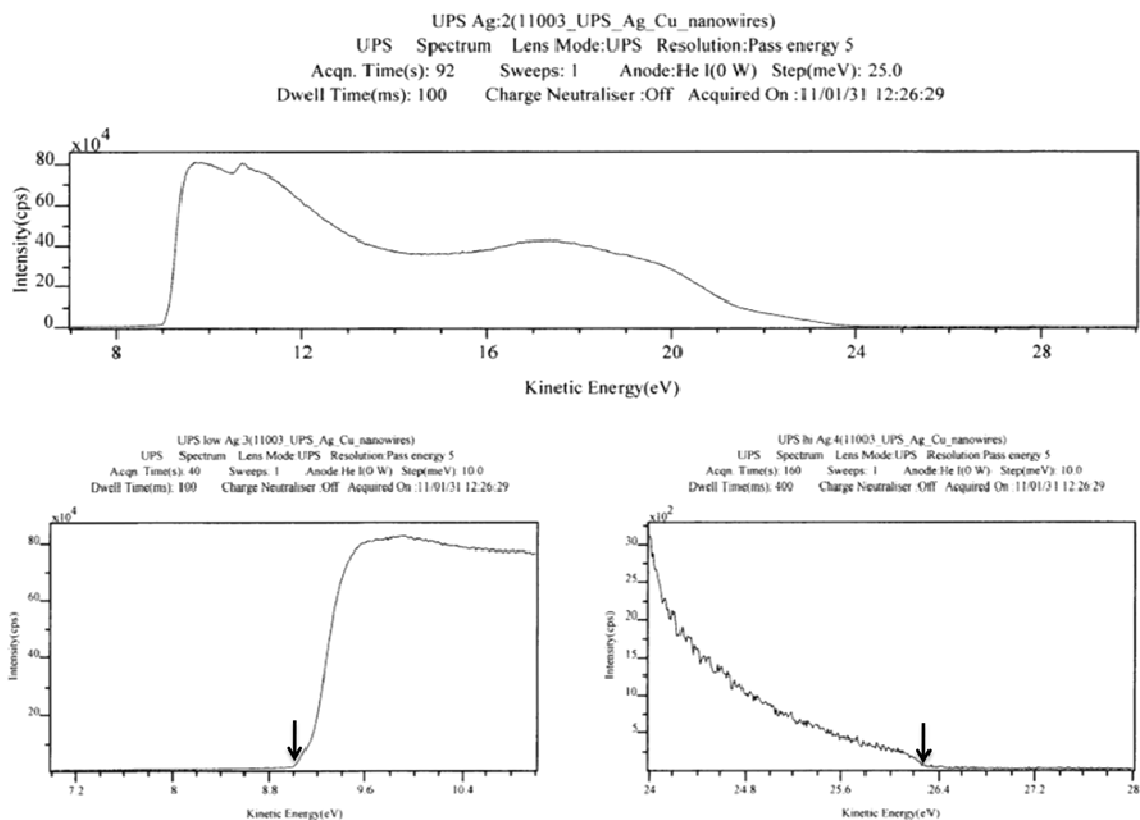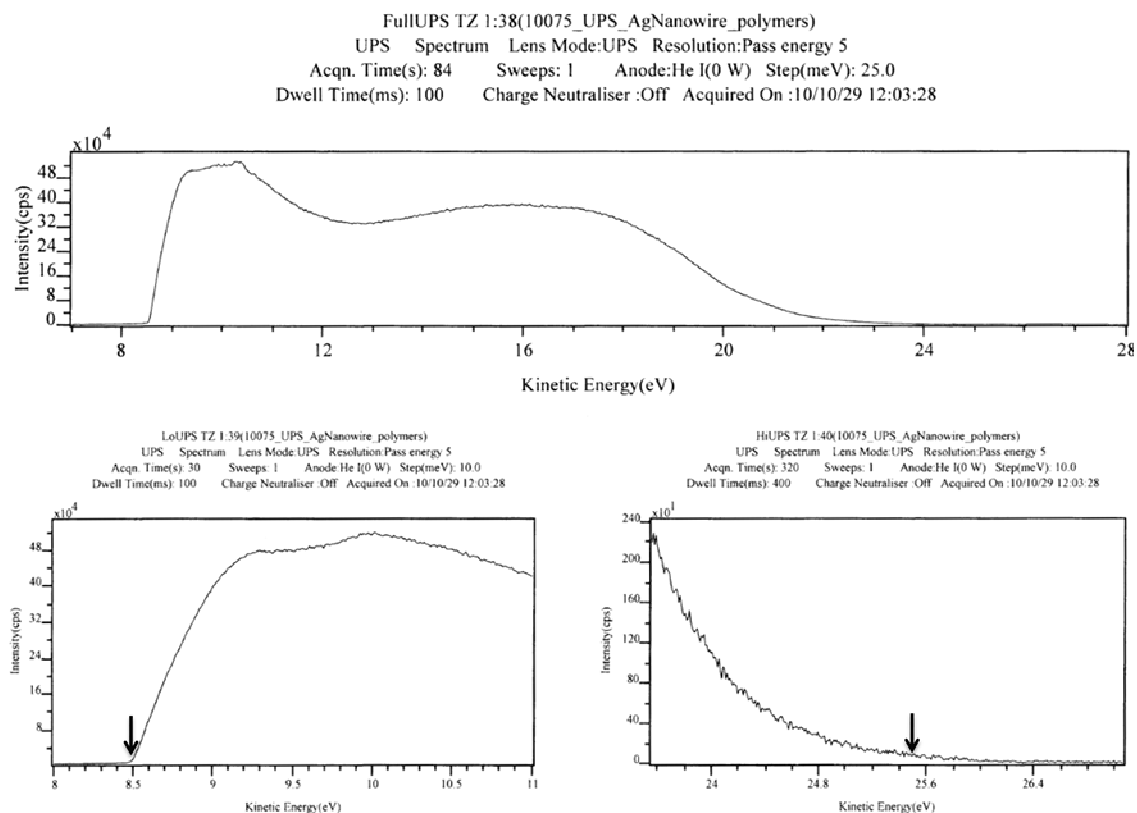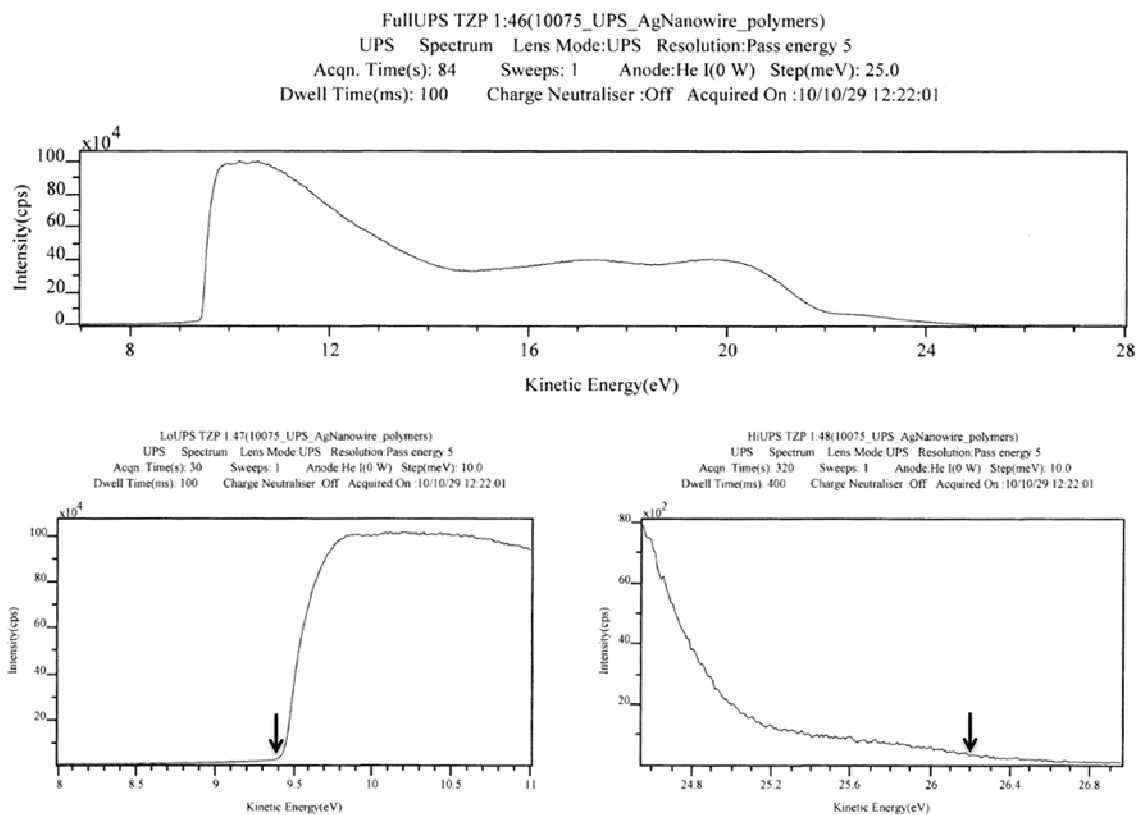
Figure B.7. UPS spectrum of PEDOT:PSS coating Ag NW/PET substrate (arrows indicating E_{min} on left and E_{max} on right).

REFERENCES

(1)   Zhao, J. H.; Wang, A. H.; Green, M. A.; Ferrazza, F. *Applied Physics Letters* 1998, *73*, 1991.

(2)   Green, M. A.; Emery, K.; Hishikawa, Y.; Warta, W. *Progress in Photovoltaics* 2009, *17*, 85.

(3)   Green, M. A.; Emery, K.; Hishikawa, Y.; Warta, W. *Progress in Photovoltaics: Research and Applications* 2011, *19*, 84.

(4)   Gunes, S.; Neugebauer, H.; Sariciftci, N. S. *Chemical Reviews* 2007, *107*, 1324.

(5)   Kallmann, H.; Pope, M. *Journal of Chemical Physics* 1959, *30*, 585.

(6)   Tang, C. W. *Applied Physics Letters* 1986, *48*, 183.

(7)   Sariciftci, N. S.; Smilowitz, L.; Heeger, A. J.; Wudl, F. *Science* 1992, *258*, 1474.

(8)   Yu, G.; Gao, J.; Hummelen, J. C.; Wudl, F.; Heeger, A. J. *Science* 1995, *270*, 1789.

(9)   Zhou, H.; Yang, L.; You, W. *Macromolecules* 2012, *45*, 607.

(10)   Kirchmeyer, S.; Reuter, K. *Journal of Materials Chemistry* 2005, *15*, 2077.

(11)   Cheng, Y.-J.; Yang, S.-H.; Hsu, C.-S. *Chemical Reviews* 2009, *109*, 5868.

(12)   Chen, H.-Y.; Hou, J.; Zhang, S.; Liang, Y.; Yang, G.; Yang, Y.; Yu, L.; Wu, Y.; Li, G. *Nat Photon* 2009, *3*, 649.

(13)   Facchetti, A. *Chemistry of Materials* 2010, *23*, 733.

(14)   Shaheen, S. E.; Brabec, C. J.; Sariciftci, N. S.; Padinger, F.; Fromherz, T.; Hummelen, J. C. *Applied Physics Letters* 2001, *78*, 841.

(15)   Brabec, C. J.; Shaheen, S. E.; Winder, C.; Sariciftci, N. S.; Denk, P. *Applied Physics Letters* 2002, *80*, 1288.

(16)   Ma, W. L.; Yang, C. Y.; Gong, X.; Lee, K.; Heeger, A. J. *Advanced Functional Materials* 2005, *15*, 1617.

(17)   Li, G.; Shrotriya, V.; Huang, J. S.; Yao, Y.; Moriarty, T.; Emery, K.; Yang, Y. *Nature Materials* 2005, *4*, 864.

(18)   Dennler, G.; Scharber, M. C.; Brabec, C. J. *Advanced Materials* 2009, *21*, 1323.

(19)   Kim, Y.; Cook, S.; Tuladhar, S. M.; Choulis, S. A.; Nelson, J.; Durrant, J. R.; Bradley, D. D. C.; Giles, M.; McCulloch, I.; Ha, C.-S.; Ree, M. *Nature Materials* 2006, *5*, 197.

(20)   He, Z.; Zhong, C.; Huang, X.; Wong, W.-Y.; Wu, H.; Chen, L.; Su, S.; Cao, Y. *Advanced Materials* 2011, *23*, 4636.

(21)   Liang, Y.; Xu, Z.; Xia, J.; Tsai, S.-T.; Wu, Y.; Li, G.; Ray, C.; Yu, L. *Advanced Materials* 2010, *22*, E135.

(22)   Huo, L.; Zhang, S.; Guo, X.; Xu, F.; Li, Y.; Hou, J. *Angewandte Chemie International Edition* 2011, *50*, 9697.

(23)   Park, S. H.; Roy, A.; Beaupre, S.; Cho, S.; Coates, N.; Moon, J. S.; Moses, D.; Leclerc, M.; Lee, K.; Heeger, A. J. *Nature Photonics* 2009, *3*, 297.

(24)   Sun, Y.; Takacs, C. J.; Cowan, S. R.; Seo, J. H.; Gong, X.; Roy, A.; Heeger, A. J. *Advanced Materials* 2011, *23*, 2226.

(25)   Amb, C. M.; Chen, S.; Graham, K. R.; Subbiah, J.; Small, C. E.; So, F.; Reynolds, J. R. *Journal of the American Chemical Society* 2011, *133*, 10062.

(26)   Chu, T.-Y.; Lu, J.; Beaupré, S.; Zhang, Y.; Pouliot, J.-R. m.; Wakim, S.; Zhou, J.; Leclerc, M.; Li, Z.; Ding, J.; Tao, Y. *Journal of the American Chemical Society* 2011, *133*, 4250.

(27)   Sun, Y.; Seo, J. H.; Takacs, C. J.; Seifter, J.; Heeger, A. J. *Advanced Materials* 2011, *23*, 1679.

(28)   Price, S. C.; Stuart, A. C.; Yang, L.; Zhou, H.; You, W. *Journal of the American Chemical Society* 2011, *133*, 4625.

(29)   Service, R. F. *Science* 2011, *332*, 293.

(30)   Zhou, H.; Yang, L.; Stuart, A. C.; Price, S. C.; Liu, S.; You, W. *Angewandte Chemie International Edition* 2011, *50*, 2995.

(31)   Cho, S.; Seo, J. H.; Kim, S. H.; Song, S.; Jin, Y.; Lee, K.; Suh, H.; Heeger, A. J. *Applied Physics Letters* 2008, *93*, 263301.

(32)   Jayakannan, M.; Van Hal, P. A.; Janssen, R. A. J. *Journal of Polymer Science Part a-Polymer Chemistry* 2002, *40*, 251.

(33)   Karikomi, M.; Kitamura, C.; Tanaka, S.; Yamashita, Y. *Journal of the American Chemical Society* 2002, *117*, 6791.

(34)   Wang, E.; Wang, M.; Wang, L.; Duan, C.; Zhang, J.; Cai, W.; He, C.; Wu, H.; Cao, Y. *Macromolecules* 2009, *42*, 4410.

(35)   Zhou, H.; Yang, L.; Xiao, S.; Liu, S.; You, W. *Macromolecules* 2010, *43*, 811.

(36)   Gadisa, A.; Oosterbaan, W. D.; Vandewal, K.; Bolsée, J.-C.; Bertho, S.; D'Haen, J.; Lutsen, L.; Vanderzande, D.; Manca, J. V. *Advanced Functional Materials* 2009, *19*, 3300.

(37)   Egbe, D. A. M.; Tu☐rk, S.; Rathgeber, S.; Ku☐hnlenz, F.; Jadhav, R.; Wild, A.; Birckner, E.; Adam, G.; Pivrikas, A.; Cimrova, V.; Kno☐r, G. n.; Sariciftci, N. S.; Hoppe, H. *Macromolecules* 2010, *43*, 1261.

(38)   Brédas, J. L.; Heeger, A. J. *Chemical Physics Letters* 1994, *217*, 507.

(39)   Helbig, M.; Hörhold, H.-H. *Die Makromolekulare Chemie* 1993, *194*, 1607.

(40)   Wong, S.; Ma, H.; Jen, A. K. Y.; Barto, R.; Frank, C. W. *Macromolecules* 2003, *36*, 8001.

(41)   Reichenbacher, K.; Suss, H. I.; Hulliger, J. *Chemical Society Reviews* 2005, *34*, 22.

(42)   Pagliaro, M.; Ciriminna, R. *Journal of Materials Chemistry* 2005, *15*, 4981.

(43)   Wang, Y.; Parkin, S. R.; Gierschner, J.; Watson, M. D. *Organic Letters* 2008, *10*, 3307.

(44)   Wong, K. W.; Yip, H. L.; Luo, Y.; Wong, K. Y.; Lau, W. M.; Low, K. H.; Chow, H. F.; Gao, Z. Q.; Yeung, W. L.; Chang, C. C. *Applied Physics Letters* 2002, *80*, 2788.

(45)   Yan, H.; Lee, P.; Armstrong, N. R.; Graham, A.; Evmenenko, G. A.; Dutta, P.; Marks, T. J. *Journal of the American Chemical Society* 2005, *127*, 3172.

(46)   Ma, H.; Yip, H.-L.; Huang, F.; Jen, A. K. Y. *Advanced Functional Materials* 2010, *20*, 1371.

(47)   Subbiah, J.; Kim, D. Y.; Hartel, M.; So, F. *Applied Physics Letters* 2010, *96*, 063303.

(48)   Kro☐ger, M.; Hamwi, S.; Meyer, J.; Riedl, T.; Kowalsky, W.; Kahn, A. *Applied Physics Letters* 2009, *95*, 123301.

(49)   Tao, C.; Ruan, S. P.; Xie, G. H.; Kong, X. Z.; Shen, L.; Meng, F. X.; Liu, C. X.; Zhang, X. D.; Dong, W.; Chen, W. Y. *Applied Physics Letters* 2009, *94*.

(50)   Meyer, J.; Kroger, M.; Hamwi, S.; Gnam, F.; Riedl, T.; Kowalsky, W.; Kahn, A. *Applied Physics Letters* 2010, *96*, 193302.

(51)   Hayakawa, A.; Yoshikawa, O.; Fujieda, T.; Uehara, K.; Yoshikawaa, S. *Applied Physics Letters* 2007, *90*.

(52)   Kim, J. Y.; Kim, S. H.; Lee, H. H.; Lee, K.; Ma, W. L.; Gong, X.; Heeger, A. J. *Advanced Materials* 2006, *18*, 572.

(53)   Yip, H.-L.; Hau, S. K.; Baek, N. S.; Ma, H.; Jen, A. K. Y. *Advanced Materials* 2008, *20*, 2376.

(54)   Bulliard, X.; Ihn, S.-G.; Yun, S.; Kim, Y.; Choi, D.; Choi, J.-Y.; Kim, M.; Sim, M.; Park, J.-H.; Choi, W.; Cho, K. *Advanced Functional Materials* 2010, *20*, 4381.

(55)   Jung, J. W.; Lee, J. U.; Jo, W. H. *The Journal of Physical Chemistry C* 2009, *114*, 633.

(56)   Shrotriya, V.; Li, G.; Yao, Y.; Chu, C.-W.; Yang, Y. *Applied Physics Letters* 2006, *88*, 073508.

(57)   Irwin, M. D.; Buchholz, D. B.; Hains, A. W.; Chang, R. P. H.; Marks, T. J. *Proceedings of the National Academy of Sciences* 2008, *105*, 2783.

(58)   Steirer, K. X.; Chesin, J. P.; Widjonarko, N. E.; Berry, J. J.; Miedaner, A.; Ginley, D. S.; Olson, D. C. *Organic Electronics* 2010, *11*, 1414.

(59)   Steirer, K. X.; Ndione, P. F.; Widjonarko, N. E.; Lloyd, M. T.; Meyer, J.; Ratcliff, E. L.; Kahn, A.; Armstrong, N. R.; Curtis, C. J.; Ginley, D. S.; Berry, J. J.; Olson, D. C. *Advanced Energy Materials* 2011, *1*, 813.

(60)   Leterrier, Y.; Médico, L.; Demarco, F.; Månson, J. A. E.; Betz, U.; Escolà, M. F.; Kharrazi Olsson, M.; Atamny, F. *Thin Solid Films* 2004, *460*, 156.

(61)   Wu, Z.; Chen, Z.; Du, X.; Logan, J. M.; Sippel, J.; Nikolou, M.; Kamaras, K.; Reynolds, J. R.; Tanner, D. B.; Hebard, A. F.; Rinzler, A. G. *Science* 2004, *305*, 1273.

(62)   Zhang, M.; Fang, S.; Zakhidov, A. A.; Lee, S. B.; Aliev, A. E.; Williams, C. D.; Atkinson, K. R.; Baughman, R. H. *Science* 2005, *309*, 1215.

(63)   Li, J.; Hu, L.; Wang, L.; Zhou, Y.; Grüner, G.; Marks, T. J. *Nano Letters* 2006, *6*, 2472.

(64)   Miller, A. J.; Hatton, R. A.; Silva, S. R. P. *Applied Physics Letters* 2006, *89*, 133117.

(65)   Rowell, M. W.; Topinka, M. A.; McGehee, M. D.; Prall, H.-J.; Dennler, G.; Sariciftci, N. S.; Hu, L.; Gruner, G. *Applied Physics Letters* 2006, *88*, 233506.

(66)   Eda, G.; Fanchini, G.; Chhowalla, M. *Nat Nano* 2008, *3*, 270.

(67)   Kim, K. S.; Zhao, Y.; Jang, H.; Lee, S. Y.; Kim, J. M.; Kim, K. S.; Ahn, J.-H.; Kim, P.; Choi, J.-Y.; Hong, B. H. *Nature* 2009, *457*, 706.

(68)   Gomez De Arco, L.; Zhang, Y.; Schlenker, C. W.; Ryu, K.; Thompson, M. E.; Zhou, C. *ACS Nano* 2010, *4*, 2865.

(69)   Kang, M.-G.; Guo, L. J.; 6 ed.; AVS: 2007; Vol. 25, p 2637.

(70)   Tvingstedt, K.; Inganäs, O. *Advanced Materials* 2007, *19*, 2893.

(71)   Wu, H.; Hu, L.; Rowell, M. W.; Kong, D.; Cha, J. J.; McDonough, J. R.; Zhu, J.; Yang, Y.; McGehee, M. D.; Cui, Y. *Nano Letters* 2010, *10*, 4242.

(72)   Lee, J.-Y.; Connor, S. T.; Cui, Y.; Peumans, P. *Nano Letters* 2008, *8*, 689.

(73)   Ko, D.-H.; Tumbleston, J. R.; Zhang, L.; Williams, S.; DeSimone, J. M.; Lopez, R.; Samulski, E. T. *Nano Letters* 2009, *9*, 2742.

(74)   Hu, L.; Kim, H. S.; Lee, J.-Y.; Peumans, P.; Cui, Y. *ACS Nano* 2010, *4*, 2955.

(75)   Lee, J.-Y.; Connor, S. T.; Cui, Y.; Peumans, P. *Nano Letters* 2010, *10*, 1276.

(76)   Gaynor, W.; Lee, J.-Y.; Peumans, P. *ACS Nano* 2009, *4*, 30.

(77)   Beaujuge, P. M.; Amb, C. M.; Reynolds, J. R. *Accounts of Chemical Research* 2010, *43*, 1396.

(78)   Honda, S.; Ohkita, H.; Benten, H.; Ito, S. *Chemical Communications* 2010, *46*.

(79)   Koppe, M.; Egelhaaf, H.-J.; Dennler, G.; Scharber, M. C.; Brabec, C. J.; Schilinsky, P.; Hoth, C. N. *Advanced Functional Materials* 2010, *20*, 338.

(80)   Kotlarski, J. D.; Blom, P. W. M. *Applied Physics Letters* 2011, *98*, 053301.

(81)   Kim, J. Y.; Lee, K.; Coates, N. E.; Moses, D.; Nguyen, T.-Q.; Dante, M.; Heeger, A. J. *Science* 2007, *317*, 222.

(82)   Sista, S.; Park, M.-H.; Hong, Z.; Wu, Y.; Hou, J.; Kwan, W. L.; Li, G.; Yang, Y. *Advanced Materials* 2010, *22*, 380.

(83)   Chou, C.-H.; Kwan, W. L.; Hong, Z.; Chen, L.-M.; Yang, Y. *Advanced Materials* 2011, *23*, 1282.

(84)   Yakimov, A.; Forrest, S. *Appl. Phys. Lett.* 2002, *80*, 1667.

(85)   Hadipour, A.; de Boer, B.; Blom, P. W. *Journal of Applied Physics* 2007, *102*, 074506.

(86)   Yang, F.; Lunt, R. R.; Forrest, S. R. *Appl. Phys. Lett.* 2008, *92*, 053310.

(87)   Zhang, C.; Tong, S. W.; Jiang, C.; Kang, E. T.; Chan, D. S.; Zhu, C. *Applied Physics Letters* 2008, *92*, 083310.

(88)   Yuen, A. P.; Hor, A.-M.; Preston, J. S.; Klenkler, R.; Bamsey, N. M.; Loutfy, R. O. *Applied Physics Letters* 2011, *98*, 173301.

(89)   Hadipour, A.; de Boer, B.; Blom, P. W. M. *Advanced Functional Materials* 2008, *18*, 169.

(90)   Siddiki, M. K.; Li, J.; Galipeau, D.; Qiao, Q. *Energy & Environmental Science* 2010, *3*, 867.

(91)   Sista, S.; Hong, Z.; Chen, L.-M.; Yang, Y. *Energy & Environmental Science* 2011, *4*, 1606.

(92)   Moliton, A.; Nunzi, J.-M. *Polymer International* 2006, *55*, 583.

(93)   Scharber, M. C.; Mühlbacher, D.; Koppe, M.; Denk, P.; Waldauf, C.; Heeger, A. J.; Brabec, C. J. *Advanced Materials* 2006, *18*, 789.

(94)   Peet, J.; Kim, J. Y.; Coates, N. E.; Ma, W. L.; Moses, D.; Heeger, A. J.; Bazan, G. C. *Nat Mater* 2007, *6*, 497.

(95)   Thompson, B. C.; Fréchet, J. M. J. *Angewandte Chemie International Edition* 2008, *47*, 58.

(96)   Price, S. C.; Stuart, A. C.; You, W. *Macromolecules* 2010, *43*, 4609.

(97)   Zhou, H.; Yang, L.; Stoneking, S.; You, W. *ACS Applied Materials & Interfaces* 2010, *2*, 1377.

(98)   Perez, M. D.; Borek, C.; Forrest, S. R.; Thompson, M. E. *Journal of the American Chemical Society* 2009, *131*, 9281.

(99)   Vandewal, K.; Tvingstedt, K.; Gadisa, A.; Inganas, O.; Manca, J. V. *Nat Mater* 2009, *8*, 904.

(100)   Huo, L.; Chen, H.-Y.; Hou, J.; Chen, T. L.; Yang, Y. *Chemical Communications* 2009, 5570.

(101)   Fahrenbruch, A. L.; Aranovich, J. *Springer-Verlag: Berlin, Heidelberg, New York,* 1979, *31*.

(102)   Bube, H. R.; Fahrenbruch, A. L. *Academic, New York* 1981, 163.

(103)   Rand, B. P.; Burk, D. P.; Forrest, S. R. *Physical Review B* 2007, *75*, 115327.

(104)   Würfel, P. *Wiley-VCH* 2005.

(105)   Sze, S. M. *Wiley-Interscience: New York* 1981.

(106)   Liang, Y.; Feng, D.; Wu, Y.; Tsai, S.-T.; Li, G.; Ray, C.; Yu, L. *Journal of the American Chemical Society* 2009, *131*, 7792.

(107)   Ko, S.; Verploegen, E.; Hong, S.; Mondal, R.; Hoke, E. T.; Toney, M. F.; McGehee, M. D.; Bao, Z. *Journal of the American Chemical Society* 2011, *133*, 16722.

(108)   Hou, J.; Chen, H.-Y.; Zhang, S.; Chen, R. I.; Yang, Y.; Wu, Y.; Li, G. *Journal of the American Chemical Society* 2009, *131*, 15586.

(109)   Zou, Y.; Najari, A.; Berrouard, P.; Beaupré, S.; Réda Ai☐ch, B.; Tao, Y.; Leclerc, M. *Journal of the American Chemical Society* 2010, *132*, 5330.

(110)   Coffin, R. C.; Peet, J.; Rogers, J.; Bazan, G. C. *Nat Chem* 2009, *1*, 657.

(111)   Zhou, H.; Yang, L.; Price, S. C.; Knight, K. J.; You, W. *Angewandte Chemie International Edition* 2010, *49*, 7992.

(112)   Piliego, C.; Holcombe, T. W.; Douglas, J. D.; Woo, C. H.; Beaujuge, P. M.; Freì☐chet, J. M. J. *Journal of the American Chemical Society* 2010, *132*, 7595.

(113)   Szarko, J. M.; Guo, J.; Liang, Y.; Lee, B.; Rolczynski, B. S.; Strzalka, J.; Xu, T.; Loser, S.; Marks, T. J.; Yu, L.; Chen, L. X. *Advanced Materials* 2010, *22*, 5468.

(114)   Yang, L.; Zhou, H.; You, W. *The Journal of Physical Chemistry C* 2010, *114*, 16793.

(115)   Son, H. J.; Wang, W.; Xu, T.; Liang, Y.; Wu, Y.; Li, G.; Yu, L. *Journal of the American Chemical Society* 2011, *133*, 1885.

(116)   Okamoto, T.; Nakahara, K.; Saeki, A.; Seki, S.; Oh, J. H.; Akkerman, H. B.; Bao, Z.; Matsuo, Y. *Chemistry of Materials* 2011, *23*, 1646.

(117)   Beaujuge, P. M.; Pisula, W.; Tsao, H. N.; Ellinger, S.; Mu☐llen, K.; Reynolds, J. R. *Journal of the American Chemical Society* 2009, *131*, 7514.

(118)   Beiley, Z. M.; Hoke, E. T.; Noriega, R.; Dacuña, J.; Burkhard, G. F.; Bartelt, J. A.; Salleo, A.; Toney, M. F.; McGehee, M. D. *Advanced Energy Materials* 2011, *1*, 954.

(119)   Guo, J.; Liang, Y.; Szarko, J.; Lee, B.; Son, H. J.; Rolczynski, B. S.; Yu, L.; Chen, L. X. *The Journal of Physical Chemistry B* 2009, *114*, 742.

(120)   Yiu, A. T.-H.; Beaujuge, P. M.; Lee, O. P.; Woo, C. H.; Toney, M. F.; Frechet, J. M. J. *Journal of the American Chemical Society* 2011.

(121)   Burkhard, G. F.; Hoke, E. T.; McGehee, M. D. *Advanced Materials* 2010, *22*, 3293.

(122)   Tumbleston, J. R.; Liu, Y.; Samulski, E. T.; Lopez, R. *Advanced Energy Materials* 2012, *2*, 477.

(123)   Mihailetchi, V. D.; Koster, L. J. A.; Hummelen, J. C.; Blom, P. W. M. *Physical Review Letters* 2004, *93*, 216601.

(124)   Servaites, J. D.; Ratner, M. A.; Marks, T. J. *Energy & Environmental Science* 2011, *4*, 4410.

(125)   Cowan, S. R.; Roy, A.; Heeger, A. J. *Physical Review B* 2010, *82*, 245207.

(126)   Jamieson, F. C.; Agostinelli, T.; Azimi, H.; Nelson, J.; Durrant, J. R. *The Journal of Physical Chemistry Letters* 2010, *1*, 3306.

(127)   Shuttle, C. G.; Hamilton, R.; O'Regan, B. C.; Nelson, J.; Durrant, J. R. *Proceedings of the National Academy of Sciences* 2010, *107*, 16448.

(128)   Sokel, R.; Hughes, R. C. *Journal of Applied Physics* 1982, *53*, 7414.

(129)   Peer, K. *Modern fluoroorganic chemistry : synthesis, reactivity, applications*; WILEY-VCH Verlag GmbH & Co. KGaA, Weinheim, 2004.

(130) Carsten, B.; Szarko, J. M.; Son, H. J.; Wang, W.; Lu, L.; He, F.; Rolczynski, B. S.; Lou, S. J.; Chen, L. X.; Yu, L. *Journal of the American Chemical Society* 2011, *133*, 20468.

(131) Sontag, S. K.; Sheppard, G. R.; Usselman, N. M.; Marshall, N.; Locklin, J. *Langmuir* 2011, *27*, 12033.

(132) Marshall, N.; Sontag, S. K.; Locklin, J. *Chemical Communications* 2011, *47*, 5681.

(133) Doubina, N.; Jenkins, J. L.; Paniagua, S. A.; Mazzio, K. A.; MacDonald, G. A.; Jen, A. K. Y.; Armstrong, N. R.; Marder, S. R.; Luscombe, C. K. *Langmuir* 2011, *28*, 1900.

(134) Senkovskyy, V.; Khanduyeva, N.; Komber, H.; Oertel, U.; Stamm, M.; Kuckling, D.; Kiriy, A. *Journal of the American Chemical Society* 2007, *129*, 6626.

(135) Tenent, R. C.; Barnes, T. M.; Bergeson, J. D.; Ferguson, A. J.; To, B.; Gedvilas, L. M.; Heben, M. J.; Blackburn, J. L. *Advanced Materials* 2009, *21*, 3210.

(136) Barnes, T. M.; Bergeson, J. D.; Tenent, R. C.; Larsen, B. A.; Teeter, G.; Jones, K. M.; Blackburn, J. L.; van de Lagemaat, J. *Applied Physics Letters* 2010, *96*, 243309.

(137) Li, D.; Xia, Y. *Advanced Materials* 2004, *16*, 1151.

(138) Pike, G. E.; Seager, C. H. *Physical Review B* 1974, *10*, 1421.

(139) Brabec, C. J.; Cravino, A.; Meissner, D.; Sariciftci, N. S.; Fromherz, T.; Rispens, M. T.; Sanchez, L.; Hummelen, J. C. *Advanced Functional Materials* 2001, *11*, 374.

(140) Gadisa, A.; Svensson, M.; Andersson, M. R.; Inganas, O. *Applied Physics Letters* 2004, *84*, 1609.

(141) Mihailetchi, V. D.; Blom, P. W. M.; Hummelen, J. C.; Rispens, M. T. *Journal of Applied Physics* 2003, *94*, 6849.

(142) Shen, Y.; Hosseini, A. R.; Wong, M. H.; Malliaras, G. G. *ChemPhysChem* 2004, *5*, 16.

(143) Ishii, H.; Sugiyama, K.; Ito, E.; Seki, K. *Advanced Materials* 1999, *11*, 605.

(144)   Zhou, E.; Cong, J.; Wei, Q.; Tajima, K.; Yang, C.; Hashimoto, K. *Angewandte Chemie* 2011, *123*, 2851.

(145)   Mikroyannidis, J. A.; Tsagkournos, D. V.; Balraju, P.; Sharma, G. D. *Journal of Power Sources* 2011, *196*, 2364.

(146)   Gadisa, A.; Mammo, W.; Andersson, L. M.; Admassie, S.; Zhang, F.; Andersson, M. R.; Inganäs, O. *Advanced Functional Materials* 2007, *17*, 3836.

(147)   Zhang, F.; Jespersen, K. G.; Björström, C.; Svensson, M.; Andersson, M. R.; Sundström, V.; Magnusson, K.; Moons, E.; Yartsev, A.; Inganäs, O. *Advanced Functional Materials* 2006, *16*, 667.

(148)   Zheng, Q.; Jung, B. J.; Sun, J.; Katz, H. E. *Journal of the American Chemical Society* 2010, *132*, 5394.

(149)   Zoombelt, A. P.; Mathijssen, S. G. J.; Turbiez, M. G. R.; Wienk, M. M.; Janssen, R. A. J. *Journal of Materials Chemistry* 2010, *20*, 2240.

(150)   Wienk, M. M.; Kroon, J. M.; Verhees, W. J. H.; Knol, J.; Hummelen, J. C.; van Hal, P. A.; Janssen, R. A. J. *Angewandte Chemie International Edition* 2003, *42*, 3371.

(151)   Zhou, H.; Yang, L.; Liu, S.; You, W. *Macromolecules* 2010, *43*, 10390.

(152)   Schlenker, C. W.; Thompson, M. E. *Chemical Communications* 2011, *47*, 3702.

(153)   Brunetti, F. G.; Gong, X.; Tong, M.; Heeger, A. J.; Wudl, F. *Angewandte Chemie International Edition* 2010, *49*, 532.

(154)   Gong, X.; Tong, M.; Brunetti, F. G.; Seo, J.; Sun, Y.; Moses, D.; Wudl, F.; Heeger, A. J. *Advanced Materials* 2011, *23*, 2272.

(155)   Ross, R. B.; Cardona, C. M.; Guldi, D. M.; Sankaranarayanan, S. G.; Reese, M. O.; Kopidakis, N.; Peet, J.; Walker, B.; Bazan, G. C.; Van Keuren, E.; Holloway, B. C.; Drees, M. *Nature Materials* 2009, *8*, 208.

(156)   Varotto, A.; Treat, N. D.; Jo, J.; Shuttle, C. G.; Batara, N. A.; Brunetti, F. G.; Seo, J. H.; Chabinyc, M. L.; Hawker, C. J.; Heeger, A. J.; Wudl, F. *Angewandte Chemie International Edition* 2011, *50*, 5166.

(157)   Ameri, T.; Dennler, G.; Waldauf, C.; Azimi, H.; Seemann, A.; Forberich, K.; Hauch, J.; Scharber, M.; Hingerl, K.; Brabec, C. J. *Advanced Functional Materials* 2010, *20*, 1592.

(158)   Konarka Technologies, I. *http://www.konarka.com/* 2011.

(159)   Pommerehne, J.; Vestweber, H.; Guss, W.; Mahrt, R. F.; Bassler, H.; Porsch, M.; Daub, J. *Advanced Materials* 1995, *7*, 551.

(160)   Zhan, X. W.; Liu, Y. Q.; Wu, X.; Wang, S. A.; Zhu, D. B. *Macromolecules* 2002, *35*, 2529.